Ultrastructure and Mechanical changes in multi-scale of Sclera following Proteoglycan Depletion

Thesis submitted in accordance with the requirements of the University of Liverpool for the degree of Doctor of Philosophy by

Zhuola

October 2018

Acknowledgements

The completion of this PhD dissertation would not have been possible without the help and support of many people. I am forever grateful to Dr Riaz Akhtar, and I appreciate all his contributions of all the time and ideas to my PhD. As my primary supervisor, he guided me through the long journey of the PhD pursuit, while giving me the freedom to develop my research project. I am also thankful for the excellent example he has provided as a dedicated researcher. I would like to thank my second supervisor Professor Ahmed Elsheikh for his support, constructive feedback on my work. I also want to thank the School Director of Postgraduate Research professor Haujiang Ouyang who gave me great help during my maternity leave and the leave to China for my mother's surgery. Thankful for Professor Eithne Comerford who provided me with the enzyme and valuable advice. Dr Edwin Yates and Miss Shao-Hsuan Chang who offered my help with my biochemistry work, my study wouldn't be complete without your help. Also I would like to thank my examiners Dr Colin Grant and Dr Elizabeth Laird for all the helpful advices for my research.

I am grateful for the School of engineering for funded my research and provide me with such an enjoyable environment for studying.

Thank my colleagues at the University of Liverpool, past and present, for their support and advice. Very special thanks to Zhuo Chang, Liuying Li, Rui Chen, Ahmed Kazaili, Fatemeh Rostaminiya, Shao-Hsuan Chang, Dong Zhou and Phakakorn Panpho for their support and most importantly their friendship. Our many discussions, scientific and otherwise, really helped me throughout this PhD. Also, thank all the musician in the university symphony orchestra, I will always miss our Monday night rehearsal.

I am thankful for all the friends I made at Liverpool, especially Fang Wang, Zhaoliang Zheng, Coco Chen, Liang Zhang, Sissy Liu and Bo Zhou for our good laughs and all the fun weekends. Special thanks to my little friends Qianqian, Alice, Chenchen and Xinxin, your smiles always fill my heart and light up my day.

Words cannot express how grateful I am for my family. A special thanks to my mother-in-law, father-in-law for all of the sacrifices that you've made on my behalf. To my dear mother, thank you for being so strong for me, thank you for forgiving me as a terrible daughter who wasn't there for you when you needed the most. And my beloved husband, Liang Guo. Thank you for supporting me for everything, thank you for encouraging me throughout this experience. To my beloved daughter Sarangerel Guo, I would like to express my thanks for being such a good girl, your laugh and kisses always cheer me up and keep me going.

Ultrastructure and Mechanical changes in multi-scale of Sclera following Proteoglycan Depletion

Author: Zhuola

The sclera is the dense outer coating of the eye which provides the structural framework that defines the shape of the eye. It is mainly composed of collagen, elastin and interfibrillar proteoglycans. The mechanical properties the sclera have a major impact on healthy function of the eye and are governed by the properties and composition of the microstructural components. For example, biomechanical degradation associated with glaucomatous and myopia occurs alongside a reduction of proteoglycans. The contribution of proteoglycan to the mechanical behaviour of posterior sclera has been studied before. However the distribution of proteoglycan various greatly through all regions of the sclera and the mechanical role of proteoglycan in all scleral region has never been studied. Therefore, this work aims to investigate the contributions of proteoglycan to the structure and mechanical properties of all regions of the sclera, as well as their possible mechanical role in occurs pathology like myopia.

In this study, the role of proteoglycan degradation on the tissue ultrastructure, nano- and micromechanical properties of the porcine sclera is studied by several techniques. In vitro enzymatic degradation of proteoglycans was conducted with α-amylase and chondroitinase ABC enzymes. Proteoglycans depleted by the enzymes were characterized by glycosaminoglycan content measurement and proteoglycan protein expression. Collagen fibril morphology and nanomechanical stiffness pre and post

enzymes were measured with atomic force microscopy. And the scleral micromechanical properties were measured by nanoindentation technique.

DMMB assays indicated that sGAG content was reduced after α-amylase and chondroitinase treatment. And significant variations were found in the scleral protein analyse pattern incubated with both enzymes. These results indicated that both enzymes could cause proteoglycan depletion in the sclera tissue. Scleral topography by AFM results shows that proteoglycan depletion will lead to a reduction of collagen fibrils size, however not affect the collagen fibril D-periodicity. The mechanical results by AFM and nanoindentation show that proteoglycan depletion leads to significant reduction in both nanoscale and microscale mechanical properties of the sclera. However, there are regional differences in both structure and mechanical proteoglycan between results treated with amylase and chondroitinase.

List of Publications

Zhuola, L., Kharaz, Y., Comerford, E. and Akhtar, R., 2017, June. Nano-structure and mechanical changes in sclera following proteoglycan depletion. In INTERNATIONAL JOURNAL OF EXPERIMENTAL PATHOLOGY (Vol. 98, No. 3, pp. A11-A11).

Kearns, V.R., Tasker, J., Zhuola., Akhtar, R., Bachhuka, A., Vasilev, K., Sheridan, C.M. and Williams, R.L., 2017. The formation of a functional retinal pigment epithelium occurs on porous polytetrafluoroethylene substrates independently of the surface chemistry. Journal of Materials Science: Materials in Medicine, 28(8), p.124.

Chen, R., Curran, J., Pu, F., Zhuola, Z., Bayon, Y. and Hunt, J.A., 2017. In Vitro Response of Human Peripheral Blood Mononuclear Cells (PBMC) to Collagen Films Treated with Cold Plasma. Polymers, 9(7), p.254.

Mears, L.L., Draper, E.R., Castilla, A.M., Su, H., Zhuola., Dietrich, B., Nolan, M.C., Smith, G.N., Doutch, J., Rogers, S., Akhtar, R. and Cui, H., 2017. Drying affects the fiber network in low molecular weight hydrogels. Biomacromolecules, 18(11), pp.3531-3540.

Zheng Z, Chang Z, Xu GK, McBride F, Ho A, Zhuola Z, Michailidis M, Li W, Raval R, Akhtar R, Shchukin D. Microencapsulated phase change materials in solar-thermal conversion systems: understanding geometry-dependent heating efficiency and system reliability. ACS Nano. 2016 Dec 23;11(1):721-9.

Conference Presentations

Zhuola, Eithne Comerford, and Riaz Akhtar (2017). Nano-Structure and Mechanical changes in Sclera following Proteoglycan Depletion. PPT presentation at The Minerals, Metals and Materials Society(TMS) 2017 Annual Meeting &Exhibition. San Diego, California, USA

Zhuola, Yalda Ashraf Kharaz, Steve Barrett, Eithne Comerford, and Riaz Akhtar (2017) Nano-Structure and Mechanical properties mapping in Sclera following Proteoglycan Depletion. Poster presented at British Society for Matrix Biology (BSMB) Matrix Proteoglycans – active participants in cell-ECM communication. Oxford, UK

Zhuola, Eithne Comerford, and Riaz Akhtar (2016) Nanomechanical properties mapping in the Sclera following Proteoglycan Depletion. Poster presented at Annual Scanning Probe Microscopy (SPM) conference meeting. Cambridge, UK

Zhuola, Yalda Ashraf Kharaz, Steve Barrett, Eithne Comerford, and Riaz Akhtar (2016) Nanomechanical Changes in the Sclera following Proteoglycan Depletion. Poster presented at 5th International Conference of Bionic Engineering. Ningbo, P.R.China.

Zhuola, Yalda Ashraf Kharaz, Steve Barrett, Eithne Comerford, and Riaz Akhtar (2016) Multi- scale mechanical properties mapping in sclera following Proteoglycan depletion. Poster presented at Annual University of Liverpool Poster day online. Won second place poster commended by the Faculty judges

Contents

List of Publications iii

Conference Presentations iv

List of Figures vi

List of Tables xv

Chapter 1: Introduction 1

1.1 Background 1

1.2 Aims and Objectives 2

1.2 Layout of the thesis 3

Chapter 2: Literature Review 5

2.1 Introduction 5

2.2 The sclera 6

2.2.1 Scleral Anatomy 6

2.2.2 Composition of the sclera 7

2.2 Sclera in ageing and disease 18

2.2.1 Sclera in the ageing process 18

2.2.2 The sclera and glaucoma 19

2.2.3 The sclera and myopia 21

2.2.4 Animal models for vision science 23

2.3 3D-Imaging measurement of scleral ultrastructure 24

2.3.1 Scanning Electron Microscope (SEM) and Tunneling Electron Microscope (TEM) 24

2.3.2 Atomic force microscopy 27
2.4 Mechanical testing of the sclera 30
2.4.1 Uniaxial tensile testing 31
2.4.2 Inflation testing 34
2.4.3 Nanoindentation 35
2.4.4 Atomic force microscopy for Mechanical Testing 40
2.5 Summary 45
Chapter 3 47
3.1 Introduction 47
3.1.1 Proteoglycan in connective tissue 47
3.1.2 Proteoglycan in the sclera 49
3.1.3 Enzymes used in the proteoglycan research in ocular tissue 53
3.2 Methods 53
3.2.1 Sample preparation 53
3.2.2 Coomassie blue staining 55
3.2.3 Dimethylmethylene blue (DMMB) assay 56
3.2.4 Data analysis and statistics 57
3.3 Results and Discussion 57
3.3.1 Regional analysis of PG core proteins 57

3.3.2 Regional analysis of s-GAG quantification 60

3.4 Conclusion 68

Chapter 4 Collagen fibril Structure Mapping with AFM 69

4.1 Introduction 69

4.2 Method 73

4.2.1 Sample preparation 73

4.2.2 AFM Peakforce QNM in air 74

4.2.3 Image processing and analysis 78

4.2.4 Data analysis and statistics 81

4.3 Results 81

4.4 Discussion and Conclusion 89

Chapter 5 Mechanical properties mapping following proteoglycan depletion 94

5.1 Introduction 94

5.2 Method 99

5.2.1 Sample preparation 99

5.2.2 Incubation buffers 100

5.2.3 AFM Peakforce QNM in liquid 100

5.2.4 Data analysis and statistics 103

5.3 Results 103

5.4 Discussion and Conclusion 111

5.4.1 Scleral nanomechanical change following hydration with distilled water and PBS buffer 111

5.4.2 Scleral nanomechanical change following enzyme treatment 113

Chapter 6: Mapping mechanical properties at a microscale following proteoglycan depletion by nanoindentation. 115

6.1 Introduction 115

6.2 Methods 118

6.2.1 Sample preparation and nanoindentation testing 118

6.2.2 Analysis of mechanical properties 119

6.2.3 Statistical analysis 120

6.3 Results 121

6.4 Discussion 129

6.5 Conclusion 130

Chapter 7 Conclusion 132

7.1 Summary of finding 132

7.2 Key contribution 137

Chapter 8 Limitations and future work 138

8.1 Limitations 138

8.2 future directions 139

Reference.....142

Appendix A.....153

Experimental setup and protocols.....153

SDS-PAGE Loading and running buffer.....153

Papain Digestion.....154

GAG ASSAY.....154

Pilot study for experimental setup.....155

Drawings for nanoindentation sample holder.....158

Appendix B.....162

Codings for Image processing.....162

Appendix C.....170

AFM Images.....170

Images of proteoglycan.....170

Images of collagen fibrils “fusion” after Amylase treatment.....172

Images of collagen fibrils distribution pre and post treatments.....176

List of Figures

Figure 2.1 Schematic of the human eye and path of light rays. The light signal passes through the cornea and changes direction via the lens to focus on the retina where the light signal is transformed into electrical signal. The electrical signals are then transmitted to the brain through the optic nerve…….. 6

Figure 2.1 Diagrammatic representation of the human ocular globe (right) and the corneoscleral junction in longitudinal section (left) (Foster and de la Sainz Maza, Jensen, 1982). ……..7

Figure 2.3 The organisation and production of a collagen fibril. ..……. 10

Figure 2.4 Outer layer of normal supero-temporal human sclera showing lamellar structure. ……... 11

Figure 2.5 The arrangement of collagen fibres around the sclera. Anterior to the equator, the fibres are meridional, particularly in relation to the muscle insertions. 13

Figure 2.6 Schematic of the interactions between proteoglycan and collagen fibrils. The location and structure of decorin, biglycan, aggrecan and hyaluronan are also shown. These PGs were reported to exist in the scleral matrix (Rada et al., 2015) ..15

Figure 2.7 Basic structure of proteoglycan with a chondroitin sulphate GAG sidechain. ……...16

Figure 2.8 Distributions and concentrations of heparan, dermatan and chondroitin sulphated GAGs within the sclera (right eye). ……. 17

Figure 2.9 Regional analysis of scleral proteoglycan concentration with the increase of age (Rada et al., 2015)…….. 19

Figure 2.11 Transverse sections of scleral collagen fibrils in normal, age-matched control, and highly myopic eyes, captured by scanning electron micrographs (SEM) (McBrien et al., 2001). …….23

Figure 2.12 With SEM, rectangular sections with circular section profiles (B). Oblique sections with ellipsoidal section profiles (C). The minimum profile diameter is identical in both section profiles (A).Adapted from Wollensak et al. (2004)…… 27

Figure 2.13 SEM/TEM Imaging of the sclera structure at multiple length-scales. .. 28

Figure 2.14 In an AFM, a laser beam landed on and reflected by the surface of cantilever then caught by photodetector. …….. 30

Figure 2.15 AFM images from height channel showing scleral diameter distribution across the sclera posterior (a), equatorial (b) and anterior regions (c) (Papi et al., 2014). From the images, collagen fibrils diameter from anterior region are significant greater than in posterior region…….. 31

Figure 2.16 Uniaxial tensile testing set up (a) and the liquid chamber (b). Scleral strip IS immersed in a tissue bath yields estimates of the scleral modulus. (Geraghty et al., 2015) ……34

Figure 2.17 Schematic of load-control nanoindentation: a load (P) is applied while the load-displacement and displacement-time are recorded. ……...37

Figure 2.18 Schematic of Berkovich (A), big (B) and small (C) sphere, flat punch (D) indenter tips, and their projected areas Ac. he is the contact depth, α1 is a geometric constant, and R the radius……...40

Figure 3.1 Structure of PGs (chondroitin and heparan sulphate) showing the polysaccharide-protein linkage region and the main disaccharide units. Gal, galactose; Xyl, xylose; GluA, ß-D-glucuronic acid; GalNAc, N-Acetylgalactosamine. ((Maeda, 2015)……...45

Figure 3.2 Stereo paired image of a three-dimensional reconstruction of proteoglycan (orange) and collagen fibrils (blue) from electron tomography from the sclera of an 89-year-old male donor (Watson and Hazleman, 2012b)……..48

Figure 3.3 Carbohydrate sequences of the five types of GAG chains that have been reported in the sclera using monosaccharide symbols: (A) Hyaluronan; (B) Chondroitin; (C) Dermatan; (D) Heparin; and (E) Keratan. Possible sulfation presence and location (2S, 4S, or 6S) is indicated. (Sigma-Aldrich, 2000)……...50

Figure 3.4 Schematic of porcine eye globe (left) showing the anterior (A), equatorial (E), and posterior (P) regions from where the tissue was dissected. Figure adapted from Papi et al. (2014)……. 52

Figure 3.5 SDS-PAGE patterns of α-amylase incubated scleral protein. α-amylase incubated protein from anterior (A+), equatorial (E+), and posterior regions (P+) each displayed a banding pattern distinct from the three regions from the control (A-, E- and P-). Gels were stained with Coomassie Blue…… 56

Figure 3.6 SDS-PAGE patterns of chondroitinase ABC incubated with scleral protein. ……. 58

Figure 3.7 s-GAG content measurements from anterior, equatorial, and posterior scleral regions of porcine sclera (n= 5 eyes/group). …….59

Figure 3.8 Standard deviations of s-GAG content measurement from three regions of porcine sclera. Results are divided into three experimental groups: control, α-amylase, and chondroitinase ABC…… 60

Figure 4.1 AFM images of the Type one collagen fibril surface profiles before (a), during (b), and after (c) swelling. (d) Mean of four adjacent profiles along the fibril's main axis (grey) and a sinusoidal fit (black). The collagen gap zone depth reduced when hydration level increased. (Spitzner et al., 2015) ……68

Figure 4.2 outer layer of hydrated human scleral collagen fibril diameter (C) and D-period (D) measurements using line profiling plots on AFM topography (A) and deflection images (B) in a scan size of 5 × 5 μm2.(Lee et al., 2011)…… 72

Figure 4.3 Cantilever and tip used in this study (Bruker Nano Inc.). ……73

Figure4.4 Selection of testing location. (a) This Figure shows a typical 15μm image and (b) shows a typical 7μm image. A region of collagen fibril bundle which were selected are highlighted (red oval). Testing locations (1.5μm ×1.5μm) were subsequently chosen along this bundle. …….75

Figure 4.5 AFM probe scanning start point in (a) was found with the MATLAB localization algorithm after depletion (b)……. 76

Figure4.6 (a) Collagen fibril parameters (diameter, D-periodicity, and gap-zone depth) were measured and compared with image analysis techniques in this study. A single collagen fibril was selected manually from the (b) AFM height image for the gap zone depth measurement. The contiguous height difference of peak and valley in the (c) exported curve is the value of the gap zone depth; this was calculated through an algorithm……...…… 77

Figure 4.7 Image processing and analysing method for the 'rectangle' method. …. 78

Figure 4.8 AFM images captured from same location on the same collagen bundle before and after treatment with distilled water…….. 80

Figure 4.9. Collagen fibril diameter results in pre- and post-buffer treatment images (n=5 porcine eyes/group)……... 81

Figure 4.10. Collagen fibrils D-periodicity results in pre- and post-buffer treatment images…….82

Figure 4.11 Collagen fibril gap zone depth results in pre- and post-buffer treatment images……83

Figure 4.12 Collagen fibrils fused after treatment with α-amylase. (a) is the 1.4 μm AFM image before incubation with α-amylase and (b) is the image captured from same location on the tissue after incubation. White arrows indicated the locations of same collagen fibrils before and after incubation…….. 84

Figure 4.13 Size 15μm images from AFM height channel captured from same locations before (a) and after (b) incubation with distilled water, PBS buffer and chondroitinase ABC……...86

Figure 4.14 Collagen fibril bundles "split up" after α-amylase treatment. (a) is the 15μm AFM image before incubated with α-amylase and (b) is the image captured from same location on the tissue after incubation. White arrows indicated the locations of same collagen fibril bundles before and after incubation……. 87

Figure 4.15 3D Schematic (c) of collagen and proteoglycan interaction based on AFM images. The small objects between the collagen fibrils in image (a) are interfibrillar proteoglycan. The selected area image (b) shows suspected big size proteoglycan……...88

Figure 4.16 Collagen fibrils structures in highly myopic eyes captured by previous studies: (a) Comparison between a normal, control, and highly myopic eye. Collagen fibrils became irregular in size, and abnormally small collagen fibrils are increased in all scleral layers in highly a myopic eye (McBrien et al., 2001). (b) ''Star'' shape

collagen fibrils found in the cornea of a highly myopic eye (Harper and Summers, 2015a)…….91

Figure 5. 1. The operating principle of a Bruker multi-mode AFM with peakforce QNM mode scanning sample surface. The force-distance curve at each tapping pixel is defined by: surface approach (1–2), point of deepest indentation (3), force release and surface restoration (4) and released cantilever (5)……..95

Figure 5. 2 (a) Plot of force and Z position as a function of time (b). A force curve eliminates the time variable, plotting Force vs. Z position. Edited from Veeco Instruments Inc. (2010)…….96

Figure 5. 3 Schematic diagram of the porcine eye globe (left) showing the anterior (A), equatorial (E) and posterior (p) regions from where the tissue was dissected. Tissue was sectioned vertically and numbered sequentially; probe location images captured in this Figure show that same location of the specimen (upper inner corner) was selected as the testing location for one repeat of samples for four groups…… 99

Figure 5.4 AFM PeakForce QNM image with size 7μm2 from height channel (left), 2D (middle) and 3D (right) DMT Modulus channel……103

Figure 5. 5 Elastic modulus changes following buffer treatment in all scleral regions. ……104

Figure 5. 6 Elastic modulus result following four treatments in scleral anterior regions……..105

Figure 5. 7 Elastic modulus result following four treatments in scleral equatorial regions……106

Figure 5. 8 Elastic modulus changes following buffer treatment in scleral posterior regions……..107

Figure 5. 9 Decrease of elastic modulus in all three regions after being incubated with chondroitinase ABC. ……..108

Figure 5. 10 Decrease of elastic modulus in all three regions after being incubated with α-amylase……109

Figure 5. 12 Increase of the elastic modulus of collagen fibrils as a function of NaCl concentration. (Grant et al., 2009)…….. 111

Figure 6.1. Scleral collagen fibrils and tissue matrix structure at the nanometer and micrometre scale observed by AFM and TEM. PG= Proteoglycan; F= Fibroblast; Mf=Micro fibril (Komai and Ushikif, 2015)……116

Figure 6.2. Shear storage modulus G′ for specimens from the three regions after treatment with control and chondroitinase ABC buffer……. 122

Figure 6.3 Shear storage modulus G′ for specimens from the three regions after treatment with control and ∝-amylase buffer. ……123

Figure 6.4 Shear loss modulus G′ for specimens from the three regions after treatment with control and chondroitinase ABC buffer…….. 124

Figure 6.5 Shear loss modulus G´ for specimens from the three regions after treatment with control and ∝-amylase buffer. ……..125

Figure 6.6 The loss factor for specimens from the three regions after treatment with control and chondroitinase ABC buffer. ……126

Figure 6.7 The loss factor for specimens from the three regions after treatment with control and ∝-amylase buffer. ……127

List of Tables

Table 2.1 Collagen types within sclera (McGurk et al. 2013, Meek KM 2008)……. 9

Table 3.1 PGs in the sclera and their core protein weight, apparent molecular masses, and s-GAG chains.(Young et al., 2003, Kurylo et al., 2016, Michelacci et al., 2003, Dunlevy and Rada, 2004). (CS: Chondroitin Sulphate, DS: Dermatan Sulphate, KS: Keratan Sulphate, HS: Heparan Sulphate)…… 64

Table 4.2 Collagen types within the sclera (Meek, 2008, Shoulders and Raines, 2009, Karsdal et al., 2016)……..67

Table 4.2 Morphological characteristics of scleral collagen fibres studied by various techniques. ……71

Table 5. 3 Information for the cantilever and tip used in this study (Bruker Nano Inc.)

……..100

Table 5. 4 Comparison of mechanical outcome, expressed as a mean value with the standard error of mean, p-value and difference in percentage between pre and post-buffer treatment. …….110

Table 6.1 Results of the shear storage modulus, G′ , shear loss modulus, G″ , and the loss factor from each group, presented as mean value, standard error of mean

(SE), statistical significance (Student ’ s t-test, p) and reduction compared to control. …….128

Table 7.1 The outcome summary of this study. Modulus Changes found in the sclera tissue after enzyme incubations by different technique approaches…..138

Abbreviation

AFM	Atomic force microscopy
CS	Chondroitin Sulphate
CSM	Continuous Stiffness Measurement
DMMB	Dimethylmethylene blue
DS	Dermatan Sulphate
ECM	extracellular matrix
GAG	Glycosaminoglycans
HS	Heparan Sulphate
IOP	Intraocular Pressure
KS	Keratan Sulphate
OCT	optimal cutting temperature
ONH	optic nerve head
PBS	phosphate buffered saline
PDMS	Polydimethylsiloxane
PeakForce QNM	PeakForce Quantitative Nanomechanical Mapping
PGs	proteoglycans
PS1	Photostress coating 1
RGCs	retinal ganglion cells
SD	Standard deviation
SEM	Standard error mean
SDS-PAGE	sodium dodecyl sulphate-polyacrylamide gel electrophoresis
SEM	Scanning electron microscope

TEM	Transmission electron microscopy

Chapter 1: Introduction

1.1 Background

Myopia, or short-sightedness, is the most common eye disorder that cause distant objects to appear blurred, while close objects can be seen clearly. Preliminary projections from the World Health Organization (WHO) based on prevalence data indicated that myopia will affect 52% of the world's population by 2050(Murienne et al., 2015). One of the potentially blinding ocular diseases associated with myopia is glaucoma. The mechanical stresses induced by increased axial length of the globe and oxidative stress are implicated in the development of glaucoma in myopic eyes(Marcus et al., 2011). Glaucoma is an optic neuropathy that causes progressive, irreversible visual field loss and is the second leading cause of blindness(Murienne et al., 2016).

The sclera is the main load-bearing structure of the eye. It resists intraocular pressure (IOP) and external forces. The sclera maintains the shape of the eye and protects the more delicate intraocular structures such as the retina and choroid. The mechanical properties of the sclera have been suggested to play a vital role in the initiation and development of glaucoma and myopia. Mechanical changes in the sclera can significantly influence susceptibility to development of these diseases even at normal IOP. Understanding how the components of the sclera contribute to its mechanical properties is crucial for understanding the role of these components in the pathophysiology of myopia and glaucoma. In turn, this could lead to the development of new treatments in the long-term. Although the main role of collagen in the biomechanics of biological tissue is known, the role of proteoglycan variation through the whole sclera has yet to be studied. Furthermore, the pathological changes

in scleral glycosaminoglycan (GAG) content along with mechanical properties have been observed independently in aged, glaucoma, and myopic eyes. (Norton and Rada, 1995, Rada et al., 2015, Knepper et al., 1996) However, the impact of GAG content variation in mechanics and tissue structures in all scleral regions has not been determined.

The triggering of specific structural and mechanical changes is beneficial for specific diseases such as glaucoma or myopia. This could represent the next generation of eye treatments in an effort to avoid surgical interventions. Currently, most studies of the function of scleral proteoglycan are a focus on the posterior region and few have studied the contribution of proteoglycan in mechanical behaviour of whole sclera. The alteration in posterior sclera shape is caused by the difference in regional mechanical response to pressure, and there is also regional variation in proteoglycan distribution. Thus, it is necessary to study the structure and mechanical role of proteoglycan in the whole sclera to fill the gap.

1.2 Aims and Objectives

The main goal of this study is to investigate the contribution of sulphated proteoglycans to the tissue structure and corresponding mechanical properties of all regions of sclera using experimental approaches. This work aims to investigate porcine sclera as a model of human sclera for tissue structure and mechanical properties changes following proteoglycan depletion in scleral anterior, equatorial and posterior regions. This aim required the following objectives to be accomplished:

- The first objective of this study was to characterise the effect of enzymatic degradation using chondroitinase ABC and α-amylase on scleral

proteoglycans across the three different regions. These two enzymes have been used previously for scleral proteoglycan depletion in mechanical studies.

- The second objective was to characterise the effect of proteoglycan depletion by the same enzymes on the sclera nanostructure focussing on collagen fibrils, across the three different regions.
- The final objective was to characterise the effect of proteoglycan depletion on sclera the mechanical properties across all three regions focussing on the nanometer and micrometre scale.

1.2 Layout of the thesis

In addition to this introduction, this thesis is composed of seven chapters, the contents of which are summarised below.

Chapter 2 provides background information on sclera topography and composition relevant to this study. A brief description on sclera in ageing and disease is provided, followed by a review of the literature in both scleral structure and studies of mechanical properties.

In **Chapter 3,** scleral sGAG content in all three regions was determined in this chapter using the DMMB assay and the proteoglycan protein expression was observed from in-gel Coomassie blue staining. The aim of this chapter is to provide a better understanding of the effect of these two enzymes on scleral regions, especially the effect of α-amylase on scleral proteoglycans.

Chapter 4 explores the nanostructure (diameter, D-periodicity, and gap zone depth) of scleral collagen fibrils as captured by atomic force microscopy (AFM). The

scleral collagen fibrils nanostructure parameters were analyzed from AFM images with image analyzing software then compared between control and enzymes-treated groups.

Chapters 5 and **6** evaluate the contribution of proteoglycans to the mechanical behaviour of the three regions in the porcine sclera. To determine the mechanical properties of the sclera, properties including surface elasticity and adhesion. Due to the multiscale organisation of biological tissues like the sclera, the mechanical response can vary according to different length-scale observations. The sclera tissue were tested with AFM in liquid in **Chapter 5** to measure tissue fibril mechanical properties at the nano-level. The testing in this chapter was performed under the same room temperature and with the same spatial resolution as in Chapter 4. Also the same enzyme groups and incubation durations were used in this chapter in order to have consistent result with Chapter 4. Scleral matrix mechanical properties were measured at a microscale with a nanoindentation technique in **Chapter 6,** under the same room temperature with the same enzymes and for the same incubation durations. The results of mechanical properties were compared between control and enzyme-treated groups.

Chapter 7 summarises and discusses the key results from this study. **Chapter 8** concludes the findings and highlights the main limitations of this work, and closes with future research perspectives.

The appendix contains further details on the experimental procedures and designs, as well as the coding for image processing and data analysing methods using MATLAB and Image SXM.

Chapter 2: Literature Review

2.1 Introduction

The eye is the organ of sight that transforms light signals into electrical signals. These signals are then transmitted to the brain, where they are interpreted to form an image. For an object within human eyesight, the light reflected from the object travels in the eye, goes through the cornea, and its angle is changed by the lens and focused onto the retina (Figure 2.1). To adapt for object distance, the ocular lens adjusts its curvature, bending the light rays to a precise length. Failure to focus light waves on the retinal surface could result in blurred vision. Object information is first encoded into electrical signals by specialised photoreceptor cells in the retina, before the signals are transmitted to the retinal ganglion cells (RGCs) whose axons exit the eye through the optic nerve head (ONH) to transmit the electrical signal to the brain.

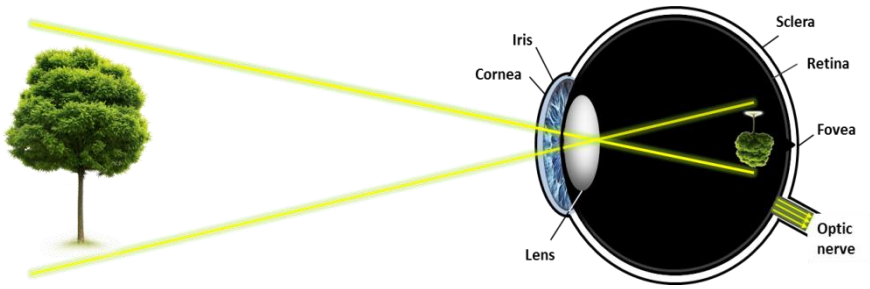

Figure 2.1 Schematic of the human eye and path of light rays. The light signal passes through the cornea and changes direction via the lens to focus on the retina where the

light signal is transformed into electrical signal. The electrical signals are then transmitted to the brain through the optic nerve (Figure drawn by the author).

2.2 The sclera

2.2.1 Scleral Anatomy

The sclera is the white part of the eye (Figure 2.2) that extends between the cornea and the optic nerve. It comprises one-fifth of the eye, commencing anteriorly at the limbus and ending posteriorly at the optic nerve. It is near spherical with an approximate surface area of 16.3 cm^2 (Olsen et al. 1998) and a typical radius of 11.5 mm (Forrester et al. 1990). The sclera is characterised by a relatively homogenous thickness in infants until the age of 4 to 5 years when the posterior region begins to thicken and the equatorial region becomes relatively thin compared to other regions (Avetisov, Savitskaya & Vinetskaya 1983). Scleral thickness in adult humans has been shown to decrease from approximately 500-600 μm at the limbus (corneoscleral junction) to 400-500 μm at the equator before increasing to values in the region of 1000 μm near the optic nerve in the posterior region (Olsen et al. 1998, S, S & JB 2012). This trend for regional variation was also observed in porcine sclera (Timothy et al. 2002). The sclera encroaches slightly more into the cornea in the superior and inferior quadrants than it does laterally, but the internal diameter of the scleral foramen is circular at 11.6 mm (Watson et al. 2004).

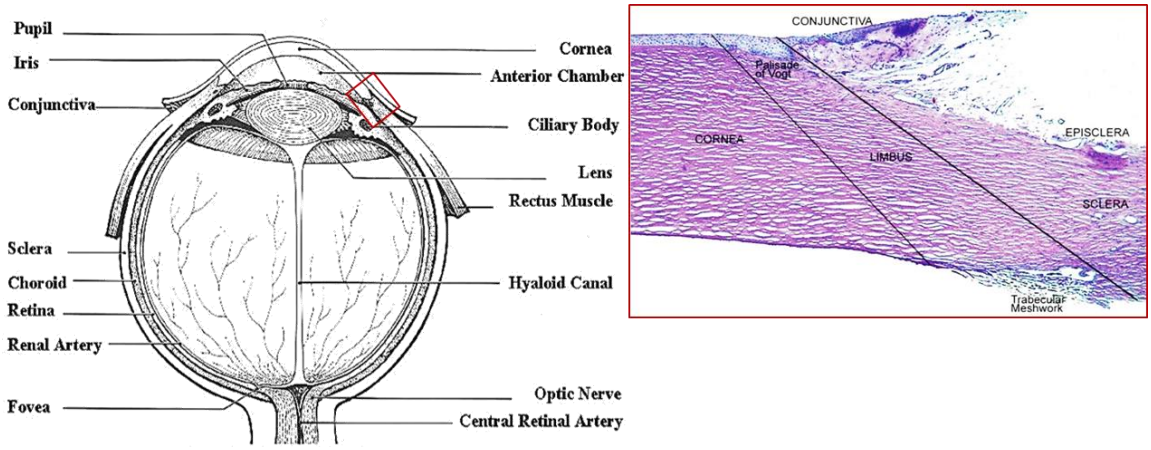

Figure 2.2 Diagrammatic representation of the human ocular globe (right) and the corneoscleral junction (limbus) in longitudinal section (left) (Foster and de la Sainz Maza, Jensen, 1982).

The sclera is primarily composed of collagen; the human sclera contains approximately 50% collagen by weight (Campbell et al., 2014). In all species, the main collagen fibrils are Type I; 90% of fibrils in human sclerae are Type I. The mechanical properties of the sclera are highly influenced by the microstructural arrangement of the collagen fibrils. There are a small amount of proteoglycans (PGs) in the sclera (<1 %), but a number of studies have suggested that these play an essential role in the biomechanical behaviour of the sclera(Chen et al., 2014). The lack of PGs results in the significant reduction of the slope of low strain in the stress-strain relationship and stress levels at consecutive stretch cycles (Eshel et al., 2001).

2.2.2 Composition of the sclera

The extracellular matrix (ECM) of the sclera is composed of three main structural components: collagen, elastin, and PGs. These are produced and degraded by scleral fibrocytes (Rada et al., 2000a).

Collagen

All types of collagen are formed of collagen molecules, each one made of a triple helix of polypeptide chains. Collagen represents 80% of the dry weight of the sclera. Different types of collagen are found in the human sclera, which are divided into 4 classes based on their supramolecular arrangement: fibril-forming collagens (types I, III, V), fibril-associated collagens (type XII), network-forming collagens (types IV, VI, VIII), and cell-associated transmembrane collagens (type XIII) (Jerome, A,J, La,Tessa. & H 1957, Keeley, Morin & Vesely 1984). Among these collagens, type I mainly contribute to the tensile strength of the biological tissue. Type III collagen is considered essential for the structural maintenance of expansible organs (such as arteries and lungs). Type V collagen is thought to have a similar function with PGs in controlling fibril diameter. Type V and VI are found outside fibrils, often separating the filaments from blood vessels and nerves. The structures and main functions of these collagen types are presented in Table 2.1.

Table 2.1 Collagen types within sclera (McGurk et al. 2013, Meek KM 2008)

Type	Structure	Class	Representative tissues	Main function
I	300nm molecule length, 67nm banded fibrils	Fibrillar	Skin, tendon, bone, dentin	Resistance to tension
III	67nm banded fibrils	Fibrillar	Skin, muscle, blood vessels, frequently together with type I	Structural maintenance in expansible organs
V	390nm molecule, N-terminal globular domain	Fibrillar	Fetal tissues, skin, bone, placenta, most interstitial tissues	Participates in type I collagen function
XII	Large N-terminal domain; interacts with type I collagen	FACIT (Fibril Associated Collagens with Interrupted Triple helices)	Embryonic tendon and skin	Interacts with type I collagen

VI	Non-fibrillar collagen	Network	Underlying epithelial, endothelial, fat, muscle and nerve cells	Maintaining tissue integrity

Type I collagen is the most abundant in the sclera (Meek, 2008). It is characterised by cross-striated fibrils with a D-band periodicity of 67 nm (Figure 2.3) that are stabilised by covalent intramolecular and intermolecular crosslinks. The collagen fibril size distribution in humans is similar in the anterior and posterior sclera (Foster and de la Sainz Maza) but is smaller in the peripapillary region (Downs et al., 2005) (the sclera adjacent the optic nerve head). The fibrils of the outer human sclera (closer to the ocular cavity) are on average larger in diameter (58-160 nm) than those of the inner sclera (50-76 nm, closer to the choroid) (Young, 1985a).

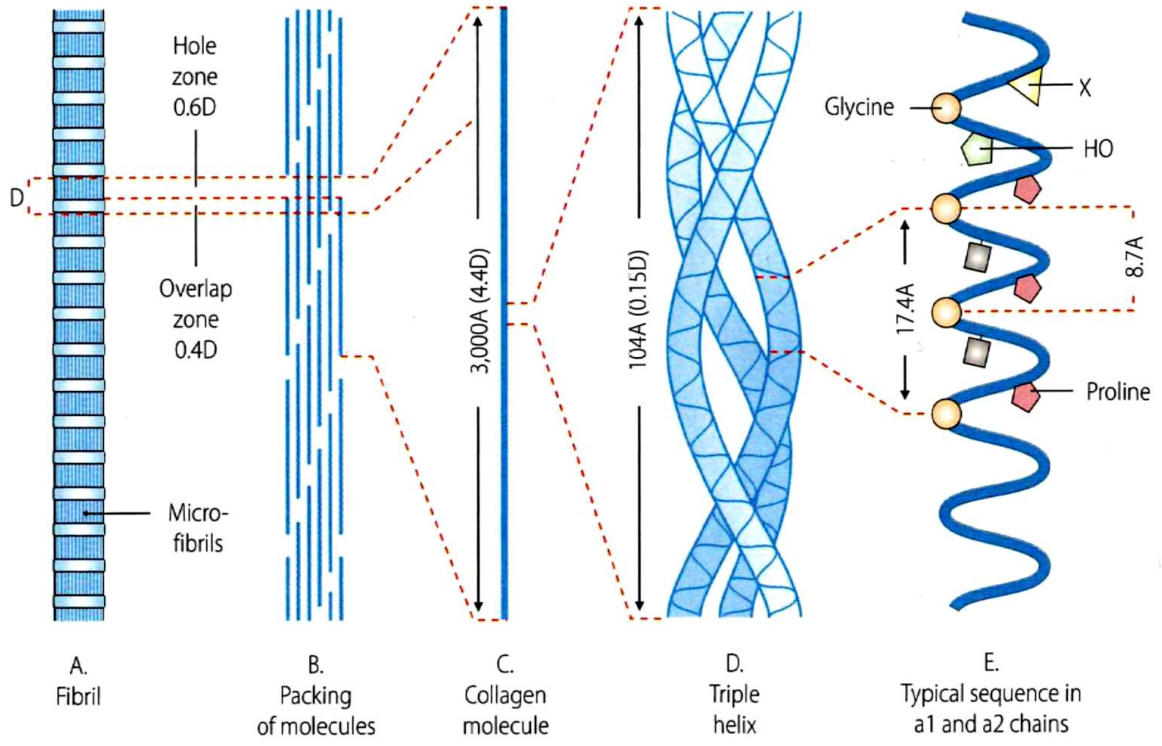

Figure 2.3 The organisation and production of a collagen fibril. Within the fibril, collagen molecules of length 300 nm and width 1.5 nm are staggered concerning

their neighbours by multiples of *D*. A single molecule is formed from three polypeptide chains, called α-chains (Watson and Hazleman, 2012).

The fibril bundles in sclera do not follow the same arrangement of the organised orthogonal arrangement as they do in the cornea (Komai and Ushik, 1991). Instead, they have been shown to be interwoven in a more irregular and complex pattern with lamellae dimensions up to 50 μm wide and six μm thick with increasing interweaving and density towards the inner regions (Young, 1985) (Figure 2.4).

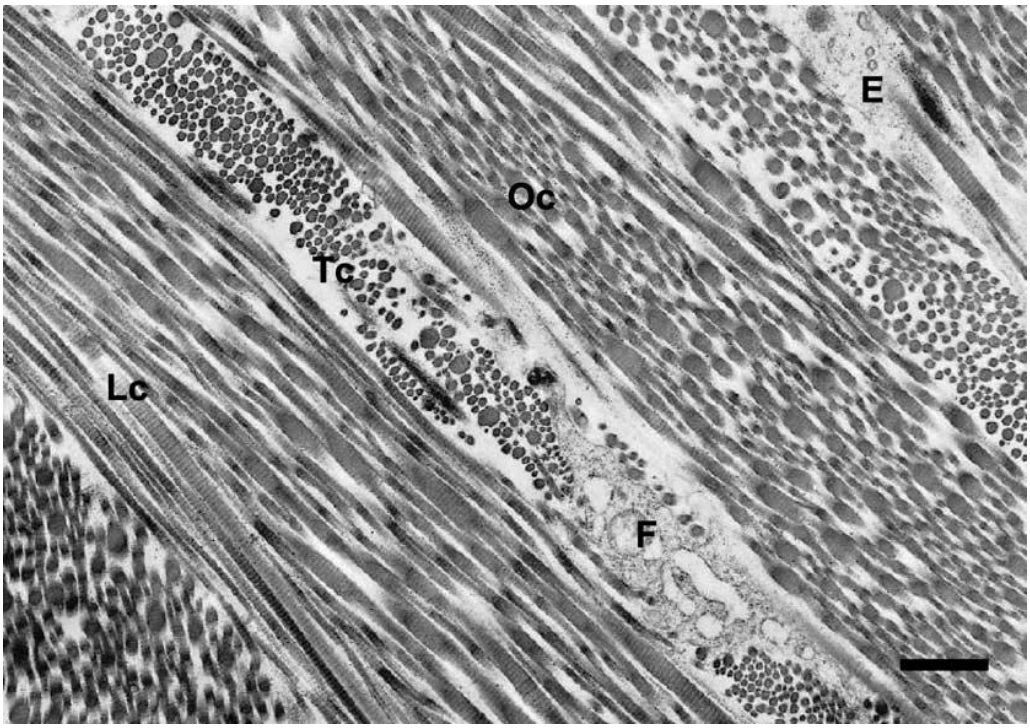

Figure 2.4 Outer layer of normal supero-temporal human sclera showing lamellar structure. Presented in longitudinal (Lc), transverse (Tc) and oblique (Oc) sections with the variation in fibril diameter evident. Fibrocytes (F) and elastin fibres (E) also visible (scale bar ≈ 1.5 μm) (Watson and Young, 2004).

The lamellae are circumferentially oriented at the limbus and in the outer peripapillary region but radially arranged in the inner peripapillary region (Newton and Meek, 1998). Elsewhere, the lamellae form reticular patterns in the outer sclera

and rhombic patterns in the inner sclera, where they are more interwoven (Komai and Ushikif, 2015). The lamellae of the outer human sclera are on average thinner (0.5-2 µm) and narrower (1-5 µm) than those of the inner sclera (0.5-6 µm thin, 1-50 µm wide). Scleral fibroblasts are mostly located between the collagen lamellae (Watson et al. 2004). Elastic fibres and elastin microfibrils are occasionally seen between or within collagen bundles (Komai, Ushik 1991).

The bundles of collagen fibrils tend to be fusiform in shape and branch dichotomously, with each tapering end entering another fasciculus (Komai and Ushik, 1991). This format gives great strength and enables the structure to conform to the stress and strain imposed on it by the extraocular muscles. As shown in Figure 2.5, collagen bundles behind the limbus are slightly curved with the concavity directed forwards.

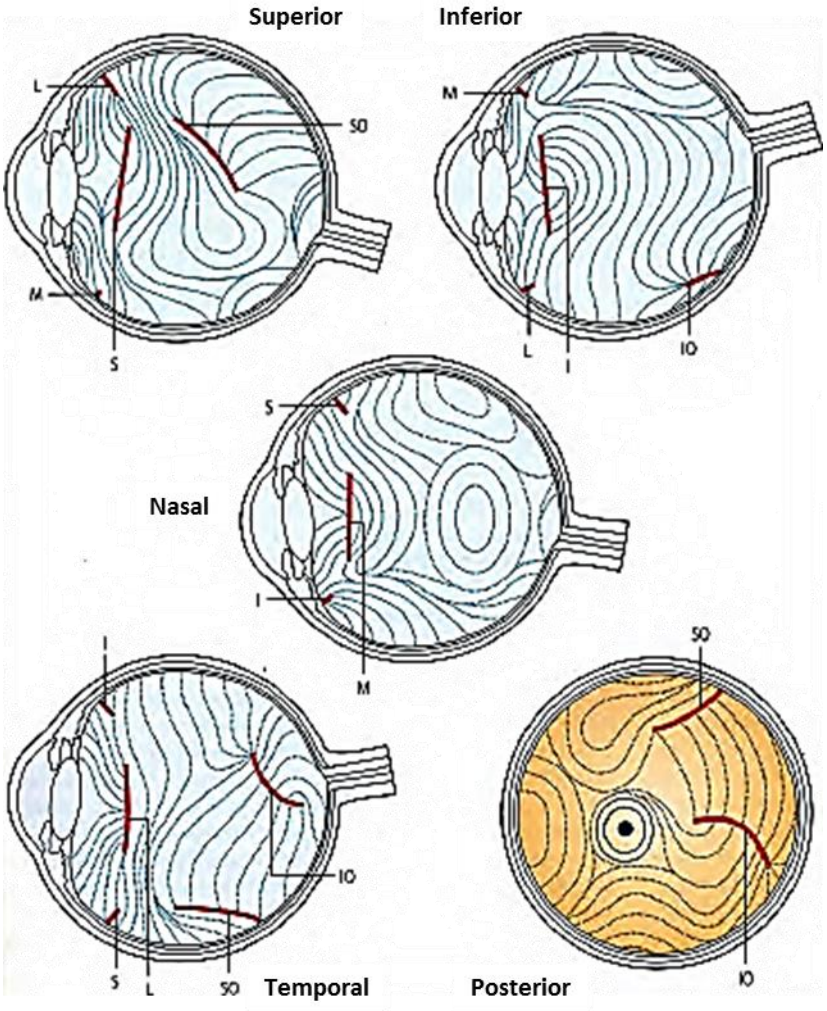

Figure 2.5 The arrangement of collagen fibres around the sclera. Anterior to the equator, the fibres are meridional, particularly in relation to the muscle insertions. (S: superior rectus muscle; I: inferior rectus muscle; M: medial rectus muscle; IO: inferior rectus muscle; SO: superior oblique muscle) (Kokott, 1934).

Elastin

Elastin fibres in the sclera are interwoven between collagen fibrils and comprise 2% of the dry weight of the sclera (Meek, 2008). Elastin fibres consist of multiple elastin molecules crosslinked through covalent bonding. They are surrounded by longitudinal microfibrils formed of the glycoprotein. The elastin core and elastin microfibrils have been shown to interact directly with collagen and PGs, or through

bridging molecules. Elastin fibres are circumferentially arranged with a 300 μm region around the ONH in humans, showing no preferred arrangement elsewhere. Distal to the peripapillary sclera, elastin fibres are predominantly found in the inner sclera where their density decreases. The average diameter of the elastin fibres varies with age in humans. At 2-3 years old their diameter is 12 nm; this can increase to 20 nm at 80 years old (Kanai and Kaufman, 1972). Biochemical analysis has shown the elastin component of the adult human sclera to be around 2% by weight, although this increases to 5% in the scleral spur and trabecular meshwork (Moses RA et al. 1978).

Proteoglycans

Proteoglycans (PGs) are composed of GAGs attached to a core protein through covalent bonding and they form the ground substance in which the collagen fibrils and elastin fibres are embedded. GAGs are polysaccharide chains of various lengths consisting of repeating disaccharide units. Figure 2.6 shows an image of a proteoglycan captured with atomic force microscopy (AFM). PGs core proteins make up of 2% of the dry weight of the sclera(Ayad et al., 1998), while GAGs represent 0.5 to 1%(Breen et al., 1972).

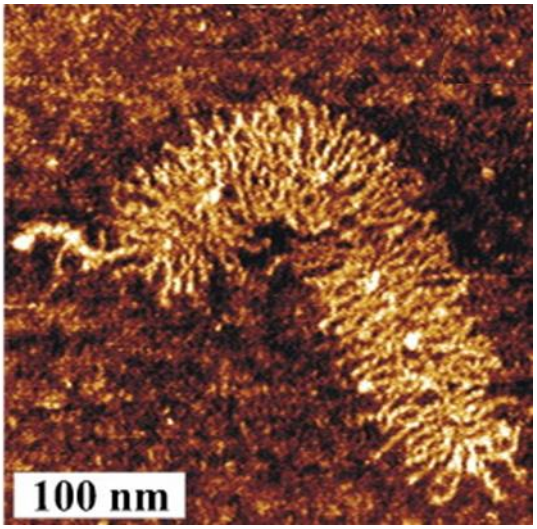

Figure 2.6 AFM images of molecular brushes: proteoglycans having a protein backbone with glycosaminoglycans side chains(Peng and Bhushan, 2012)

As shown in Figure 2.7, proteoglycans consist of a protein core to which at least one s-GAG side-chain is attached through a linkage region (Watson et al. 2004). There are mainly three types of sulphate found in sclera: chondroitin sulphate, dermatan sulphate, and heparin sulphate. Anionic groups on GAG sidechains of matrix PGs have been exploited to visualise scleral PGs and their collagen associations, using cationic dyes such as cuprolinic and cupromeronic blue (Van Kuppevelt et al. 1987).

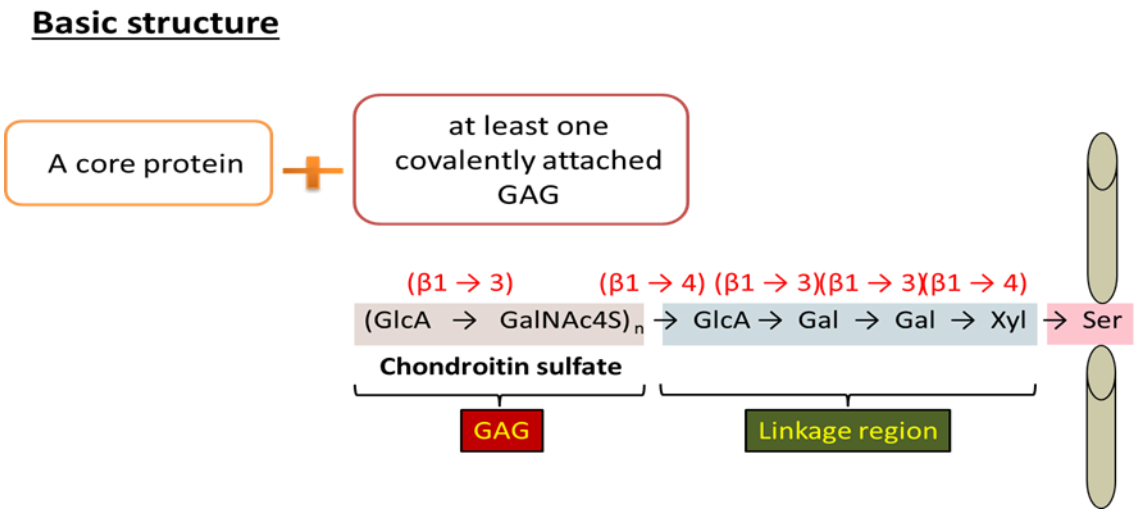

Figure 2.7 Basic structure of proteoglycan with a chondroitin sulphate GAG sidechain.

The interfibrillar compartment in the scleral matrix is occupied primarily by PGs, mainly decorin and biglycan. Small PGs are also believed to regulate collagen fibril assembly and interactions. Human sclera also contains small amounts of the large PG aggrecan (Rada et al., 1997). Collagen fibrils and PG interactions are shown in Figure 2.8. The most abundant PG in human sclera is decorin (which represents 74%) followed by biglycan (20%) and aggrecan (6%) (Rada et al., 1997). Decorin (≈ 45kDa core) has a single chondroitin sulphate or dermatan sulphate glycosaminoglycan (GAG) side chain, while biglycan (≈ 45kDa core) has two side chains of chondroitin sulphate and/or dermatan sulphate GAG. Aggrecan is the largest PG (≈ 350kDa core), consisting of up to 100 chondroitin sulphate and 30 keratan sulphate side chains (Rada et al., 1997).

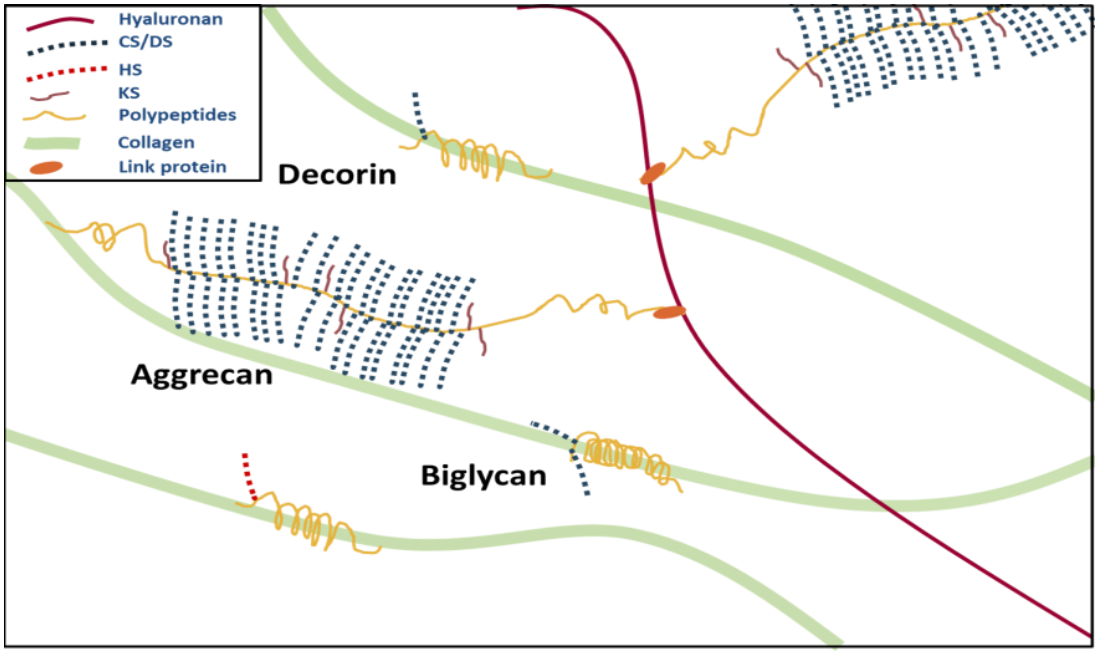

Figure 2.8 Schematic of the interactions between proteoglycan and collagen fibrils. The location and structure of decorin, biglycan, aggrecan and hyaluronan are also shown. These PGswere reported to exist in the scleral matrix (Rada et al., 2015)

Among the GAGs, dermatan sulphate and hyaluronic acid are the most abundant in the sclera, followed by chondroitin sulphate, keratan sulphate, heparin sulphate, and heparin (Clark et al., 2011). Hyaluronic acid is unsulphated and not associated with core proteins, thus providing binding sites for aggrecan (Varki et al., 2009). The human sclera also contains a small amount of lumican (≈ 70kDa core) (Johnson et al., 2006), another member of the SLRP family with a short unsulphated lactosaminoglycan side chain (Dunlevy and Rada, 2004). Other core proteins have also been identified in the human sclera (Johnson et al., 2006) such as proline-arginine-rich end leucine-rich protein (PRELP), fibromodulin, osteoglycin, and chondroadherin. GAGs usually adopt a linear rather than globular conformation, filling the space between collagen fibrils and the collagen-elastin network (Raspanti

et al., 2008). PGs such as decorin and lumican can bind collagen (including type I collagen) through their core protein (Vogel et al., 1984, Hedbom and Heinegård, 1993, Pogany et al., 1994, Raspanti et al., 2008). However, the aggrecan's core protein was observed between the collagen fibre and lamellae rather than in close association with collagen fibrils (Rada et al., 2006). Other PGs, such as biglycan, also interact with collagen via their GAG side chains through electrostatic interactions as shown *in vitro*.

The proportion of PGs and GAGs vary significantly in different regions of the sclera. Chondroitin sulphate increases from the equator to the posterior region and reaches the maximum concentration at 2 mm around the fovea. The peripapillary area contains a high concentration of dermatan sulphate. The concentration of heparin sulphate is low throughout the sclera but highest in the anterior region to the equator, especially in the nasal limbus (Trier et al., 1990). Concentrations and distributions of GAGs in sclera are shown in Figure 2.9.

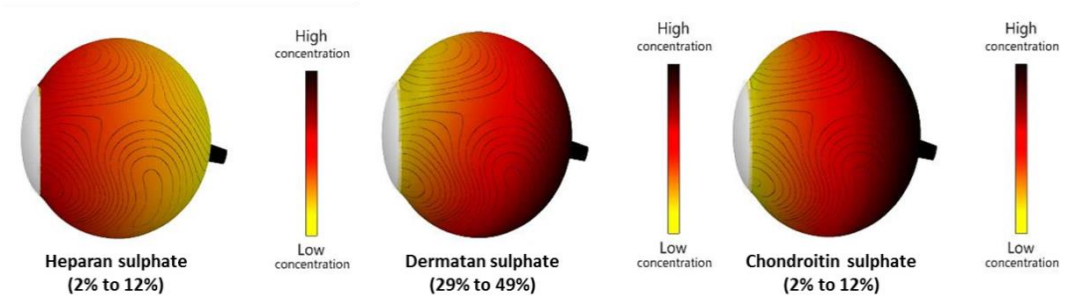

Figure 2.9 Distributions and concentrations of heparan, dermatan and chondroitin sulphated GAGs within the sclera (right eye). Keratan sulphated GAGs have been reported in the human sclera (Keenan et al., 2012b), but their regional distribution has not been studied.

Through their interactions with collagen, PG core proteins and side chains are believed to regulate collagen fibrillogenesis, including the regulation on collagen fibril structure, diameter, and fibril density (Robinson et al., 2017, Wang et al., 2015).

2.2 Sclera in ageing and disease

2.2.1 Sclera in the ageing process

The colour of human sclera changes with age, becoming darker, redder, and yellower (Russell et al., 2014). Scleral thickness has been reported to significantly decrease in the aged human sclera (Vurgese et al., 2012). This trend of decrease has also been observed in porcine eyes (Timothy et al., 2002). Mechanical properties of sclerae have also been reported to change with age. Although tissue stiffness increases with age (Geraghty et al., 2015), the stiffness of collagen fibres decrease (Coudrillier et al., 2015a). In the human sclera, the concentration of all three PGs increases significantly from birth to the fourth decade of life (Figure 2.10). Decorin and biglycan decrease in all scleral regions after the fourth decade. However, aggrecan is not significantly reduced with the increase of age (Rada et al., 2015).

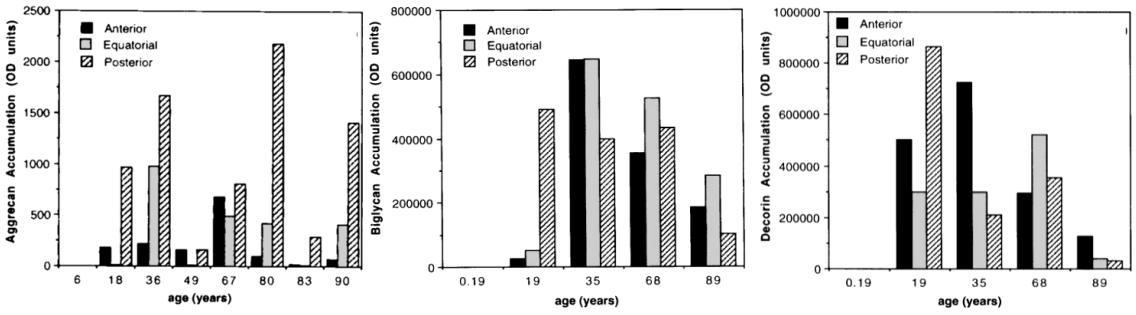

Figure 2.10 Regional analysis of scleral proteoglycan concentration with the increase of age (Rada et al., 2015).

2.2.2 The sclera and glaucoma

Glaucoma is the second leading cause of blindness worldwide, with the patient population expected to reach 80 million by 2020 (Quigley and Broman, 2006). Glaucoma is an optic neuropathy characterised by progressive and irreversible visual field loss of retinal ganglion cell (RGC) axons followed by visual field loss. An insult to the RGC axons occurs in the lamina cribrosa (LC) and the connective tissue of the optic nerve head (ONH). In the early stage of disease, the LC and peripapillary sclera move posteriorly as the opening of the posterior scleral canal increases (Quigley et al., 1981). As the disease progresses, the anterior laminar beam fails, and the LC compresses. The LC insertion into the sclera moves posteriorly, leading the characteristic "excavated" shape of the optic disk (Quigley et al., 1983). (Figure 2.11)

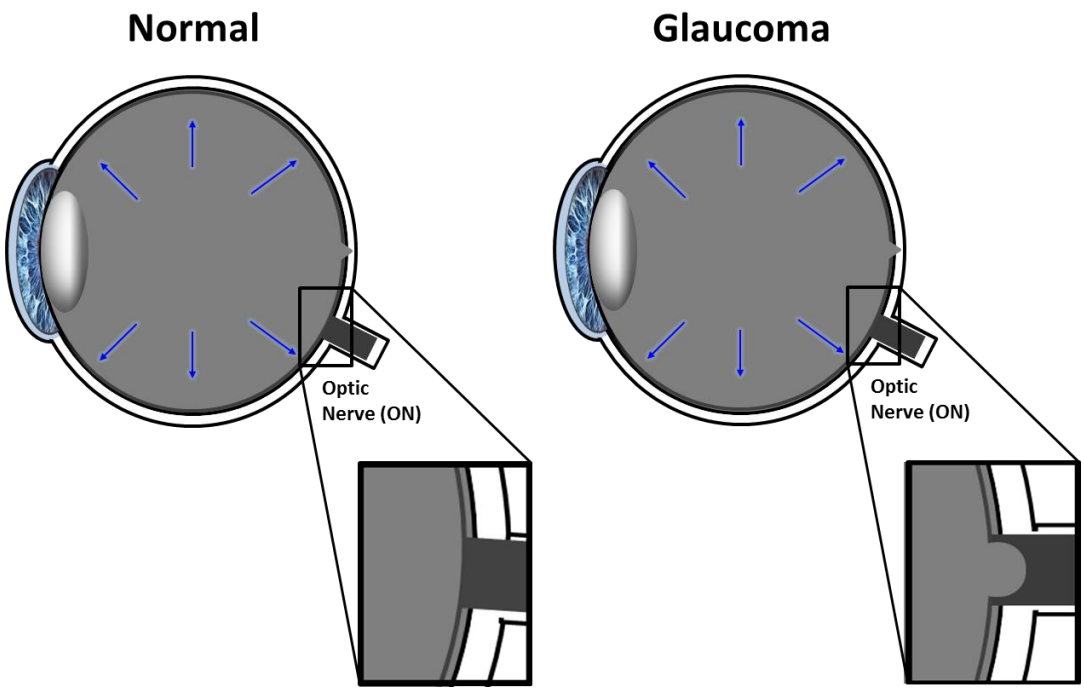

Figure 2.11 Increased intraocular pressures inside the eye cause damage to the optic nerve. Adapted from Howell et al. (2007).

An increased intraocular pressure (IOP) was initially believed to damage RGC axons (Fechtner and Weinreb, 1994). In angle-closure glaucoma, the narrow-angle between the cornea and iris physically blocks the trabecular meshwork responsible for draining the aqueous humour outside the eye. In open-angle glaucoma, the aqueous humour is not drained fast enough by the trabecular meshwork. However, glaucoma also appears in patients with normal IOP (Bengtsson, 1981, Tielsch et al., 1991). Thus, a vascular theory also suggests that an impaired blood supply at the ONH is responsible for axonal damage (Fechtner and Weinreb, 1994). The ONH has been considered as a 'biomechanical structure' as pathological levels of stress and strain could develop in the LC at any level of IOP (Downs et al., 2005). The previous study showed that the mechanical properties of sclera significantly influence the deformation of the more compliant LC that might highly contribute to the development of glaucoma (Coudrillier et al., 2015b, Oglesby et al., 2016, Eilaghi et al., 2010). For the treatment of high-pressure glaucoma, medication such as eye drops can effectively reduce the amount of aqueous humour produced by the eye. Laser therapy or surgery can also prevent the build-up of aqueous humour inside the anterior chamber (Quigley, 1993). However, these treatments are not efficient in glaucoma with normal IOP.

Biomechanical studies of glaucoma have focused on microstructural changes in the peripapillary region. Scleral thinning occurs in the peripapillary sclera of experimental glaucoma monkey eyes (Downs et al., 2001) but this thinning was not observed in human eyes (Jonas and Jonas, 2011). The thickness of sclera followed with a higher fixation in sclerae with glaucoma suggests a loss of non-fibrillar components in glaucoma (Cone-Kimball et al., 2013). The density of collagen is

lower in human and experimental glaucoma monkey eyes (Quigley et al., 1991). However, no significant change has been found in the collagen fibril diameter change or elastin density. The peripapillary sclera of human glaucomatous eyes exhibits a lower creep rate and higher stiffness than normal eyes measured by inflation testing (Coudrillier et al., 2012). Moreover, inflation tests in experimental glaucomatous monkey eyes under inflation show a higher stiffness in the posterior sclera (Girard et al., 2011). The peripapillary sclera exhibits higher viscoelastic parameters compared to the equilibrium modulus after stress relaxation, but there is no change in time-dependent viscoelastic parameters as compared to controls with uniaxial strip tests (Downs et al., 2005).

2.2.3 The sclera and myopia

Myopia is the most common visual disorder in which light enters the eye and focuses in front of the retina. It is most often associated with an increase of the axial length of the eye. Most patients develop myopia during their childhood and keep progressing until puberty (Lagrèze and Schaeffel, 2017). Among people affected by myopia, 12-15 % patients suffered from high myopia (McBrien et al., 2003, Celorio and Pruett, 1991), which can eventually lead to blindness due to the increased risk for retinal tissue degeneration (Celorio and Pruett, 1991). The regional and worldwide prevalence of myopia in the future has been predicted by a meta-analysis conducted in 2016. In 2010, the highest incidence was reported in East Asia, Southeast Asia, and North America. However, the highest increase rate has been estimated in Asia-Pacific, South Asia, and the Caribbean (Lagrèze and Schaeffel, 2017).

The overall thinning and localised ectasia of the sclera has been reported in highly myopic eyes (Kaya and Yildirim, 2016). This thinning is associated with the thinning of scleral collagen fibrils and reductions in proteoglycan content. An increase in the frequency of abnormal small and irregular shape collagen fibrils have been found in the long-term myopic sclera (Figure 2.12), especially the outer sclera (Curtin et al., 1979). This change of scleral collagen fibril seems to cause the lower tensile strength of tissue that makes the sclera easier to expand. Reductions in the proteoglycan content of myopic sclera have also been found in several studies in humans, chickens, and tree shrews (Rada et al., 1994, Norton and Rada, 1995, Avetisov et al., 1983b). An axial elongation of the eye, especially the posterior pole (Rada et al., 2006), occurs in the myopic eye, illustrating the mechanical properties of the posterior sclera.

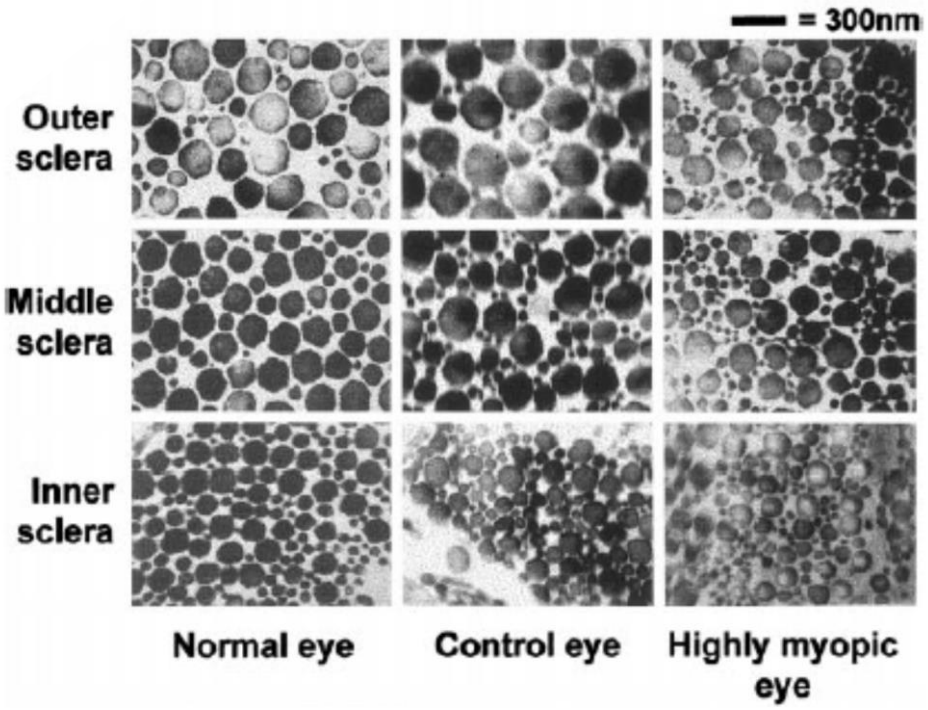

Figure 2.12 Transverse section of scleral collagen fibrils in normal, age-matched control, and highly myopic eyes, captured by scanning electron micrographs (SEM) (McBrien et al., 2001). Compared to the normal and control eye, an increase of

abnormal small and irregular shape collagen fibrils have been found in the highly myopic sclera.

In myopic eyes, most changes occur in the posterior region of the sclera. The thickness of the sclera decreases along with a decrease in tissue dry weight (McBrien et al., 2001a). This decrease in both suggests a loss (rather than a redistribution) of tissue. The mechanical measurement for the myopic eye also focuses on the posterior sclera. The posterior sclera of myopic human eyes under uniaxial testing reaches a higher strain at maximum pressure than that of normal eyes (Avetisov et al., 1983b). In the myopic eyes of tree shrews, the posterior sclera also shows a greater strain at the peak pressure (Phillips and McBrien, 1995; Phillips et al., 2000), as well as a higher creep rate; the stiffness remains the same as in uniaxial strip tests.

2.2.4 Animal models for vision science

Animal models are often used for vision science research (for the study of the retina, glaucoma, myopia and so on.) as an insight into tissue mechanisms, structure, nanostructures, and biochemistry. The animal models used most often include monkeys (Girard et al., 2011), pigs (Murienne et al., 2015), chicks, tree shrews (Sherman et al., 1977; Wallman et al., 1978; Wiesel and Raviola, 1977), guinea pigs, and mice (Barathi et al., 2008; Howlett and McFadden, 2006). From all these animals, monkeys are the most suitable large mammal for research into glaucoma and myopia (Downs et al., 2005; Funata and Tokoro, 1990). However, the availability of monkeys is very low due to ethical and economic reasons. Pigs have been suggested as another suitable model by many studies. Porcine scleras show similarities in structure, histology, and collagen fibril diameter (Nicoli et al., 2009) and architecture

(Nicoli et al., 2009). Despite the differences in tissue thickness, porcine and human scleras behave the same way towards the permeation of a small molecule. Human and porcine scleras also show similar responses towards chemical and physical cross-linking, as well as increased stress value compared to porcine sclerae; a similar response is not observed in rabbit sclerae (Zhang et al., 2014). Additionally, the porcine eye has been reported as a suitable animal model for studying glaucoma (Ruiz-Ederra et al., 2005).

2.3 3D-Imaging measurement of scleral ultrastructure

2.3.1 Scanning Electron Microscope (SEM) and Tunneling Electron Microscope (TEM)

2.3.1.1 Principles

Both SEM and TEM are type of electron microscopes (EM) that use electrons to illuminate a specimen and create an enlarged image. Electron microscopes have much greater resolving power than light microscopes and can obtain much higher magnifications. Some electron microscopes can magnify specimens up to 2 million times, while the best light microscopes are limited to magnifications of 2000 times. (Williams and Carter, 1996)

In SEM, a beam of electrons is directed from a filament to the sample in a vacuum environment. The electrons are guided to the sample by a series of electromagnetic lenses. The solution and depth of field of the image are determined by the beam current and the final spot size, which are adjusted with one or more condenser lenses and the final, probe-forming objective lenses. The electrons interact with the sample within a few nanometers to several microns of the surface, depending on beam

parameters and sample type. Electrons are emitted from the sample primarily as either backscattered electrons or secondary electrons. Once these electrons escape from the sample surface, they are typically detected by an Everhart-Thornley scintillator-photomultiplier detector (Khursheed, 2007).

The beam of electrons went "pass through" the specimen to form an image in TEM instead of focus only on the surface. When the electrons beam emerges from the specimen, it also carries structure information of the specimen then these information magnified by the objective lens system of the microscope. (Williams and Carter, 1996)

2.3.1.2 Application to the Sclera

Special tissue preparation methods are needed for testing on collagen-based biology tissue using both SEM and TEM. Samples need to be fixed and dehydrated before imaging. A transection image of collagen fibrils is particularly used for analysing collagen fibril diameter and distribution (Wollensak et al., 2004, Massoudi et al., 2015, Boote et al., 2009). Some sections with a slightly ellipsoidal section profile (Figure 2.13) result in oblique sectioning. The minimal transverse diameter of the collagen fibrils was thus measured because, in ellipsoidal section profiles, the shortest diameter is equal to the diameter of the corresponding circular section profile (Wollensak et al., 2004). However, this method is not suitable for tissues like the sclera where collagen fibrils form in bundles and greatly vary in diameter and orientation.

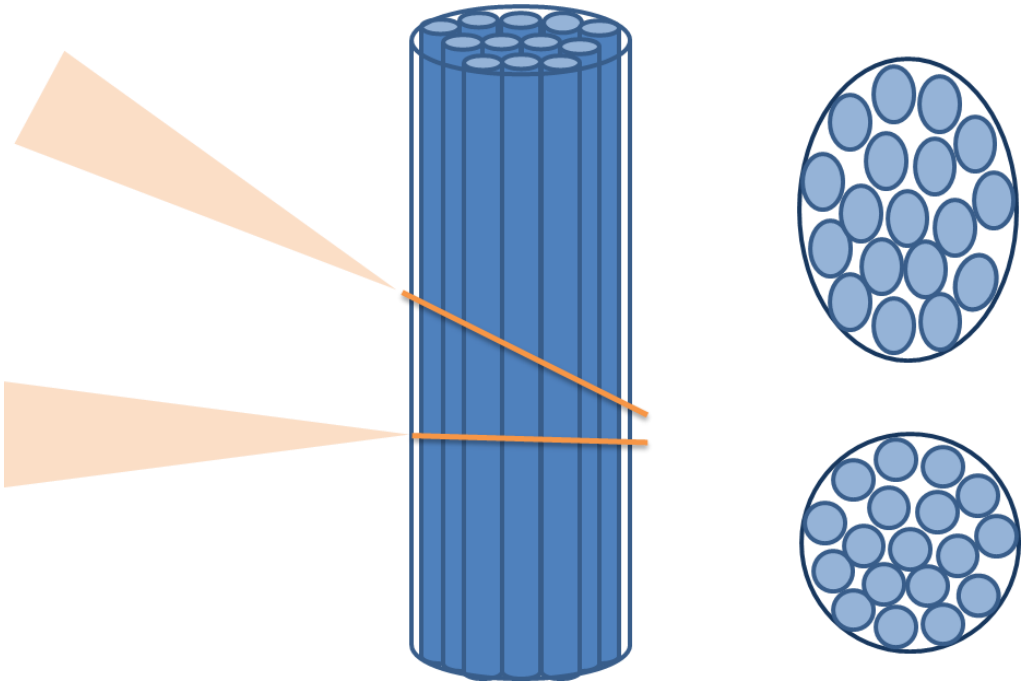

Figure 2.13 With SEM, rectangular sections with circular section profiles (B). Oblique sections with ellipsoidal section profiles (C). The minimum profile diameter is identical in both section profiles (A).Adapted from Wollensak et al. (2004).

Sclera tissue were observed using SEM/TEM by many studies, mainly focus on the micro-level to determine collagen fibrils distribution (Nicoli et al., 2009) and observes the scleral matrix (Wolff, 1997). While some of the studies has observed the in nano-scale for the nanostructure of the collagen fibrils (Young, 1985b, Austin et al., 2002). However, few of them has developed a method for calculating the collagen fibrils parameters like D-period and diameter. As figure 2.14(a) Transmission electron micrograph of two rabbit scleral collagen fibrils. The characteristic D-period of the collagen fibril is clearly visible. The black filaments bridging between two adjacent fibrils are proteoglycans.(Young 1985), (b) Transmission electron micrograph showing a transverse section of collagen lamellae in the outer, mid, and inner sclera of the normal tree shrew.(McBrien, Cornell et al. 2001), (c) Electron micrograph image of the human sclera showing six superimposed lamellae. Within each lamella, collagen fibrils run in the same direction. Significant collagen fibrils orientation variations are observed between adjacent lamellae, and fibroblasts occupy the interlamellar space. (Wolff 1997), (d) Scanning electron

micrograph of the collagen bundles in the sclera of the human eye and porcine sclera. Porcine scleral collagen bundles looked thicker but still showed a similar arrangement.(Nicoli, Ferrari et al. 2009)

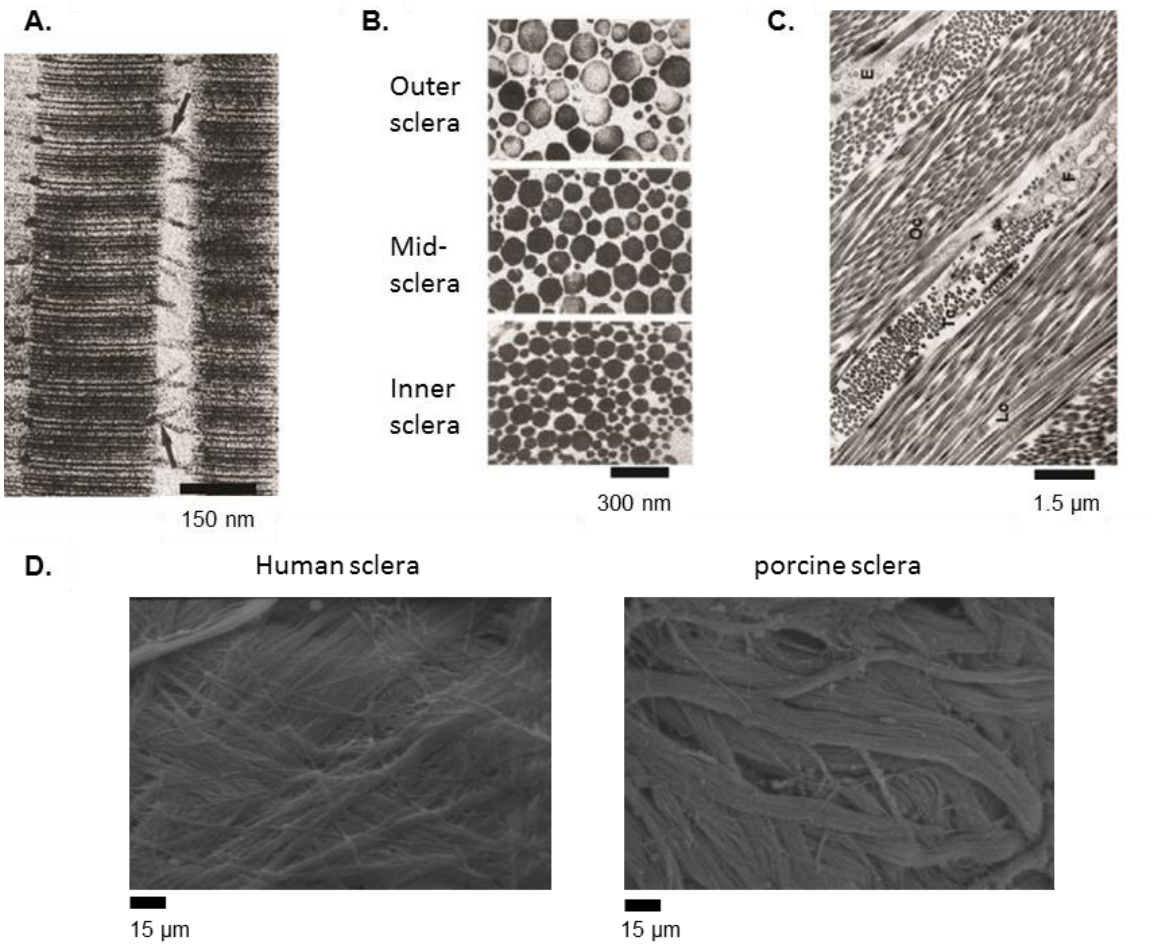

Figure 2.14 SEM/TEM Imaging of the sclera structure at multiple length-scales.

2.3.2 Atomic force microscopy

2.3.2.1 Principles

The first atomic force microscope was developed by Binning et al (1986) to overcome the limitations of the conductivity requirement for scanning tunnelling microscopy (STM). It is a nanometre-scale scanning probing technique, capable of

sensing the smallest variations on the surface of a material. In an AFM (as shown in Figure 2.15), force is required to maintain contact between the probe and sample constantly or for a short time (contact mode and tapping mode) while raster scanning. During the scanning process, a laser beam lands on the reflection surface of the probe and the reflection beam is received by a position-sensitive photodetector through a mirror. The photodetector detects the deflection of the cantilever caused by the sample surface, so the measurement of AFM is made in three dimensions, with a horizontal (X-Y) plane and a vertical (Z) dimension (Meyer 1992). AFM can be performed on fresh biological tissue samples; there is no need for sample fixation and any treatment for testing with this method. (Sweers et al., 2011)

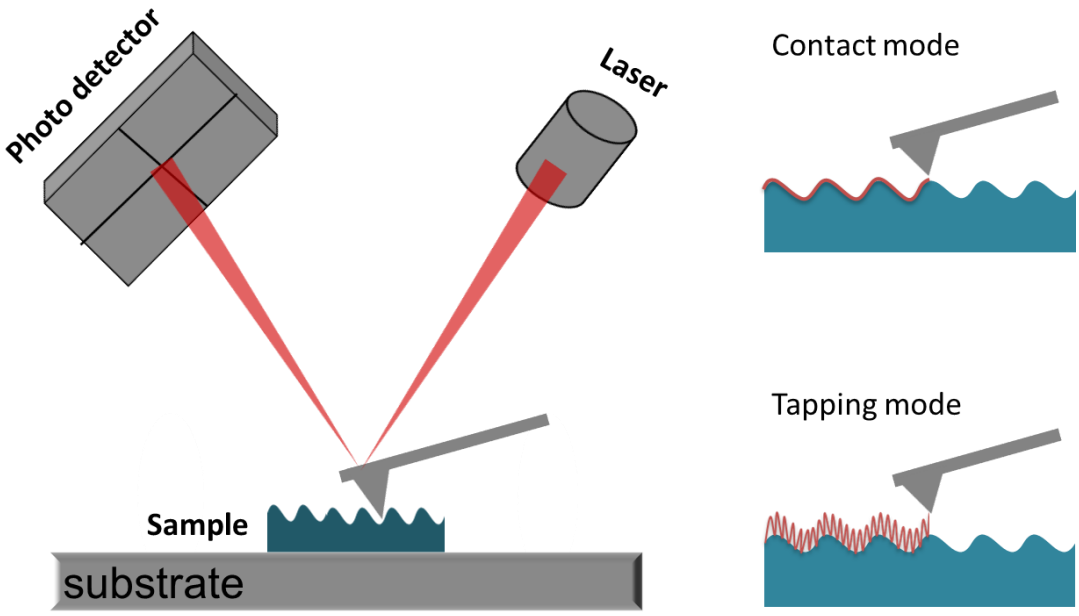

Figure 2.15 In an AFM, a laser beam landed on and reflected by the surface of cantilever then caught by photodetector. Surface roughness of the sample could then be captured as movement of cantilever. In the contact mode, tip and sample are kept in contact during the raster-scan. Detector signal is a measure of cantilever deflection, the feedback system adjusts the height of the cantilever base to keep the deflection

constant as the tip moves over the surface. In the tapping mode, probe is mechanically oscillate at or near its resonance frequency and makes repulsive contact with the sample surface at the lowest point of the oscillation. Detector signal is cantilever oscillation amplitude or phase.

The two most frequently used methods are contact mode AFM and tapping mode AFM (Rugar et al. 1990) (as shown in Figure 2.15), which can be carried out in a number of environments (Hansma et al., 1994, Bramowicz et al., 2012, Fukuma et al., 2005). In the contact mode, the small (angular) movement of the lever is commonly measured by a laser beam that is reflected off the cantilever and directed onto a split photodetector while the probe is in constant contact with the sample. The tapping mode is much gentler than the regular contact mode. In the tapping mode, the tip only contacts the surface for a small percentage of the time, keeping the tapping force low and the lateral forces negligible.

Significant differences between AFM and SEM arise when creating a representation of a sample surface. On atomically smooth surfaces, AFM is capable of producing a three-dimensional topography using just a single scan. AFM also provides a greater level of detail for these surfaces, as SEM is not as efficient in resolving the subtle changes on a highly smooth surface. When scanning thin films, SEM and AFM can produce very similar results. However, with images generated by SEM, it can sometimes be difficult to determine the slope of a surface. Conversely, AFM provides height information, making it easy to determine if surface features on a thin film are rising or falling (Russell et al., 2001). When scanning relatively rough surfaces, SEM's large depth of field gives it a significant advantage over AFM. If a sample has details that are millimetres high, the penetration of the electron beam used in SEM makes it possible to images those details.

2.3.2.2 Application to the Sclera

With AFM, collagen fibril surface information like D-banding gap depth can be extracted from height and deflection channel images, example method shown in Figure 2.16. Scleral collagen fibril structure including diameter, D-periodicity and gap zone depth were analysed by several studies using both AFM and EMs (Spitznas et al., 1970, Spitznas and Hogan, 1970, Komai and Ushik, 1991, Komai and Ushikif, 2015, Fullwood et al., 1995, Meller et al., 1997, Yamamoto et al., 2002, Grant et al., 2011b, Choi et al., 2011, Jan et al., 2017, Papi et al., 2014) . However, there are significant variations between the results of these studies. The variation may be caused by difference animal, sample condition and scanning locations. Also there might be error caused by manual measurement.

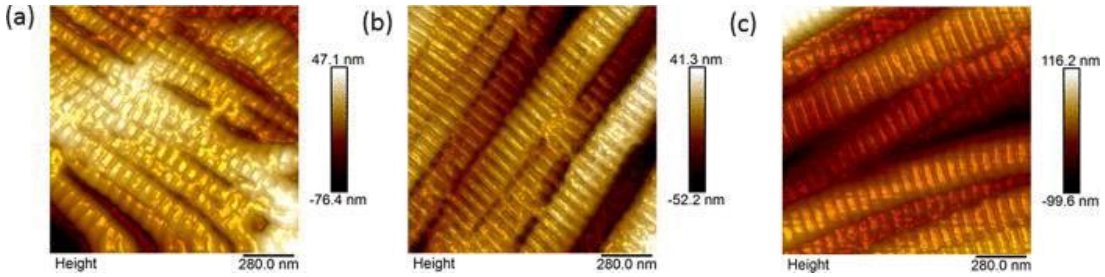

Figure 2.16 AFM images from height channel showing scleral diameter distribution across the sclera (a), posterior (b) equatorial and (c) anterior regions (Papi et al., 2014). From the images, collagen fibrils diameter were found to be significantly greater in the anterior region than in posterior region.

2.4 Mechanical testing of the sclera

The anterior part of eye forms the cornea, and the posterior part consists of three layers: the sclera, choroid and retina (Clark et al., 2011). Among these three tissues,

the sclera is the toughest, and the retina is the softest (Campbell et al., 2014).Thus the contribution to the eye tissue stiffness from the retina, choroid and sclera are an order of magnitude higher than its each other. Moreover the sclera is reported to be two times stiffer than the cornea (Pierscionek et al., 2007). Thus, the sclera plays a crucial role in maintaining the mechanical properties of the eye.

The sclera is nearly incompressible (Battaglioli and Kamm, 1984). The mechanical properties of the sclera are dependent on temperature (Greene and McMahon, 1979) and hydration (Curtin, 1969). The posterior sclera is more compliant than the anterior sclera (Palko et al., 2011), despite its thickness and higher collagen content than other regions (Avetisov et al., 1983a). The peripapillary sclera deforms more than the rest of the posterior sclera (Fazio et al., 2012). The mechanical properties of the sclera have been investigated using different experimental techniques. These have included uniaxial and biaxial testing (Zhang et al., 2014), inflation of the globe and scleral shells (Murienne et al., 2016, Murienne et al., 2015, Coudrillier et al., 2015b), dynamic mechanical testing (Palko et al., 2011), nanoindentation (Nayar et al., 2011), and indentation with AFM (Papi et al., 2014, Spitzner et al., 2015). Different testing methods affect the results by several orders of magnitude.

2.4.1 Uniaxial tensile testing

2.4.1.1 Principles

Uniaxial testing involves subjecting a material strip of uniform width to a one-dimensional tensile force. The ensuing load-elongation measurements are then used in conjunction with the strip dimensions to calculate the stress-strain behaviour and hence the resulting stiffness of the material. The uniaxial testing method is the most

common experimental technique used to determine the properties of engineering materials (Elsheikh and Anderson, 2005) due to its relatively simple set-up and post-test mathematical analysis. However, there are some inherent deficiencies when used on biological tissues, particularly specimens which are obtained from the ocular globe (Elsheikh et al., 2008). Hydration of the biological tissue has been shown to have a significant effect on the biomechanical properties (Haut and Haut, 1997). Hence, the environment in which the specimen is tested has been essential for mechanical testing. For specimens used for tensile testing, several methods such as humid and liquid chambers have been developed to keep the tissue at an appropriate hydration level(Hatami-Marbini and Rahimi, 2014).

2.4.1.2 Application to the Sclera

Geraghty et al (2010) studied regional variation biomechanical properties for the anterior, equatorial and posterior region of human sclera and also the age-related variation in the mechanical properties in the sclera (Geraghty et al., 2012), both with uniaxial tensile testing. In both studies, a hydration chamber was designed to keep the sclera tissue hydrated (as shown in Figure 2.17).

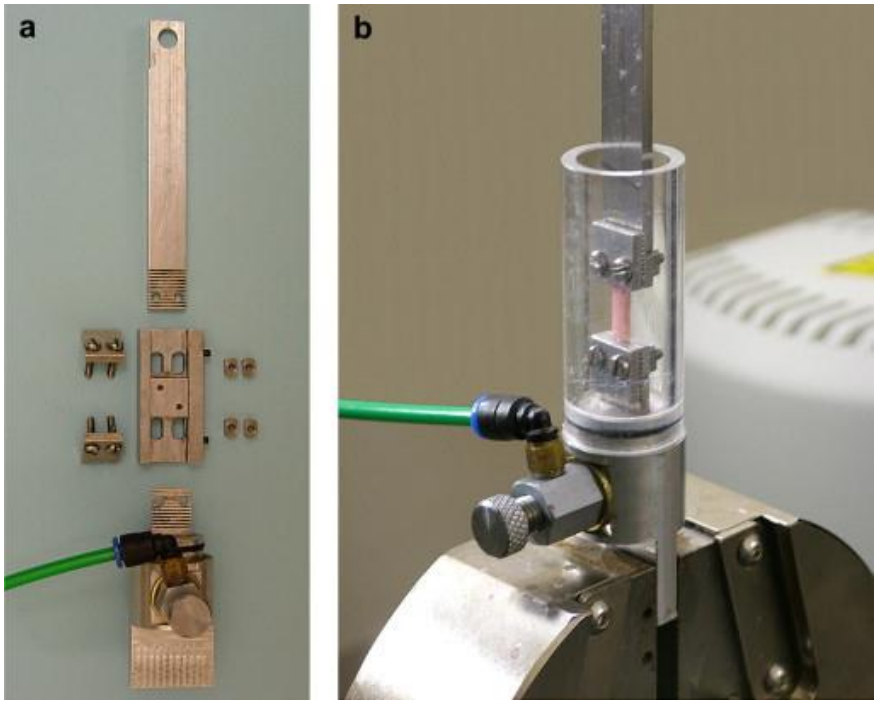

Figure 2.17 Uniaxial tensile testing set up (a) and the liquid chamber (b). Scleral strip is immersed in a tissue bath yields estimates of the scleral modulus. (Geraghty et al., 2015)

Uniaxial testing is a straightforward method. However, it has several limitations when testing on eye tissues, such as stress concentration and preconditioning effects. Preconditioning is characterised by the progressive shift of the load-unload curve on the first few cycles. This phenomenon is partly due to the rearrangement of the collagen fibrils in the direction of stress (Curtin, 1969) and suggests that the tissue is not tested under physiological conditions. Preconditioning loading cycles are designed to obtain a unique and recoverable reference state of the scleral tissue and load-unload curve (Weiyi et al., 2008, Lari et al., 2012). Moreover, the severed collagen fibrils at the tissue cutting edges and the act of flattening the sclera when testing can introduce significant errors in the measured mechanical properties (Campbell et al., 2014).

2.4.2 Inflation testing

2.4.2.1 Principles

Unlike tensile testing, inflation testing mimics the *in vivo* loading conditions of the eye. It allows the measurement of the pressure-induced 3D displacements of the scleral surface using image tracking techniques such as 3D digital image correlation (Murienne et al., 2016), electronic speckle pattern interferometry (Fazio et al., 2012), or optical flow tracking of surface particles (Girard et al., 2008).

2.4.2.2 Application to the Sclera

Three-dimensional displacements within the scleral volume can also be measured using ultrasound speckle tracking (Perez et al., 2014). For the inflation of scleral shells, boundary effects such as stress concentration are assumed to be negligible away from the clamp. In addition, tissue preconditioning was shown to be unnecessary due to the fully fixed boundary condition, providing the tissue was allowed time to recover and did not incur irreversible damage.

2.4.3 Nanoindentation

2.4.3.1 Principles

The term ‘nanoindentation’ refers to a variety of indentation-based mechanical tests applied to small volumes of material. A ‘nanoindenter’ is the name given to commercially available laboratory equipment capable of determining these nano-to-micron scale mechanical properties. During nanoindentation, a load is applied to move the tip into the sample (Shown in Figure 2.17). Load and displacement are monitored continuously during the indentation process, resulting in a load-displacement curve. The mechanical properties of a sample is calculated directly based on recorded indentation load and displacement data. The ‘nano’ prefix can potentially be misleading as the scale of the tip that is selected can vary in size, with the tip radius ranging from approximately 40 nm to 100 μm or more. The tip can be custom-made using bearings in the millimetre scale (Lee et al., 2008). It has a wide working force range of 1 μN to 500 mN, and a displacement range of 1 nm to 20 μm. This range fills the gap between AFM and macroscale mechanical testing (Ebenstein et al., 2006).

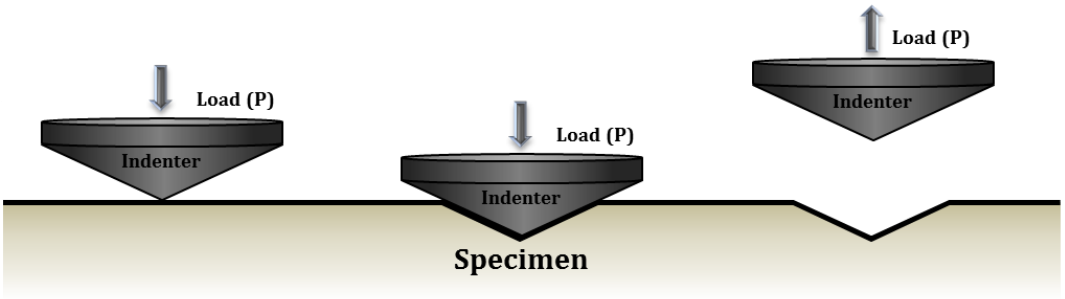

Figure 2.17 Schematic of load-control nanoindentation: a load (P) is applied while the load-displacement and displacement-time are recorded.

Doerner and Nix (Doerner et al., 1986) published the first comprehensive experimental and analytical approach to a generalised form of nanoindentation analysis from load-displacement data for non-rigid indenters of all geometries. Oliver and Pharr further generalised their approach, resulting in the widely used method for indentation analysis (Oliver and Pharr, 2004). In the Oliver-Pharr method, the projected contact area between indenter tip and material is estimated using the equations for the elastic contact of an indenter of arbitrary shape on a uniform and isotropic half space. The indentation modulus and hardness of the material can thus be calculated without the necessity of imaging the indentation after the experiment. The Oliver-Pharr method was not initially developed for analysing indentations for thin biology tissue on substrates, and no information about a possible substrate is included in the analysis. However, it is frequently used by researchers to interpret indentations performed on thin films in an attempt to obtain approximate film properties regardless of the effect of substrate properties on the measurement. The accuracy of such a measurement depends on the film and substrate properties and on the indentation depth as a fraction of the total film thickness. In general, the error due to the substrate affects increases with increasing indentation depth and with increasing elastic mismatch between film and substrate (Doerner et al., 1986, Burnett and Rickerby, 1987, Pharr and Oliver, 1992, Saha and Nix, 2002) .

Dynamic indentation analysis (DMA) techniques (Hayes et al., 2004) was developed to control the loading parameters throughout indentation experiments continuously. Typically, an oscillatory stress is imposed on the sample, either as tension, compression, or torsion. The resulting strain, which is also oscillatory, is measured. The outcome of a DMA test is the storage modulus, G´, which characterises the

sample's ability to store energy elastically, and the loss modulus, G″, which characterises the sample's ability to dissipate energy as heat. Taken together, G´ and G″ are the complex modulus of the material. Phasor analysis of DMA mechanics reveals that the storage and loss modulus are concisely related through the loss factor, which is the tangent of the phase angle, δ, by which the strain lags the stress (Akhtar et al., 2018).

In practice, G´, G″, and tan δ are measured by DMA as a function of frequency and temperature. Reporting any two of these parameters is sufficient for knowing all three. When the sample is in the form of a thin form, analogous measurements can be made by means of an oscillatory indentation test. As the indenter is pressed into the sample, an oscillating force is imposed on the sample through the indenter, and the resulting displacement oscillation is measured. By presuming the same kind of constitutive form which DMA employs, and by interpreting the indentation data in light of established contact models, one can measure equivalent values of G´ and G″ by oscillatory indentation.

Oscillatory indentation has additional advantages over traditional DMA, even when the material is available in quantities large enough to be tested by the traditional method. The moving mass of an indenter is much smaller than the moving mass of a traditional DMA instrument, which means that the indenter can be made to oscillate at much higher frequencies. Thus, oscillatory indentation can be used to characterise a larger frequency range (Han et al., 2011).

Oscillatory indentation has been established as a suitable method for mechanical testing for soft materials. Peters et al (2017) monitored the freeze-thaw cycles on

canine cartilage by using oscillatory nanoindentation with a flat punch indenter tip. Akhtar et. al (2018) utilised this method for testing mechanical properties for hydrogels.

By utilising a flat punch indenter linear viscoelastic analysis can be utilised. The theory is described in detail elsewhere(Akhtar et al., 2018). A summary is provided here. Shear modulus is calculated using the following equation:

$$G' = \frac{S(1-v)}{4a} \tag{2.1}$$

where G´ is the shear storage modulus of the material, v is the Poisson's ratio, S is the elastic stiffness of the contact, and a is the radius of contact area.

And for G″ the loss modulus:

$$G'' = \frac{D_s\omega(1-v)}{4a} \tag{2.2}$$

where the $D_s\omega$ is the contact damping, manifest as the damping coefficient Ds multiplied by the radial frequency ω.

The loss factor, tan δ, is defined as the loss modulus divided by the storage modulus is

$$\tan\delta \equiv \frac{G''}{G'} = \frac{D_s\omega}{S} \tag{2.3}$$

The selection indenter probe geometry is crucial for nanoindentation, as it determines the modes of deformation. As mentioned earlier, for the oscillatory

nanoindentation method used in this thesis, a flat punch indenter is utilised. The indenter tips are typically made out of very stiff materials, such as diamond or sapphire, so that the compliance of the sample will be greater than that of the tip. For nanoindentation of metals and ceramics, three-sided pyramidal tips that come to a sharp point, such as the Berkovich tip (Figure 2.18A), are commonly used (Pharr, Bolshakov 2002, Oliver, Pharr 2004). However, for indenting soft polymers and soft tissues, a spherical tip (Figure 2.18B,C) (Field, Swain 1993) is commonly used to minimise plastic deformation and stress concentrations to avoid damaging the sample. A third option also used in the study of viscoelastic materials is the cylindrical flat punch (Figure 2.18D). A flat tip (Herbert et al. 2009) has the advantage of a constant, known contact area as a function of depth, but has high-stress concentration at the contact perimeter.

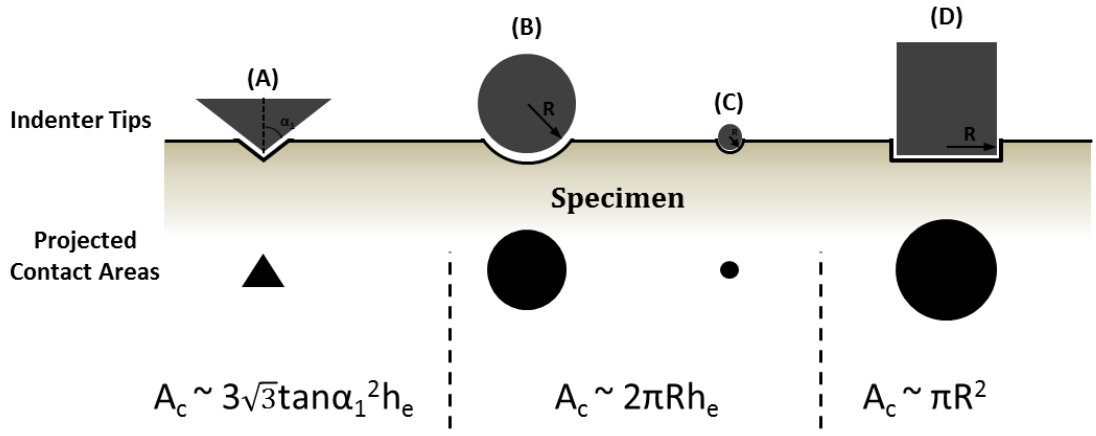

Figure 2.18 Schematic of Berkovich (A), big (B) and small (C) sphere, flat punch (D) indenter tips, and their projected areas Ac. he is the contact depth, α1 is a geometric constant, and R the radius. The geometry shown in (D) is relevant to this thesis.

2.4.3.2 Application to the Sclera

Nanoindentation technique has been used for sclera mechanical properties measurement by previous studies (Battaglioli and Kamm, 1984, Nayar et al., 2011, Siegwart Jr and Norton, 1999, Nayar et al., 2012). However, as showed in the table 2.2, the results mechanical properties of the sclera tissues vary several orders of magnitude which from as low as 30kPa to 400kPa, this variation may cause by difference in mechanical characterization protocol. The latest revealed storage modulus by Nayar et al. (2012) in macroscale is 405 ± 205kPa. Nanoindentation is a surface probing technique with monitored indentation depth, however there is difficulty of surface detection for sample submerged in liquid. Collagen based tissue like sclera, the tissue properties are easily affected by hydration level. Hence, a suitable hydration method is need for nanoindentation testing. Also, for measuring G' and G'' are the linear viscoelastic properties, strain-stress behaviour cannot be captured by this technique.

2.4.4 Atomic force microscopy for Mechanical Testing

2.4.4.1 Principles

Atomic-force microscope (AFM) is another technique to measure sample mechanical properties in nano- and microscale, AFM and nanoindenters both work by probing a surface. Additionally, AFM could also provide a high-resolution image by mapping sample surface.

The cantilever and tip are typically manufactured from silicon. Common dimensions are about 100 μm for the length of the cantilever, a few nanometres to tens of nanometers for the tip radius, and 10mN/m to 100N/m for spring constants (Russell et al., 2001). The tip itself can have various coatings to enable its sensitivity to measure certain interactions – these coatings can include metal for conductivity, or a ligand for biological specificity. The ramping force is recorded and interactions between the tip and the sample surface is measured by monitoring the displacement of the cantilever. The external disturbance is the tip-sample interaction as measured through the cantilever displacement sensor. The mechanical properties of the sample like force curve can then be calculated with the above parameters.

There are various models that used to fit force-displacement curves for Young's modulus calculation.

In the **Hertz model**, two critical assumptions need to be considered: (a) the indenter tip must has radius that is much bigger than the indentation depth; (b) the indented sample is much thicker in comparison to the indentation depth (Mahaffy et al., 2000).

$$F = \frac{4}{3}\frac{E}{(1 - \nu^2)}\sqrt{R\delta^{3/2}} \qquad (2.4)$$

where E, ν, R and δ refer to the Young's modulus, Poisson's ratio, tip radius, and indentation depth, respectively (Adamcik and Mezzenga, 2012).

The **Sneddon model** (Sneddon, 1965)was developed for measuring on very soft samples including. cells, tissues, biomolecules. When the sharp tips with a small tip radius or soft samples are involved, it is more appropriate to use the Sneddon model which considers the tip as an infinite conical indenter and describes the

corresponding elastic deformation of the initially flat surface without limitation on contact radius/tip radius (Calzado-Martín et al., 2016).

$$F = \frac{2}{\pi}\frac{E}{(1-v^2)}tan(\alpha)\delta^{\,2} \tag{2.5}$$

where F is the force, E is the apparent Young's modulus, v is the Poisson's ratio of the sample, α is the half angle of the AFM tip and δ is the indentation depth.

The **DMT model** (Derjaguin et al., 1975) modified from Herts model by adding the adhesive forces between the tip and the surface:

$$F - F_{adh} = \frac{4}{3}E * \sqrt{R(d-d_0)^3} \tag{2.6}$$

where $F{-}F_{adh}$ is force on the cantilever relative to the adhesion force, R is the tip end radius which can be calibrated prior to measurement, and $d{-}d_0$ is the deformation of the sample. If the Poisson's ratio is known, the equation can then change to

$$E^* = \left[\frac{1-v_s^2}{E_s} + \frac{1-v_{tip}^2}{E_{tip}}\right]^{-1} \tag{2.7}$$

The tip modulus (E_{tip}) is assumed to be infinite when we calculate Young's modulus of the sample (E_s). The Poisson's ratio ranges from 0.2 to 0.5, giving a variation in the reduced modulus of the sample between 4% and 25%; however, this ratio is mostly not accurately known (Pittenger et al., 2010). . In PeakForce Quantitative Mechanical property Mapping (QNM), elastic modulus (Young's modulus) is typically calculated by using the DMT model (Derjaguin *et al*., 1975)

PeakForce QNM mode (Pittenger et al., 2010a) is an AFM mode the truly achieved quantitative material property mapping with resolution demanded by researchers. This mode is developed base on the tapping mode, however the PeakForce QNM mode The tip only contacts the surface for a small percentage of the time, keeping the tapping force low and the lateral forces negligible. (in traditional mode, the lateral force mode that the tip exerts on the sample can cause the sample to tear or the tip to fracture) The force volume imaging for the mode collects force curves at each pixel in an image and directly link the sample morphology with local mechanical behaviour in the whole scan area. PeakForce QNM mode is ideal for testing on soft tissue (Young et al., 2011, Sweers et al., 2011) because unlike in tapping mode the cantilever vibrates in a constant amplitude much slower than the cantilever resonant frequency (i.e. non-resonant mode), thus avoids the filtering effect and dynamics of a resonating system. Because PeakForce Tapping does not resonate the cantilever, cantilever tuning is not required, which is particularly advantageous in fluids. Moreover, there is a controlled the maximum force (PeakForce) applied on the tip is controlled in this mode. This controlled force protects the tip and sample from damage by minimizing the tip-sample contact area.

2.4.4.2 Application to the Sclera

Scleral tissue from all regions was studied by Papi et al. (2014) using PeakForce QNM mode. In this study, variations in the collagen fibril diameter, adhesion, elastic modulus and dissipation all scleral regions were tested in air. In the results, the mean collagen fibril diameter, elastic modulus and dissipation increased from the posterior to the anterior region.

Grant et al. (2011a) have studied the porcine scleral mechanical properties and corresponding tissue ultrastructure by using tapping mode in fluid and heated to 37^{o}C to mimic the human body environment. The mechanical properties results from this study are significantly smaller than Papi et al's results (values shows in Table 2.2). This difference shows that scleral mechanical properties are greatly influenced by testing environment, AFM mode and testing location.

Table 2.2 Values reported in the literature for the stiffness of sclera, and methodologies used to obtain these values.

Author	**Tissue**	**Technique**	**Elastic modulus (MPa)**
Woo, Kobayashi et al. 1972	Human sclera	Pressurization of the eye globe	2.3
Friberg and Lace 1988	Human sclera	Uniaxial testing	2.9±1.4
Battaglioli and Kamm 1984	Human sclera	Unconfined compression	2.7 ± 4.1×10-2
Siegwart 1999	Tree shrew sclera	Tensile	1.28 ± 0.43
Wollensak and Spoerl 2004	porcine sclera	Tensile	22.82 (at 8% strain)
Grant et al. 2011	Porcine sclera	AFM	0.41 ± 0.28
Chen 2009	Porcine sclera	Tensile	0.07 ± 0.12
Nayar et al. 2012	Porcine sclera	Nanoindentation	0.40– 0.20 (macro) 0.05 – 0.04(nano)
Papi et al. 2014	Porcine sclera	AFM	6.94±1.96

2.5 Summary

The mechanical properties and nanostructure of the sclera have been shown to play an important role in the initiation and development of glaucoma and myopia. Alterations to the tissue mechanical properties nanostructure could significantly influence one's possibility of developing these diseases even at the normal IOP. In addition, proteoglycan content changes have been observed in pathological and aged scleras, but the impact of proteoglycan variations in the mechanics and structure of those proteoglycan reduced scleras has not been determined.

Moreover, there are various types of PGs existed in the sclera and they are formed in different structures. This indicated they might have a different contribution in tissue structure and mechanical behaviour. However, no study so far had considered this possibility when study the structure or mechanical properties of proteoglycan depleted scleras.

Finally, the amylase has been found in human tear fluid since 1975 and been proved to have effect on PGs in connective tissues by Quintarelli et al since 1969. Also, an increased level of amylase has been found in patients with keratoconus. However, there is no study for the role of amylase played in the eye has been conducted in neither biochemistry nor biomechanical field so far.

Base on the outcome and gap from previous research, this study will further investigate the nanostructure and mechanical response of sclera and the contribution of PGs to all regions of scleral structure and mechanical properties by using both AFM and nanoindentation technique. Additionally, this study will also investigate the amylase effect on the sclera by study the scleral proteoglycan content,

nanostructure and mechanical behaviour before and after treatment with α-amylase to provide a straightforward link for future researchers to study the role of amylase plays in the ocular tissue.

Chapter 3

3.1 Introduction

3.1.1 Proteoglycan in connective tissue

Connective tissue, wherever it is found, consists of collagen and interfibrillar matrix, made up mainly of proteoglycan (PGs) and glycoproteins (Scott, 1988). These are both products of fibroblasts. The amount and type of PGs vary from tissue to tissue. PGs play important roles in tissues, including water banding and tissue hydration, regulation of fibril size during fibrillogenesis, structural functions via interactions with collagen fibrils, regulation of permeability throughout the stroma, and almost certainly the provision of a protective envelope from external influence for collagen. PGs are composed of a core protein covalently bound to one or more glycosaminoglycan (GAG) chains, where the core protein typically consists of multiple domains with distinct structural and binding features. As shown in Figure 3.1, two GAGs are attached to the core protein through covalent bound, and the GAGs are polysaccharide chains that varies in length that consisting of repeating disaccharide units. PGs may be classified by their associated GAG chain into heparan sulphate, chondroitin sulphate, dermatan sulphate, and keratan sulphate. However, PGs are also divided into families based on the structural features of their core protein. Important PG classes in the extracellular matrix include the basement membrane PGs, the hyalectans (or lecticans), and the small leucine-rich repeat PG (SLRP) family. Some SLRP family members are part-time PGs, and others such as opticin are always substituted with oligosaccharides instead of GAGs.

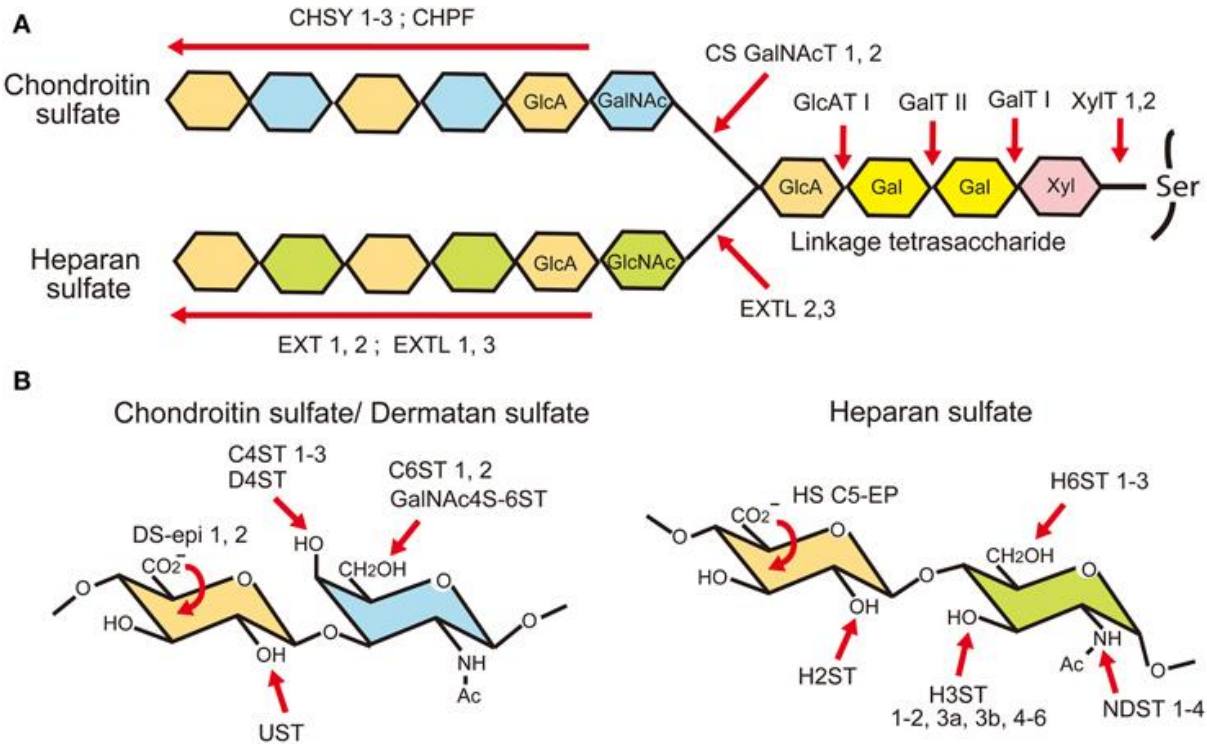

Figure 3.1 Structure of PGs (chondroitin and heparan sulphate) showing the polysaccharide-protein linkage region and the main disaccharide units. Gal, galactose; Xyl, xylose; GluA, ß-D-glucuronic acid; GalNAc, N-Acetylgalactosamine. ((Maeda, 2015)

The principal PGs of connective tissue have been characterised through complementary DNA cloning of the core proteins. Decorin and biglycan are two closely related PGs with protein cores of < 45 kDa and apparent molecular masses of 120 and 200 kDa, respectively. Decorin contains one chondroitin-dermatan sulphate GAG side chain, whereas two chondroitin-dermatan sulphate side chains may be attached to the biglycan core protein (Hitchcock et al., 2006). They are relatively small chondroitin-dermatan sulphate PGs and present in many connective tissues but differ in distribution and function. Decorin is present in close association with

collagen fibrils of many (if not all) connective tissues, where it regulates collagen fibril formation.

Additionally, large PGs have been identified in many connective tissues (Robinson et al., 2017). Aggrecan, a PG typically found in cartilage, is composed of a large (220 kDa) core protein and functions to provide tissue with resilience due to the water-binding capacity of its chondroitin and keratan sulphate GAG side chains (Roughley and Mort, 2014). The other form of large chondroitin sulphate PGs is called versican, identified in cultured human fibroblasts. Although these two PGs have large core proteins of similar size (>350 kDa) as determined by sodium dodecyl sulphate-polyacrylamide gel electrophoresis (SDS-PAGE), versican contains 15 to 17 chondroitin sulphate GAG side chains, whereas aggrecan contains more than 100 chondroitin sulphate chains and more than 30 keratan sulphate chains (Knudson and Knudson, 2001).

Since collagen, PGs, and GAGs are major targets of degradative enzymes in diseases such as osteoarthritis(Gerlie et al., 2000), it is imperative that researchers possess the means to quantify PGs in both healthy and diseased tissue precisely. This can be achieved by measuring s-GAGs in articular cartilage or a variety of body fluids such as synovial fluid, blood, or urine.

3.1.2 Proteoglycan in the sclera

The sclera is a connective tissue that provides the structural framework that defines the shape and axial length of the eye. The requirements of scleral strength, elasticity, and resiliency are largely met by connective tissue consisting of scleral fibroblasts embedded in a matrix of interwoven collagen fibrils of varying diameters. This

matrix is in close association with PGs that serve several biologic functions, including regulation the collagen fibrils and tissue hydration level, maintenance of structural integrity, growth regulation, matrix organization, cell adhesion, and binding of certain growth factors (Rada et al., 2000a). Three-dimensional reconstructions from electron tomography of human sclera reveal the d-periodic associations of proteoglycans with collagen in the tissue (shown in Figure 3.2), presumably indicative of their role in stabilising the fibrillar matrix and contributing to its rigidity and strength.

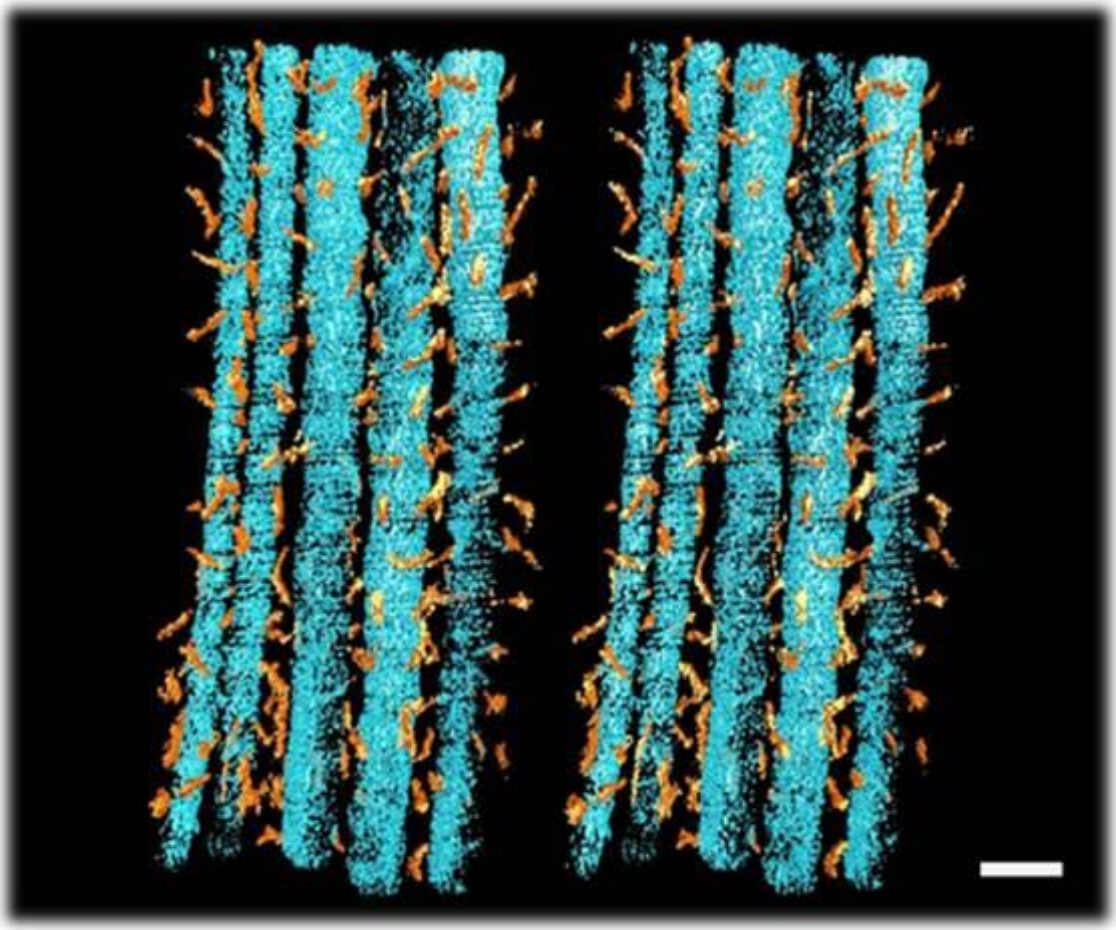

Figure 3.2 Stereo paired image of a three-dimensional reconstruction of proteoglycan (orange) and collagen fibrils (blue) from electron tomography from the sclera of an 89-year-old male donor (Watson and Hazleman, 2012b).

The sclera exhibits regional variation in structure and function. Human sclera is thickest at the posterior pole and thinnest at the equator, thickening at the corneal limbus. The posterior sclera contains the scleral canal and the lamina cribrosa for passage of the optic nerve. It also contains the sites of perforation by the long and short posterior ciliary arteries, the short ciliary veins, and the vortex veins. The anterior sclera is adjacent to the cornea at the corneal limbus and demonstrates a

significantly higher modulus of elasticity than the posterior sclera, resulting in significantly greater stiffness in the anterior sclera (Meek, 2008). Regional analysis of scleral GAGs indicates that chondroitin sulphate GAGs increases from the equator to the posterior region, reaching a maximum concentration at 2 mm around the fovea. The peripapillary area contains a high concentration of dermatan sulphate GAGs. The concentration of heparin sulphate GAGs is low throughout the sclera but highest in the anterior region to the equator, especially in the nasal limbus (Trier et al., 1990). Keratan sulphate GAGs have been found in the anterior region (Keenan et al., 2012a) but regional analysis has not been conducted by previous studies. Hyaluronic acid is the richest around the equator sclera (Trier et al., 1990). Although hyaluronan is not sulphated, other GAG chains contain sulphate substituents at various positions of the chain.

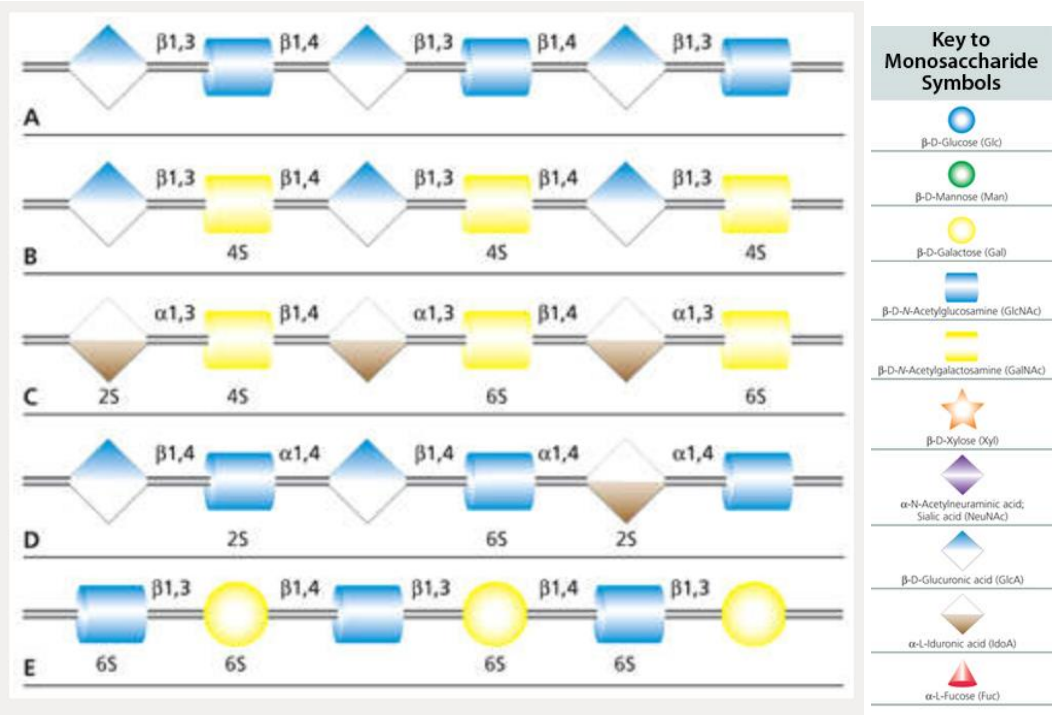

Figure 3.3 Carbohydrate sequences of the five types of GAG chains that have been reported in the sclera using monosaccharide symbols: (A) Hyaluronan; (B)

Chondroitin; (C) Dermatan; (D) Heparin; and (E) Keratan. Possible sulfation presence and location (2S, 4S, or 6S) is indicated. (Sigma-Aldrich, 2000)

PGs interact with many biologically active molecules via their core protein as well as their GAG chains, they are known to play important roles in the interactions between cells and the extracellular matrix, including the regulation of cell differentiation, proliferation, adhesion and migration. PGs also existed in and contribute to the other eye tissues, both chondroitin sulphate PGs and heparan sulphate PGs are important in determining axonal guidance from the retina (Clark et al., 2011). In addition, chondroitin sulphate PGs are essential in maintaining adhesion between RPE cells and the neurosensory retina. In Bruch's membrane, PGs are involved in the regulation of cell-matrix interactions, signalling and inflammation, and contribute to its filtration properties (Johnson et al., 2006).

3.1.3 Enzymes used in the proteoglycan research in ocular tissue

Chondroitinase is an enzyme that specifically degrades chondroitin and dermatan sulfates. Several research have used enzyme for proteoglycan depletion (Murienne et al., 2016, Murienne et al., 2015), (Van Haeringen et al., 1975),

3.2 Methods

3.2.1 Sample preparation

Five eyes of 6 to 9 month-old pigs (weight 32~34 kg) were obtained from a local slaughterhouse and prepared immediately on arrival (within an hour) at the

University of Liverpool. All eyes were obtained before the pigs were placed in a scalding tank (which has a water temperature around 60°C) to avoid tissue damage from high temperatures. Scleral tissue was cleaned of skin, fat, adherent muscle, retina, and choroid and was then dissected into anterior, equatorial, and posterior regions. The anterior region was defined as a circumferential belt adjacent to the corneal-scleral junction (5 mm wide). The equatorial region was decided as a circumferential belt located midway between the cornea-scleral junction and the posterior pole. The posterior scleral region was located at the posterior pole of the eye, excluding the lamina cribrosa and optic nerve head.

Tissues were then cut into small (<2 mm^2) pieces with a razor blade and divided into four groups treated for 48 hours in room temperature. In the first group, the specimens were incubated in ultra clean distilled water (control) (n=3 from each region for hydration and s-GAG quantification, n=1from each region for GAG staining). In the second group, they were incubated in α-amylase (A8220, Sigma-Aldrich, St. Louis MO) in distilled water at 2mg/ml (enzyme-treated) (n=3 from each region for hydration and s-GAG quantification, n=1from each region for GAG staining).In the third group they were incubated in a modified Trizma buffer at pH 8.0 with 60 mM sodium acetate and 0.02% bovine serum albumin aqueous (BSA) (control) (n=3 from each region for hydration and s-GAG quantification, n=1from each region for GAG staining). In the last group, they were incubated in Trizma buffer containing ChABC (Lyophilized (protease free), C2905, Sigma-Aldrich, St. Louis MO) at 0.5units/ml in the modified Trizma buffer (n=3 from each region for hydration and s-GAG quantification, n=1from each region for GAG staining). The

detailed protocol including the solutions used for s-GAG degradation can be found in section A of the Appendix.

3.2.2 Coomassie blue staining

In-gel protein visualisation has been facilitated by the use of an extensive and diverse array of stains. For 50 years, Coomassie Blue has been used to quantitatively assess proteins in-gel by densitometry. In recent years, proprotein detection accuracy has greatly increased, and it is now one of the most widely used methods with high-resolution results.(Gauci et al., 2013)

The Coomassie blue staining and dimethylmethylene blue assays were used here for analyse the depletion of PGs using two enzymes. Followed by sample preparation, the treated tissues were immediately frozen by liquid nitrogen, pulverised, then homogenised at 4°C overnight in 4 M guanidine-HCl containing 0.01 M sodium acetate, 0.01 M sodium EDTA, and protease inhibitor. The tissue residues were removed by centrifugation, with the supernatant collected by ECM protein extraction. The extracts were applied to dialysis for desalting, and lyophilised for harvesting the ECM protein powders. Lyophilised samples were subjected to gel electrophoresis analyses.

A urea solution of 7M with 1% SDS in 25 mM Tris-HCl (pH 7.0) and 2 mM PMSF (Sigma, USA) was added to solubilise 20 μg of protein powder. The concentration of protein lysates was measured using the BCA Protein Assay Kit (Bio-Rad, USA) according to the manufacturer's protocol. A colorimetric analysis was performed with a SpectraMax Plus plate reader. The lysates were then boiled at 95°C for 10 min and made ready for electrophoresis. The protein lysates were loaded onto

gradient gels and subjected to electrophoresis (100 V for 60 min) under reducing conditions. After electrophoresis, the gels were stained with 0.1% (w/v) Coomassie Brilliant Blue R-250 for 24 hours and then destained by soaking for at least 2 hours in 10% acetic acid, 50% methanol, and 40% H2O with at least two changes of this solvent. Finally the gels were imaged using a flatbed scanner (model BIO-5000 Bioscanner, Microtek, Hsinchu, Taiwan.) were used for imaging.

3.2.3 Dimethylmethylene blue (DMMB) assay

Dimethylmethylene blue assay is a method developed in an attempt to meet researchers' demands for a rapid, simple assay using readily available equipment. In the past decades, many groups undertook the onerous task of creating an easy, sensitive, and repeatable assay to quantify PG as s-GAG. For this purpose, attention was directed to spectrophotometric assays, including the dimethylmethylene blue assay. The 1,9-dimethylmethylene blue (DMMB) assay is widely used to measure sulphated GAGs in a variety of tissues and body fluids. This assay is based on the metachromatic property, which is the colour change (from blue to pink) produced by combining thiazine dyes with polyanions in biological tissues or fluids (Peters et al., 2008). It particularly shows reactions with chondroitin sulphates A and C, as well as keratan sulphate.

For this study, all treated samples were digested with an equal volume of papain (10 units/ml) in papain digestion buffer (1.36 g sodium acetate, 0.0326 g N-acetyl cysteine, 24 mM EDTA tetrasodium salt (0.48 ml of 0.5 M stock), 50 mM L-cysteine (87.8mg) made up to 100 ml, pH 5.8) at 60°C overnight. The papain-digested sclera samples were diluted 1:5 with water to make a total volume of 40 µl.

Subsequently, 250 µl of DMMB dye was added to each well. Results were read immediately from the plate reader at an absorbance of 570 nm. The s-GAG content was reported in µg/mg dry tissue weight by inferring the dry weight from the wet weight using the hydration data for the corresponding experimental group and quadrant. The solutions and detailed protocol used for s-GAG quantification can be found in the Appendix A. Enzymes used in this study were stored in -80^{o}C before use and personal protective equipment including gloves and lab coat were worn when handling enzymes to avoid contaminations.

3.2.4 Data analysis and statistics

sGAG content results were analysed with Origin (OriginPro 9.0) and expressed as mean ± standard deviations. Statistical significance was evaluated using the one-way ANOVA.

3.3 Results and Discussion

3.3.1 Regional analysis of PG core proteins

PGs were extracted from equal wet weights of anterior, equatorial, and posterior sclera and subjected to gel electrophoresis followed by Coomassie Blue staining. Protein bands were detected at 270, 130, 66 and 52 kDa (Fig. 3) in control groups without enzymatic digestion (A-, E-, P-). After digestion with ∝-amylase and chondroitinase ABC, four major core proteins were detected, migrating at approximately 270, 130, 66 and 52 kDa. However, there were significant regional differences observed after incubation with ∝-amylase and chondroitinase ABC.

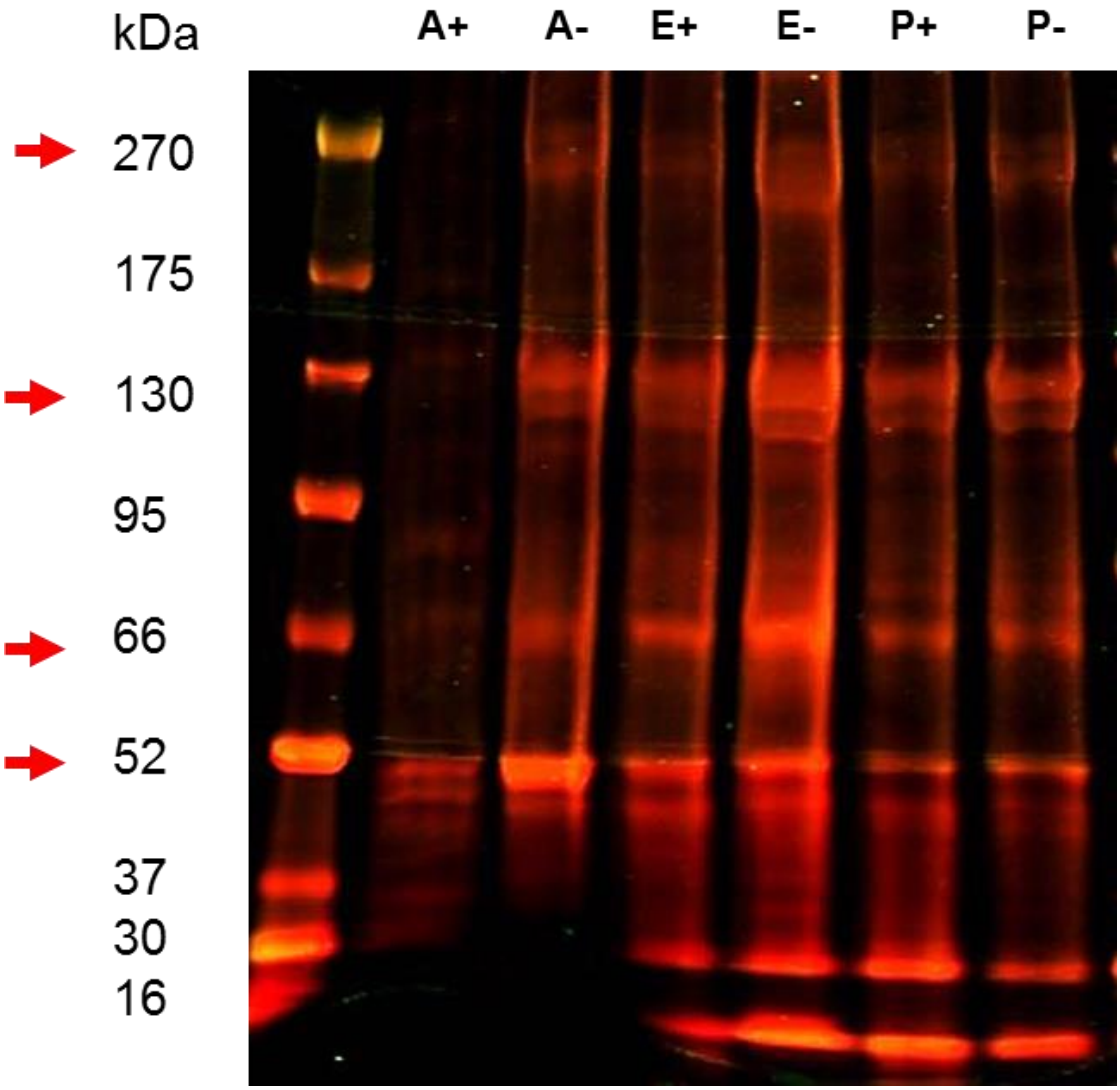

Figure 3.4 SDS-PAGE patterns of α-amylase incubated scleral protein. α-amylase incubated protein from anterior (A^+), equatorial (E^+), and posterior regions (P^+) each displayed a banding pattern distinct from the three regions from the control (A^-, E^- and P^-). Gels were stained with Coomassie Blue.

As shown in Figure 3.4, in the enzyme digested groups (E+, P+), no difference was found in the equatorial and posterior regions between control (lane 6) and with α-amylase (lane 5). However, there were significant regional differences observed in anterior region after incubated with α-amylase. Proteins with the molecular weight

of 270, 130, 66 and 52 kDa were all affected after enzymatic digestion with α-amylase. The results implied that the PGs in anterior region of sclera could be cleaved by α-amylase.

Figure 3.5 shows the pattern of chondroitinase ABC incubated with scleral protein. In the presence of chondroitinase ABC (A+, E+ and P+), the intensity of proteins with the molecular weight of 270 and 130 kDa were significantly reduced and digested by the enzyme. The patterns of all three regions were similar. The results suggested that large proteoglycans in whole sclera were cleaved by chondroitinase ABC. Different from α-amylase, Chondroitinase ABC shows no effect on the protein with the molecular weight smaller than 66 and 52 kDa in all three regions.

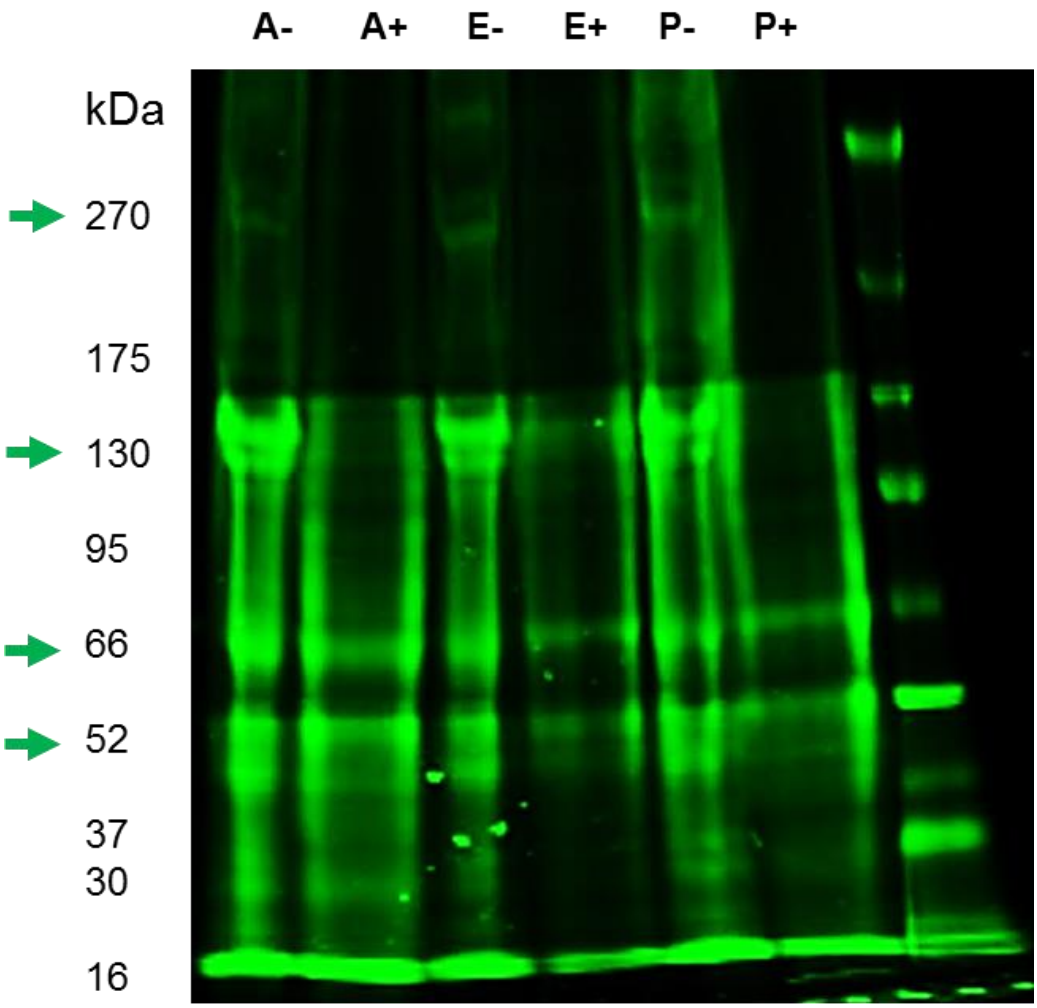

Figure 3.5 SDS-PAGE patterns of chondroitinase ABC incubated with scleral protein. Chondroitinase ABC incubated proteins from anterior (A+), equatorial (E+), and posterior regions (P+) each displayed a banding pattern distinct from the three regions from the control (A-, E- and P-). Gels were stained with Coomassie Blue.

3.3.2 Regional analysis of s-GAG quantification

The standard curve for the DMMB assay is shown in Figure 3.6.

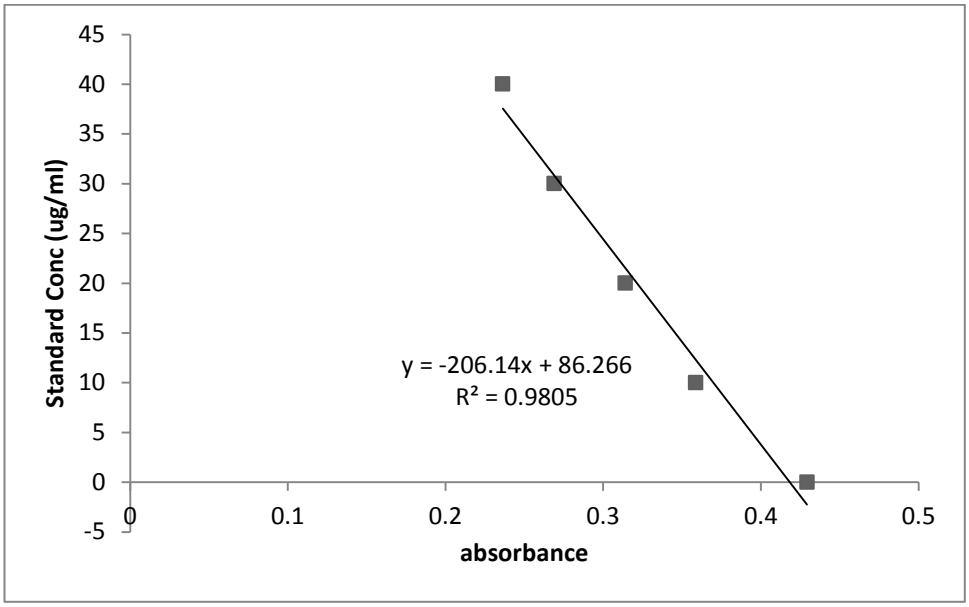

Figure 3.6 Calibration curve using Chondroitin Sulphate C (shark cartilage, Sigma C-4384) as standard.

The total s-GAG was measured from the anterior, equatorial, and posterior scleral regions of five porcine eyes. Scleral s-GAG content was obtained for the following three experimental groups: control, ∝-amylase, and chondroitinase ABC (Figure 3.7).

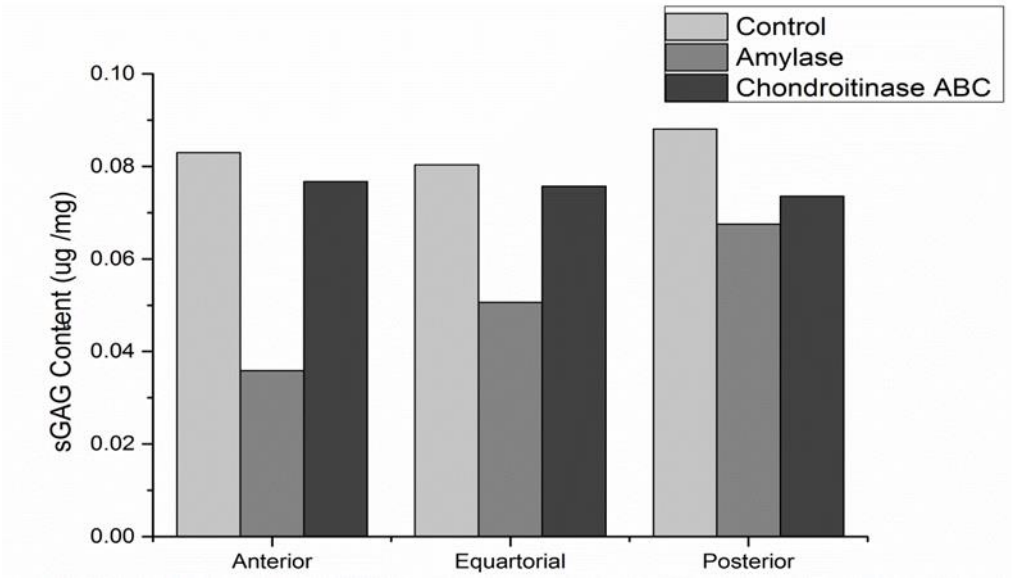

	reduced in (%) vs control group	p
amylase A	55.3	*
amylase E	42.5	*
amylase P	18.6	**
chondroitinase A	4.5	
chondroitinase E	11.4	**
chondroitinase P	14.0	**

Figure 3.7 s-GAG content measurement from anterior, equatorial, and posterior scleral regions of porcine sclera. Result are divided into three experimental groups: control, ∝-amylase, and chondroitinase ABC. (The standard deviations in this figure are too small to illustrate).

In the control group, the posterior region showed the highest level of s-GAG content (0.088 μg/mg), followed by the anterior region (0.083 μg/mg) and equatorial region (0.080 μg/mg). In the ∝-amylase group, statistical analysis showed a significant reduction of s-GAG content by 55.3% ($p \leq 0.05$) in the anterior region, 42.5% ($p \leq 0.05$) in the equatorial region, and 18.6% ($p \leq 0.01$) in the posterior region on average compared to controls. The s-GAG content was not significantly different between the control and chondroitinase ABC groups in the anterior region. However,

the equatorial region showed decreases in s-GAG content by 11.4% ($p \leq 0.01$) on average compared to controls, and 14.0% ($p \leq 0.01$) in the posterior region.

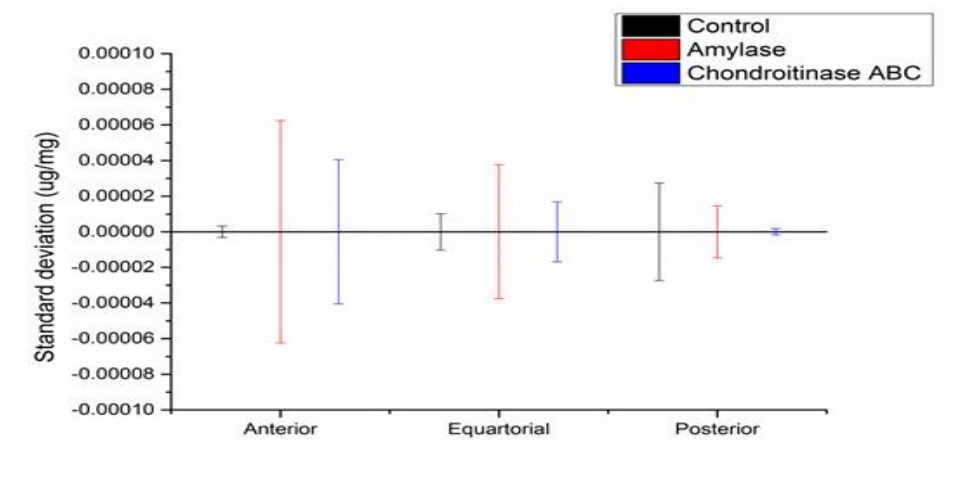

Figure3.8 Standard deviations of s-GAG content measurement from three regions of porcine sclera. Results are divided into three experimental groups: control, $\propto$-amylase, and chondroitinase ABC.

The variation in s-GAG content between samples (standard deviation) value within each group is very small compared to the average s-GAG content. However, this variation is significantly greater in enzyme-treated groups in the anterior and equatorial regions.

Changes in the ECM structure of the eyewall have been reported with both glaucoma and myopia (Rada et al., 1994, Murienne et al., 2016). These include variations in the PG content. As mentioned earlier, GAGs are polysaccharide chains of various lengths, the majority of which bind to core proteins to form PGs. The human posterior sclera is particularly rich in chondroitin sulphate GAG side chains, from the abundant presence of aggrecan, and in dermatan sulphate chains. An abnormal

accumulation of GAGs was reported in some portions of the anterior segment and in the lamina cribrosa of glaucomatous human eyes (Knepper et al., 1996). Similarly, rat and monkey lamina cribrosa showed a higher chondroitin sulphate content when subjected to IOP elevation (Murienne et al., 2015). A decrease in the overall GAG content was found in the sclera of myopic human eyes, also a decrease of s-GAG content was measured in tree shrew eyes with form deprivation myopia (Harper and Summers, 2015b). A decrease in GAG synthesis was also reported in the posterior sclera of form-deprived myopic tree shrew and monkey eyes (Rada et al., 2006).

It seems that PG interactions with collagen not only occurs through binding of the core protein, but also through electrostatic interaction of the GAGs themselves as shown *in vitro* (Rada et al., 1993). The majority of GAGs are highly polar, attracting water due to their negatively charged carboxyl and sulphated groups. Their fixed charge density also creates repulsion and attraction forces among themselves and with the collagen fibrils, respectively. As a result, the GAG content regulates tissue hydration by determining the number of polar sites for water binding as well as tissue osmotic pressure (Raspanti et al., 2008). However, tissue swelling is limited by the hydration state of the tissue, the stiffness of the collagen network, as well as the repulsion and interactions between the GAGs that determine the space for free water uptake (Scott, 1988). GAGs have been hypothesised to regulate the collagen interfibrillar spacing through their water-binding capacity, osmotic pressure, GAG charge repulsion, and GAG antiparallel interactions. GAGs have also been shown to regulate collagen fibrillogenesis *in vitro* under certain conditions, specifically affecting the rate of fibril formation and fibril diameter (Kurylo et al., 2016).

For the GAG composition of the human sclera, previously reported data indicated that the sclera contains chondroitin sulphate (28% to 48%), dermatan sulphate (29% to 49%), heparan sulphate (2% to 12%), and hyaluronan (19% to 33%) (Borcherding et al., 1975). The amount of each GAG present varies within different regions of the sclera and with age. There are also significant regional variations of GAGs in the sclera. For the s-GAG content in scleral regions, chondroitin sulphate increases from the equator to the posterior region and reaches maximum concentration at 2 mm around the fovea. The peripapillary area contains a high concentration of dermatan sulphate. The concentration of heparin sulphate is low throughout the sclera but highest in the anterior region to the equator, especially in the nasal limbus (Trier, et al., 1990). Concentrations and distributions of s-GAG in the sclera are shown in Figure 2.8 in Chapter 2.

From the s-GAG content measurement results in this study, the highest level of s-GAG was in the posterior region, while the lowest was in the equatorial region. The trend of the data is consistent with those previously measured in all three regions in the human sclera (Rada et al., 2000a).

The s-GAG content measurement result in tissue incubated with $\propto$-amylase compared with control showed reductions in all three regions. This result, along with the protein analyses, indicates that $\propto$-amylase results in proteoglycan depletion. However, the s-GAG content is reduced the most in the anterior region and least in the posterior region. This trend is the opposite of incubation with chondroitinase ABC, which is reduced most in the posterior region and least in the anterior region. This reduction shows the matches the distribution of chondroitin and dermatin

sulphate GAGs in the sclera. This difference indicates that ∝-amylase has no effect on the s-GAGs depleted by chondroitinase ABC, namely, chondroitin sulphate and dermatan sulphate.

Decorin, biglycan, aggrecan, and other small interstitial leucine-rich repeat proteoglycans (SLRPs) have been reported in sclera by Rada et al. (Rada et al., 2015, Rada et al., 2006, Rada et al., 1997, Rada et al., 2000a, Norton and Rada, 1995) as shown in Table 3.1. SLRPs are key regulators of collagen fibril and matrix assembly. The most abundant SLRPs in the sclera are decorin and biglycan, with one or two dermatan/chondroitin sulphate GAG chains, respectively. Decorin and biglycan share a common binding site for type I collagen, with decorin binding to type I collagen with a greater affinity than biglycan. Aggrecan was found in sclera in 1997 (Rada et al., 1997) and has been suggested to play an important role, as it does in the cartilage, in providing the sclera with compressive stiffness and the ability to resist the tensile stresses resulting from changes in intraocular pressure. A list of PGs found in sclera is shown in Table 3.1.

Table 3.1 PGs in the sclera and their core protein weight, apparent molecular masses, and s-GAG chains.(Young et al., 2003, Kurylo et al., 2016, Michelacci et al., 2003, Dunlevy and Rada, 2004)

Proteoglycan	Core protein (kDa)	Apparent molecular masses (kDa)	Glycosaminoglycan (number of chains)
Decorin	38.8	90-140	CS, DS
Biglycan	42	>200	CS, DS
Fibromodulin	42	67	KS

Syndecan-1	~32	77	HS
Lumican	70~80	>200	Unsulphate KS
Aggrecan	210~250	>2,500	CS, KS

For this study, there are significant variations in the pattern of scleral protein incubated with α-amylase and chondroitinase ABC. α-amylase is most impactful in the anterior region, and least in the posterior region. Conversely, chondroitinase ABC shows the most effective in the posterior region and least in the anterior region. Furthermore, chondroitinase shows an effect on proteins in weight 130 and 270 kDa, especially in the posterior region. The proteins affected by chondroitinase share similarities in the regional distribution and apparent molecular weight with decorin and biglycan. However, no change was found in the sclera protein with weights 66 and 52 kDa in all three regions incubated with chondroitinase ABC. α-amylase results in a decrease in density of all bands in 270, 130, 66 and 52kDa in the anterior region, but none in the posterior region. Although α-amylase depletes PGs with apparent molecular weights 270 and 130, this regional distribution suggests the proteoglycan depleted by α-amylase are not decorin and biglycan.

Although this result shows that α-amylase will cause proteoglycan depletion in the sclera tissue, the types of PGs that effect by α-amylase still need to be further investigated. The exact PGs that depleted by α-amylase can be identified using protein quantification technique like mass spectrometry or western blotting.

Finally, the possibility of enzyme contamination must be considered in this study. An impure enzyme could cause uncertainty in the result like difference in results between each treatment (large standard deviations). Enzyme contamination can be avoided by using inhibitors.

3.4 Conclusion

This chapter explored the two enzymes used in this study by protein analysis and s-GAG content measurement. Findings from this chapter will be used to provide a better understanding of the role that play in the nanostructure and mechanical function of the sclera. The main findings were:

- The significant reduction of PGs that were observed following the tissue being incubated with the enzymes indicated that both α-amylase and chondroitinase ABC result in proteoglycan depletion in the sclera tissue.
- Unlike assumed in previous studies on the effect of proteoglycan depletion on scleral mechanical properties (Murienne et al., 2016) the effects of both α-amylase and chondroitinase ABC on PGs are not regionally homogenous.
- The two enzymes used for proteoglycan depletion in this study target different type of PGs.

Chapter 4 Collagen fibril Structure Mapping with AFM

4.1 Introduction

The sclera response to the mechanical maintains the eye's shape by maintaining intra-ocular pressure. It also protects the eye from external harms. Type I, III, V, VI, and XII collagen are present in sclera and they exist in different collagenous structural groups (Table 4.1), including fibrillar collagen and non-fibrillar collagen groups (Keeley et al., 1984, Jerome et al., 1957). Among all types of fibrillar collagen, type I collagen (99%) is primarily composed in the sclera.

Table 4. 2 Collagen types within the sclera (Meek, 2008, Shoulders and Raines, 2009, Karsdal et al., 2016)

Type	Nano-Structure	Structure Class	Main Function
I	300nm molecule length, 67nm banded fibrils	Fibrillar	Resistance to tension
III	67nm banded fibrils	Fibrillar	Structural maintenance in expansible organs
V	390nm molecule, N-terminal globular domain	Fibrillar	Participates in type I collagen function
XII	Large N-terminal domain; interacts with type I collagen	FACIT	Interacts with type I collagen
VI	Non-fibrillar collagen	Network	Maintaining tissue integrity

Unlike in the cornea (fibril diameter around 30nm), fibrils in sclera have a wide range of diameters (between 25 and 260 nm) (Yamamoto et al., 2000, Watson and Young, 2004). Fibrils in sclera group together into collagen bundles ~0.5-0.6 μm thick; these collagen bundles are knitted together in different orientations, all contributing to the structural framework of the sclera. The most characteristic feature

of a collagen fibril is its D-periodicity. For collagen types I and III, the D-periodicity = 67nm. This is dictated by the collagen molecule's banding pattern. Collagen fibril structure studies were first proposed by Hodge and Petuska (Hodge, 1963), and many groups have made efforts in this field since then. Apart from collagen fibrils diameter and D-period, Spitzner et al. (2015) has revealed that Gap-zone (Gap between overlaps regions in collagen fibril) depth of type I collagen fibrils is highly influenced by collagen fibril hydration level. Figure 4.1 shows the single Type I collagen surface profiles in different level of relative humidity (RH).

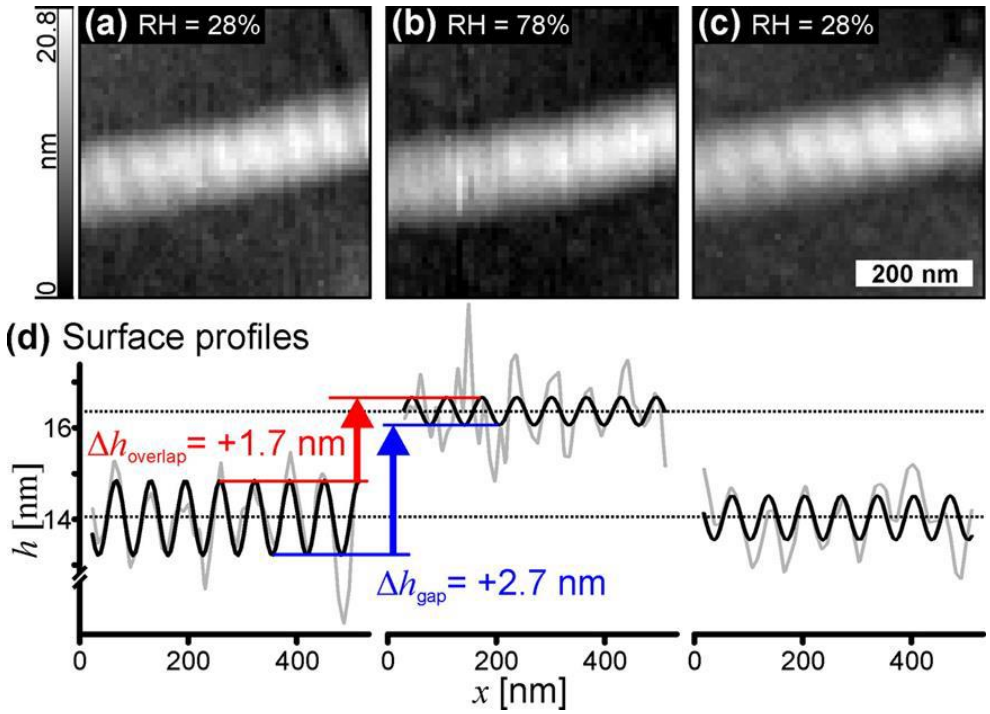

Figure 4.1 AFM images of the Type one collagen fibril surface profiles before (a), during (b), and after (c) swelling. (d) Mean of four adjacent profiles along the fibril's main axis (grey) and a sinusoidal fit (black). The collagen gap zone depth reduced when hydration level increased. (Spitzner et al., 2015)

Collagen interacts with PGs and glycosaminoglycans during fibril formation, influencing the eventual numbered the thickness of collagen fibres, and possibly regulating the mature fibre (Watson and Hazleman, 2012a).ÖBrink (1973)has revealed that chondroitin sulphate, dermatan sulphate PGs accelerate fibre formation while keratan sulphate proteoglycan may have slight decelerating effect. The collagen-proteoglycan interaction in and sclera has been observed by researchers with different techniques (Meek, 2008, Ho et al., 2014, Young, 1985a, Watson and Young, 2004). However, no research so far has observed the ultrastructure change in sclera tissue following proteoglycan depletion.

Scanning electron microscopy (SEM), transmission electron microscopy (TEM) and atomic force microscopy (AFM) are the most popular methods for collagen structure imaging (Robinson et al., 2017, Yang et al., 2015, Wang et al., 2015). SEM and AFM can both provide high resolution, 3D images. TEM provides 2D, cross-sectional images that are often used for collagen fibril diameter measurements. However, it is difficult to use this technique on tissues like sclera, because the collagen fibrils in these tissues are "knitted" together, and they do not all flow in the same direction. SEM and AFM can both provide 3D images. SEM and TEM requires special treatment for the sample before testing, however, AFM sample preparation does not require sample treatment and the AFM samples can be tested in ambient conditions air, liquid, or other controlled environments. AFM provides topographic contrast direct from height measurement, and it does not need sharp edges or special image processing methods to generate good topographic contrast in images. Several studies have been already published on AFM observation of collagen fibrils. As for sclera, Meller et al (Meller et al., 1997)observed slices of the human sclera tissue by

AFM in a contact mode. On the other hand, we previously (Yamamoto et al., 2000) investigated isolated bovine and human scleral(Yamamoto et al., 2002) collagen fibrils with a noncontact-mode AFM and analysed the ultrastructure of the collagen fibrils. Furthermore, there are other studies also measured collagen fibrils structure while testing their mechanical properties. Collagen fibrils structure results from previous studies are shown in Table 4.2.

Table 4.2 Morphological characteristics of scleral collagen fibres studied by various techniques.

Author	**Tissue**	**Technique**	**D-periodicity (nm)**	**Diameter (nm)**	**Gap zone depth (nm)**
Spitznas et al. (1970)	Rabbit sclera	SEM & TEM	70	150–250	-
Spitznas and Hogan (1970)	Human sclera	SEM & TEM	65	62–125	-
Komai and Ushik (1991)	Human sclera	TEM	-	20–230	-
Fullwood et al. (1995)	bovine sclera	AFM	55–67	up to 900	-
Meller et al. (1997)	Human sclera	AFM	77	118 - 1268	~ 0.42
Yamamoto et al. (2002)	Human sclera	AFM	65.7 ± 1.1	204.2 ±62.9	6.16 ± 1.3
Grant et al. (2011b)	Porcine sclera	AFM	64.2 ± 2.0	-	-
Choi et al. (2011)	Human sclera	AFM	69.1 ± 14.2	98 - 220	-
Papi et al. (2014)	Porcine sclera	AFM	-	104 - 294	-

Most of the previous studies measured the collagen structure manually with AFM build-in software. Method of measuring collagen diameter and D-periodicity shows

in Figure 4.2. in this method, researcher manually draw a line along collagen fibrils and read the height curve from this line, then calculate the diameter and D-periodicity with this curve. This method may cause errors since the result value could be greatly influenced by the orientation of the line. This error cannot be eliminate even a software is used for drawing a straight line since the collagen fibril has its natural curve.

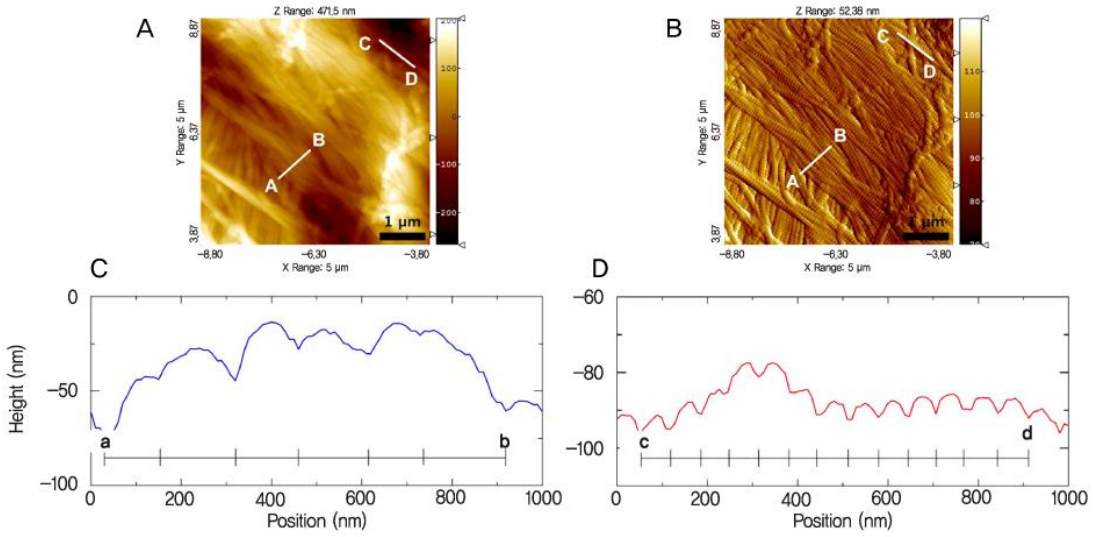

Figure 4.2 outer layer of hydrated human scleral collagen fibril diameter (C) and D-period (D) measurements using line profiling plots on AFM topography (A) and deflection images (B) in a scan size of 5 × 5 µm^2.(Lee et al., 2011)

4.2 Method

4.2.1 Sample preparation

Collection and cleaning in accordance with the preparation method in chapter 2, porcine scleras from five porcine eyes were then dissected into anterior, equatorial, and posterior regions. Three locations of 4 mm^2 blocks were taken from each region by a double-blade cutting tool; the location of the cuts is shown in Figure 4.3. The

dissected tissue was then embedded (outer layer up) in optimal cutting temperature (OCT) resin (Tissue-Tek, CellPath, Powys, UK), tissue locations and directions were labelled on the emerging cryomold (N: nasal, T: temporal. S: superior, I: inferior) for all sample. The embedded tissues were then snap-frozen with isopentane and liquid nitrogen for cryosectioning (with a Leica CM1850 cryostat, Leica Microsystems (UK) Ltd, Milton Keynes). Four Specimens with thickness of 5 μm were sectioned along the outer sclera from each block using a Leica CM1850 cryostat (Leica Microsystems (UK) Ltd, Milton Keynes), and they were then stored at -80^{o}C until testing time.

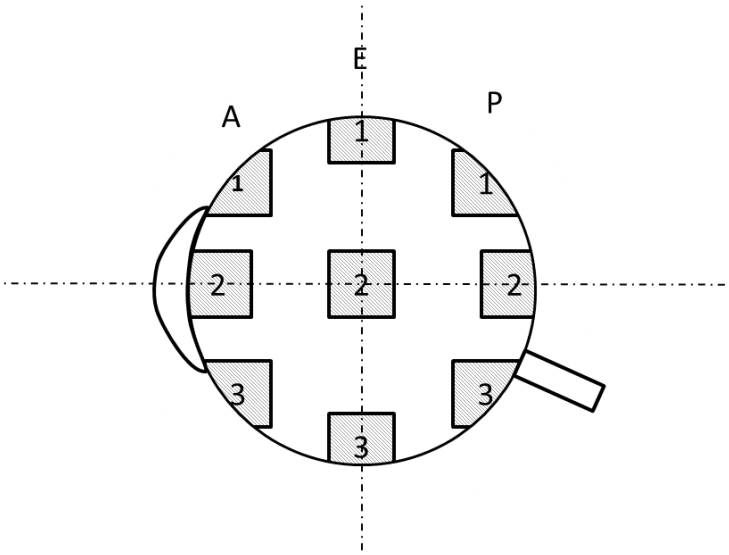

Figure 4. 3 Schematic of nasal view of a porcine eye globe (left) showing the anterior (A), equatorial (E), and posterior (P) regions from where the tissue was dissected, figure adapted from Papi et al. (2014).

4.2.2 AFM Peakforce QNM in air

Peakforce quantitative nanomechanical mapping (QNM) in air was used in this study for scleral tissue nanostructure mapping. The same technique however ever in liquid was used for mechanical mapping with same environment, frequency and scan size

(to keep the technique method consistent and the results comparable; see Chapter 5). Peakforce QNM is an AFM mode that is most suited for biological samples with structural heterogeneity (Pittenger et al., 2010b). In probe scanning techniques with normal scan forces, there are two main causes of tip and sample damage. Any lateral force that the tip exerts on the sample will cause the sample to tear, and likewise, lateral force from a hard sample will cause tip damage (Pittenger, Erina & Su 2010). Peakforce QNM controls the maximum force (i.e. the PeakForce), allowing for the detection of quantitative nanomechanical data directly from the sample.

Experiments were performed using a Bruker MultiMode 8 AFM and Tap150A probes (MPP-12120-10, Bruker Nano Inc., Nano Surfaces Division, Santa Barbara,CA). The probes (see Figure 4.4) were selected based on previous experiments on sclera tissue (Papi et al., 2014) and the recommendations of Bruker AXS for range of polymer Young's moduli to be investigated (5-500MPa—values based on IIT measurements).

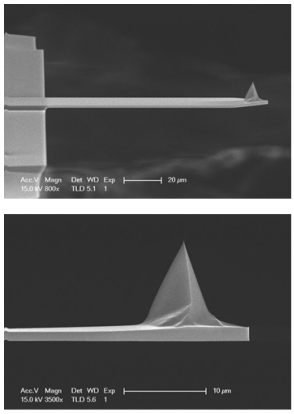

Tip Reference	RTESPA-150
Cantilever Geometry:	Rectangular
Tip Height (h):	10 - 15µm
Spring constant (N/m)	5
Tip Radius (Nom):	8 nm
Tip Radius (Max):	12 nm
Material:	0.01 - 0.025 Ωcm Antimony (n) doped Si
Cantilever Back Side Coating:	Reflective Aluminum

Figure 4.4 Cantilever and tip used in this study (Bruker Nano Inc.)

The relative calibration method was used before every testing group. PhotoStress Coating 1 (PS1, modulus of elasticity= 2.7Gpa±0.1Gpa) was used as a reference sample to adjust the tip radius. Deflection sensitivity was tested on a sapphire sample (SAPPHIRE-12M, PFQNM-SMPKIT-12, Bruker Nano Inc., Nano Surfaces Division, Santa Barbara,CA). Spring constant was also measured with thermal tune. The reference samples was tested again for each sample to make sure that the results were accurate (as shown in Figure 4.5)

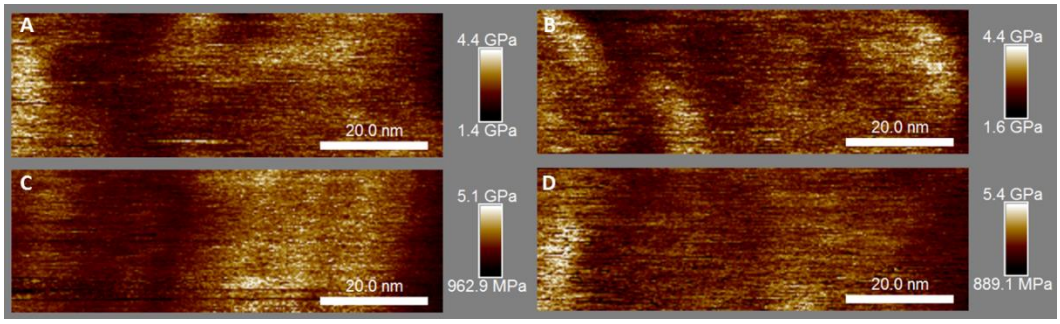

Figure 4.5 PS1 reference sample DMT results from pre (A=2.72 GPa, C= 2.82 GPa) and post (B=2.86 GPa, D=2.86 GPa) testing for one sample while all parameter stay the same (Tip Radius: 12nm, Deflection sensitivity : 27 nm/V).

The cryosectioned tissue (total n=180, Three regions of five eyes, three repeats sample for each region for each treatment group) was treated with the following solutions: 2mg/ml α-amylase in phosphate buffered saline (PBS), α-amylase (2 mg/ml, from Aspergillus oryzae, Fungamyl® 800L, activity ≥0.8 units/g, Sigma-Aldrich, St Louis, MO, USA) in distilled water, chondroitinase ABC (0.5unit/ml in a modified Trizma buffer at pH 8.0 with 60 mM sodium acetate and 0.02% BSA, C2905, Sigma-Aldrich, St Louis, MO, USA), 100% ultra-clean distilled water (control group), and 100% PBS (control group). All tests were conducted at room temperature (22^{o}C). The specimens were rinsed carefully with distilled water to

remove OCT, and they were then left to dry for 30 minutes. Drying in room temperature for 30 minutes is the time for liquid vanish from sample surface and not cause sample dehydration, this has been decided by observing sample surface by using 40x optical microscope. Before testing, 15 µm and 7 µm images were taken to finding the best testing locations. As shown in Figure 4.6, collagen fibrils in the selected bundle were complete (not covered or damaged by sectioning) and arranged along the same orientation.

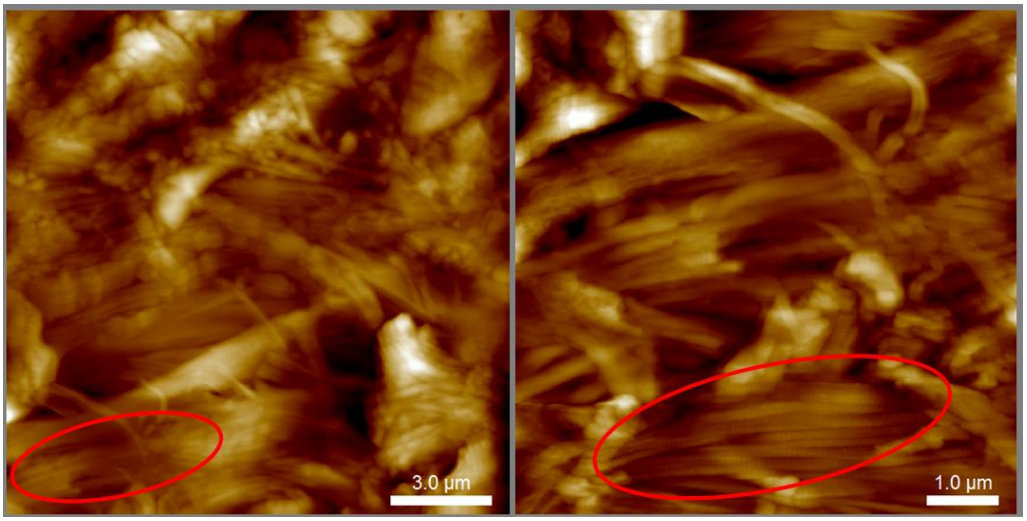

Figure 4.6 Selection of testing location. (a) This figure shows a typical 15µm image and (b) This figure shows a typical 7µm image. The selection of collagen fibril bundle (red oval). Testing locations (1.5µm ×1.5µm) were chosen along this bundle.

During testing, the starting point location on the specimens (i.e. where the point of testing parameters were: X-Offset=0, Y-Offset=0 and scan angle=0) was captured with an integrated optical microscope. Then, 10 images with a size of 1.5 µm × 1.5 µm were captured along the selected bundle and the coordinates (X-Offset and Y-Offset) of these locations were recorded. For the treatment, the specimen remained in

the AFM sample stage and was treated with a 0.04 ml solution (including the control group) for 1 hour and then washed with distilled water 3 times to stop any ongoing reaction. It was then dried for 30 minutes. The treatment testing start point (as shown in Figure 4.4) was found by the Matlab (Matlab 2013a) algorithm and the same locations and coordinates were captured again for comparison (Figure 4.7). Once all testing was complete, the reference sample (PS1) was tested again to ensure that the results were accurate.

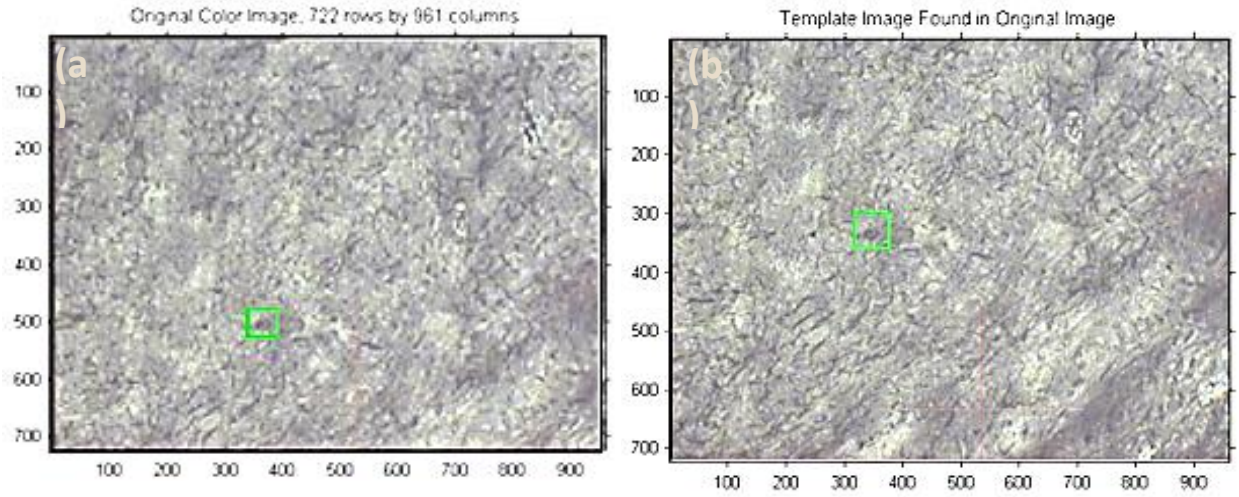

Figure 4.7 AFM probe scanning start point in (a) was found by Matlab localization algorithm after depletion (b).

4.2.3 Image processing and analysis

Collagen fibril topography parameter measurements (Figure 4.8a) were performed off-line on AFM height result images. Figure 4.8c shows the surface profiles of a single collagen fibril extracted manually from the AFM height image (Figure 4.8b) by using the 'section' tool (NanoScope Analysis 1.7, Bruker Nano Inc., Nano Surfaces Division, Santa Barbara, CA). The contiguous height difference of peak and valley on this curve were calculated automatically with Matlab script (Matlab 2013a)

as the gap zone depth. The contiguous horizontal difference of peak and peak on this curve was calculated with the same method as approximate D-periodicity. These results were used to decide the threshold of result filtering for the ‘rectangle’ method.

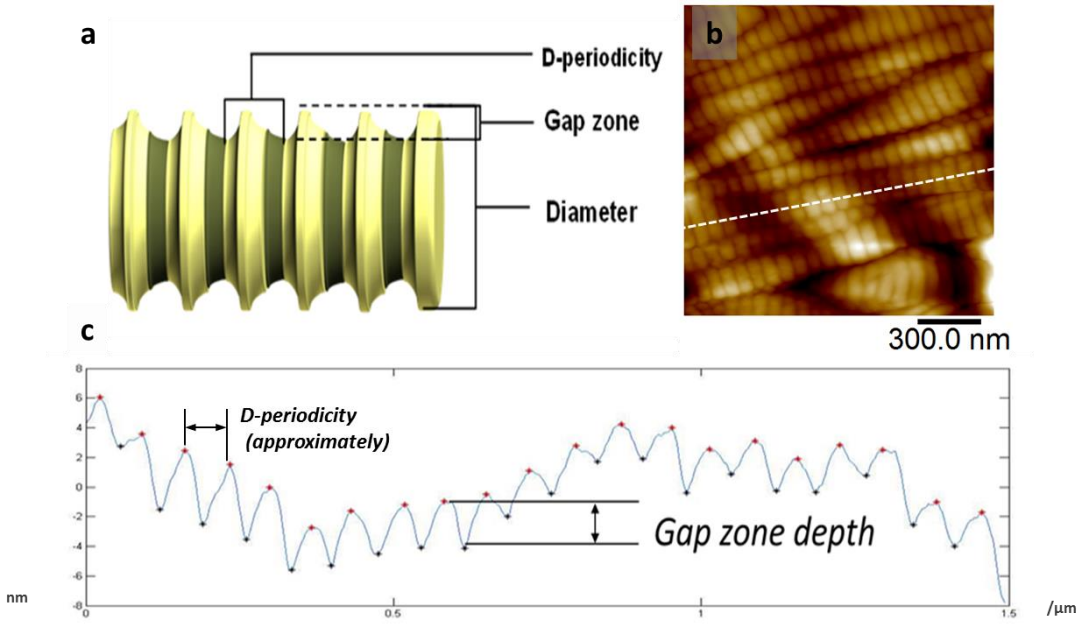

Figure4.8 (a) Collagen fibril parameters (diameter, D-periodicity, and gap-zone depth) were measured and compared with image analysis techniques in this study. A single collagen fibril was selected manually from the (b) AFM height image for the gap zone depth measurement. The contiguous height difference of peak and valley in the (c) exported curve is the value of the gap zone depth; this was calculated through an algorithm.

Collagen fibril diameter and D-periodicity were measured via the ‘rectangle’ method (Figure 4.9) using Image SXM (Barrett, 2008). Specific macros were developed for analysing collagen fibrils in AFM images with a resolution of $\geq 512^2$ pixels.

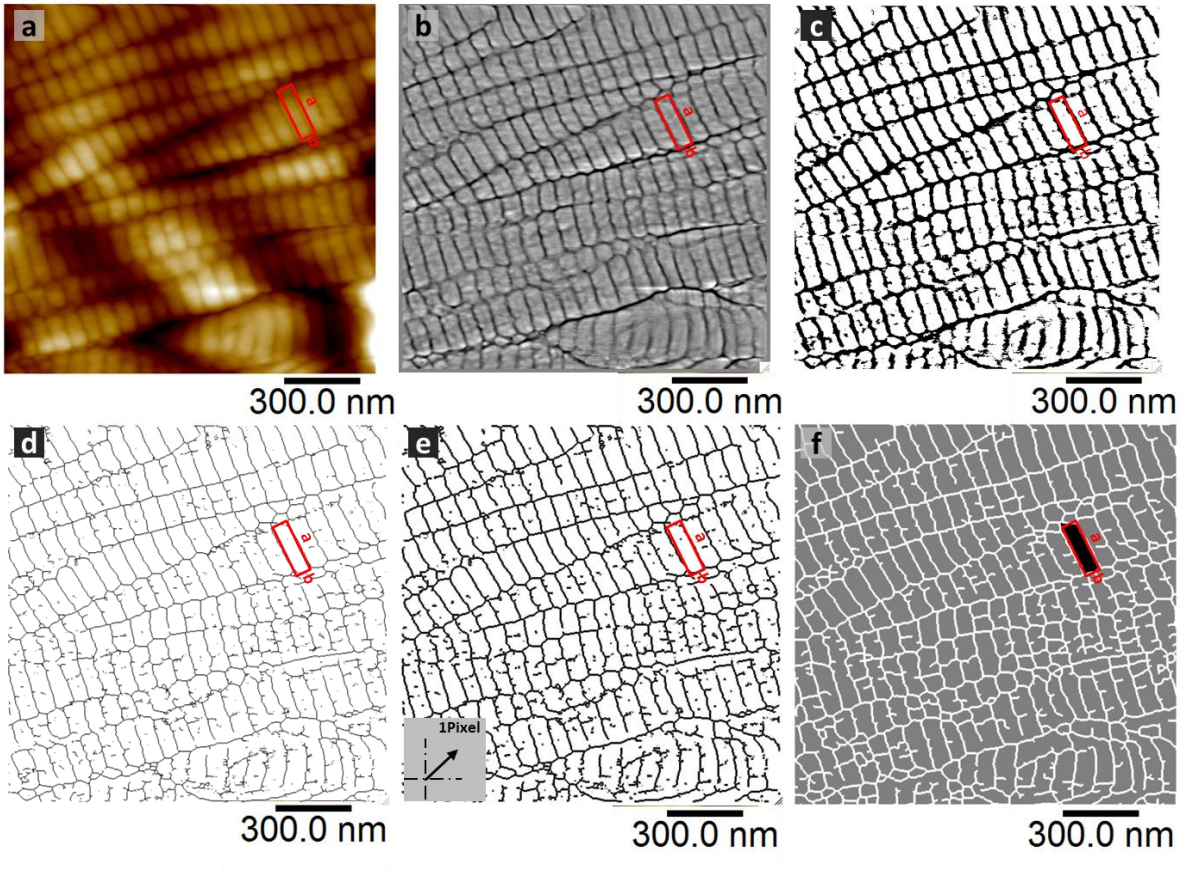

Figure4.9 Image processing and analysing method for the 'rectangle' method.

During the ‘rectangle’ analysing method, collagen fibril edges in the original image (Figure 4.6 a) were sharpened through an unsharp masking method (b). The processed image was then binarized to a black and white image using an automatically selected threshold only to leave the collagen structure lines (c). In image (d), collagen structure lines were reduced to a single-pixel-wide skeleton for unification. The skeleton image was then copied, pasted, and shifted 1 pixel towards the marking direction (e) to increase the closed areas. The section of 1 D-period of a single collagen fibril was extracted as a rectangle; diameter and D-periodicity (‘a’ and ‘b’ values) were calculated through the following equations:

$$\text{Diameter} = \frac{L}{4} + \sqrt{(\frac{L}{4})^2 - A} + \frac{2 \times line^2}{Image\ Size(nm)^2} \quad (4.1)$$

$$\text{D} - \text{periodicity} = \frac{L}{2} - Diameter + \frac{2 \times line^2}{Image\ Size(nm)^2} \quad (4.2)$$

Where *L* and *A* are the length and area of the 'rectangle', and 'line' is the number of AFM scanning lines. The error results were filtered out using D-periodicity thresholds that were predefined by the aforementioned method.

4.2.4 Data analysis and statistics

Collagen structure parameter results were analysed with Origin (OriginPro 9.0) and expressed as mean ± standard error of mean. Statistical significance between pre and post-treatment were evaluated using the one-way ANOVA. (If a p-value is less than 0.05, it is flagged with one star (*). If a p-value is less than 0.01, it is flagged with two stars (**). If a p-value is less than 0.001, it is flagged with three stars (***). If a p-value is less than 0.0001, it is flagged with four stars (****))

4.3 Results

Each tissue sample was first scanned in room temperature without treatment; the scleral nanostructure was captured and analysed. Then the same collagen bundle (shown in Figure 4.10) was found again using the relocation method after treatment, and the collagen fibril parameters were measured for comparison.

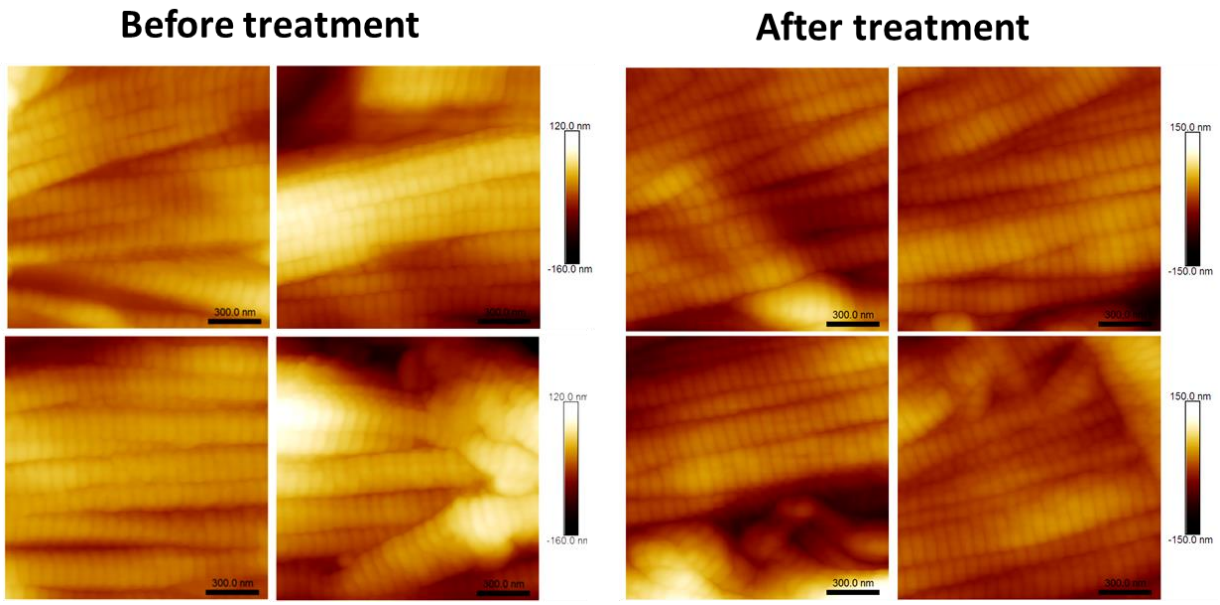

Figure 4. 10 AFM images captured from same location on the same collagen bundle before and after treatment.

Collagen fibril diameters and D-periodicities were calculated with the 'rectangle' method as mentioned in the methodology. And the collagen gap-zone depths were calculated using Matlab algorithm with the surface curve extracted with AFM build-in software. Results showed below were from all three regions of five porcine eyes.

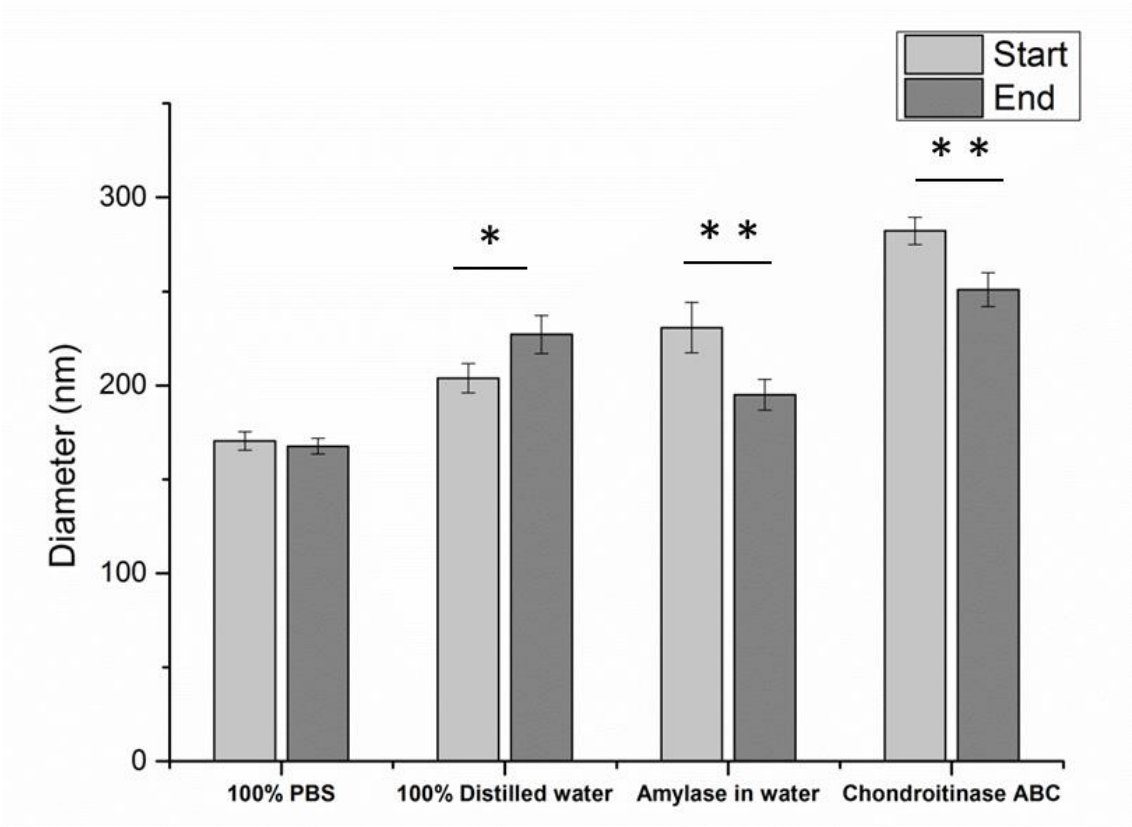

.

Figure 4. 11. Collagen fibril diameter results in pre- and post-buffer treatment images (Total n= 900 images/group. Three regions of five eyes, three repeats sample for each region and ten images for each before and after each treatment).

There was no statistical significant difference found in the collagen fibril diameter results after PBS treatment (Figure 4.11). Collagen fibril diameter increased significantly after incubation with 100% distilled. Collagen diameter decreased significantly after incubation with α-amylase and chondroitinase ABC incubation.

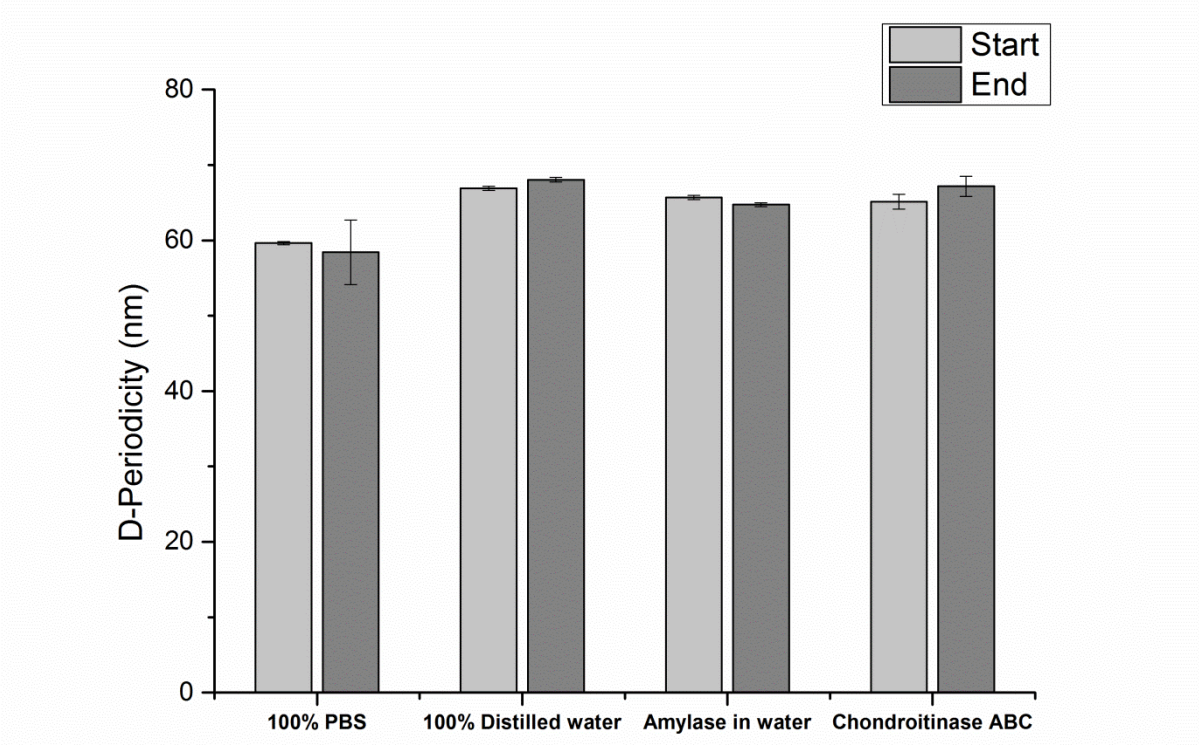

Figure 4.12. Collagen fibrils D-periodicity results in pre- and post-buffer treatment images (n= 900 images/group, Three regions of five eyes, three repeats sample for each region and ten images for each before and after each treatment).

There were no statistically significant differences found in the D-periodicity results (Figure 4.12) after any of the treatments. The mean value of collagen D-periodicity was between 60 and 70 nm.

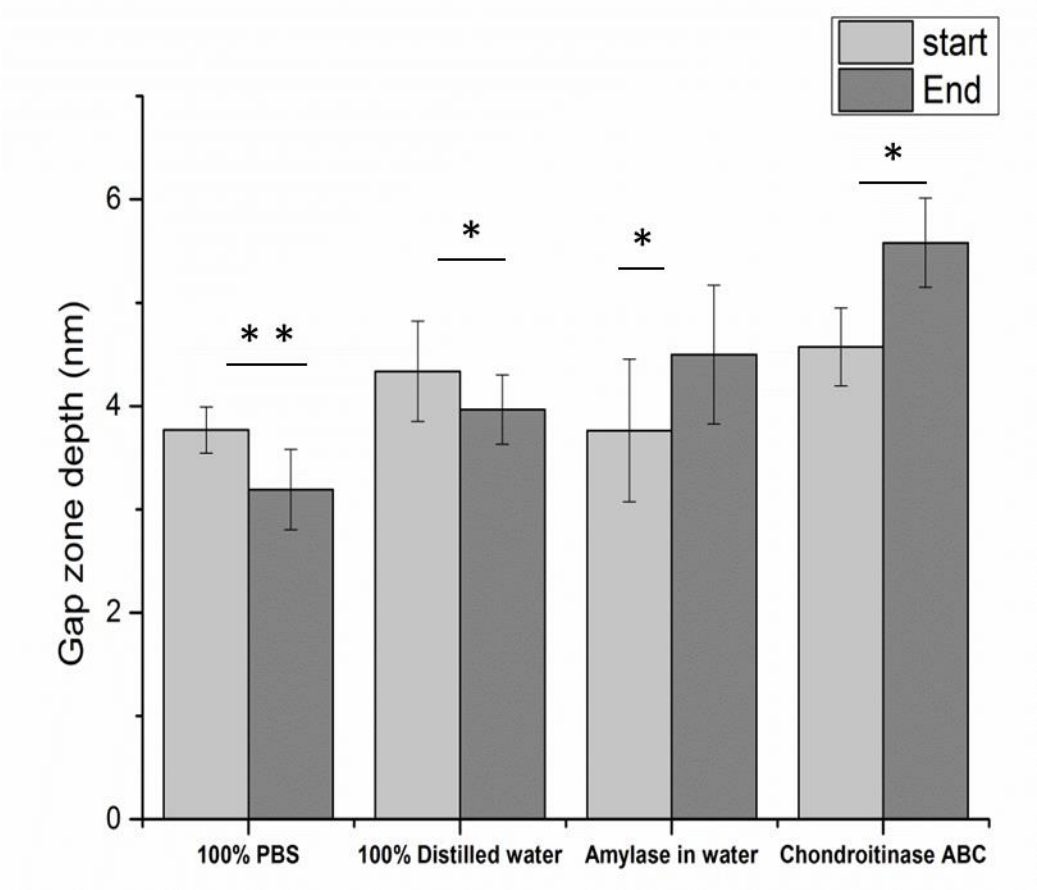

Figure 4. 13 Collagen fibril gap zone depth results in pre- and post-buffer treatment images (n= 900 images/group, Three regions of five eyes, three repeats sample for each region and ten images for each before and after each treatment).

Collagen fibril gap zone depth (Figure 4.13) decreased after being hydrated with 100% distilled water and PBS. It increased after α-amylase treatment and chondroitinase ABC treatment.

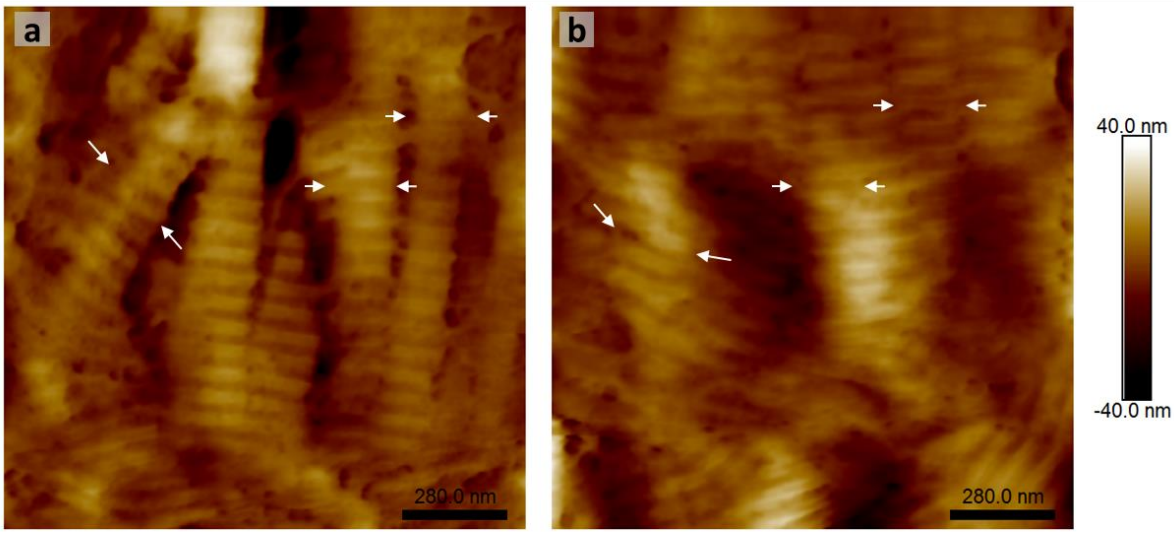

Figure 4. 14 Collagen fibrils fused after treatment with α-amylase. (a) is the 1.4μm AFM image before incubated with α-amylase and (b) is the image captured from same location on the tissue after incubation. White arrows indicated the locations of same collagen fibrils before and after incubation.

Collagen fibril fusion was noticed in some small scale images (1.4μm) of the amylase-incubated tissue. As shown in Figure 4.14, distance between collagen fibrils became extremely small and the edge of collagen fibrils disappeared in the image after incubation. Some of the collagen band from one collagen fibril even seems ‘’staged’’ into another fibrils.

Distilled water

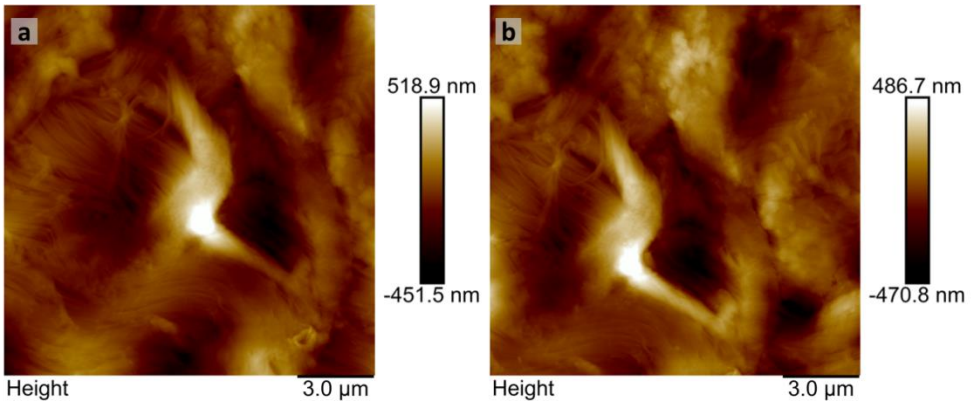

PBS

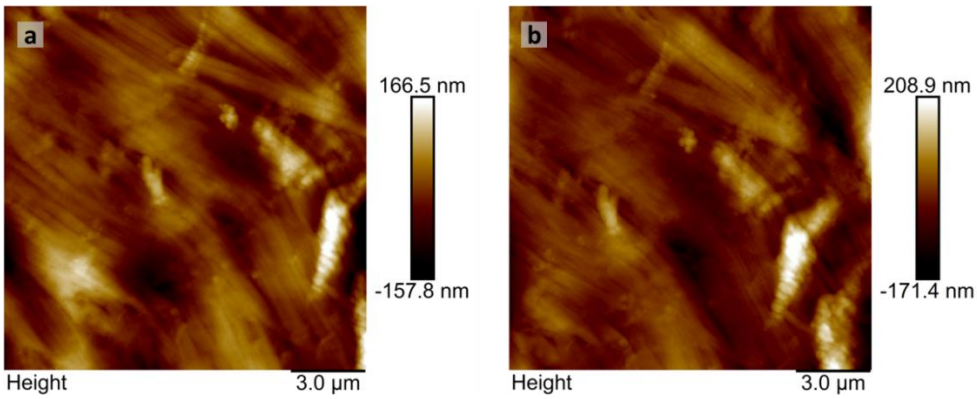

Chondroitinase ABC

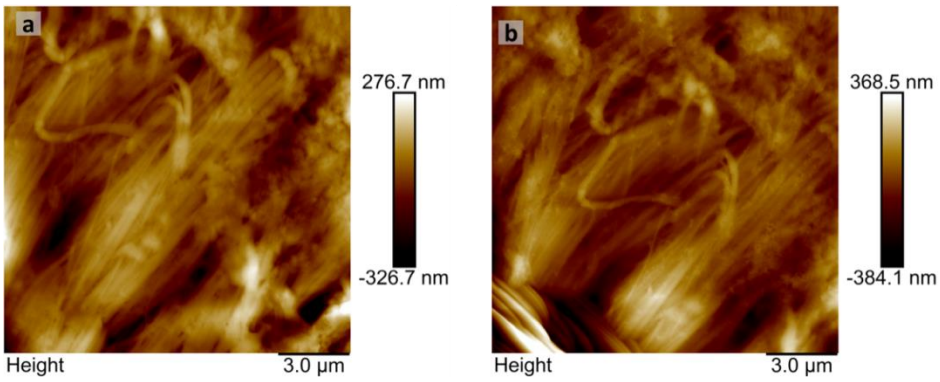

Figure 4.15 Size 15µm images from AFM height channel captured from same locations before (a) and after (b) incubation with distilled water, PBS buffer and chondroitinase ABC.

There were no visible differences in scleral collagen fibrils distribution from 15µm images before and after incubation with distilled water, PBS buffer and chondroitinase ABC in the same location (as shown in figure 4.15).

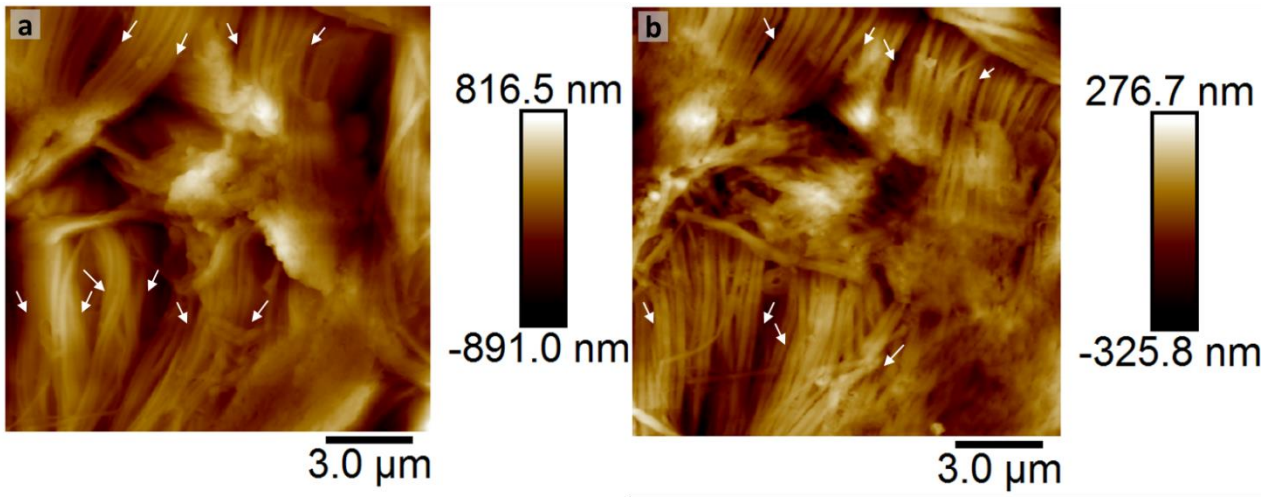

Figure 4. 16 Collagen fibril bundles "split up" after α-amylase treatment. (a) is the 15µm AFM image before incubated with α-amylase and (b) is the image captured from same location on the tissue after incubation. White arrows indicated the locations of same collagen fibril bundles before and after incubation.

The larger (15µm × 15µm) images showed both orientation and distribution of collagen fibrils changed significantly after incubation of α-amylase. As seen in Figure 4.16, in which the collagen fibril bundle can be seen to 'split up' after incubation.

4.4 Discussion and Conclusion

PGs have been observed in small scale AFM images. Figure 4.15 shows the PGs and collagen fibrils interaction in the scleral tissue. Small proteoglycan exist in between the collagen fibrils in and are structurally closely associated with the collagen fibrils. As showed in the image (a) from Figure 4.17, almost all of the interfibrillar PGs in this AFM image connect between collagen fibrils from their gap zone areas. Suspected proteoglycan showed in image (b) is appeared to have similar sizer of big proteoglycan like hyaluronan (Han et al., 2017). (c) is the three-dimensional image that generated from (a) and (b), the collagen-proteoglycan interaction from these image were quite similar to previous observation in the human sclera tissue (Figure 3.2)(Watson and Young, 2004).

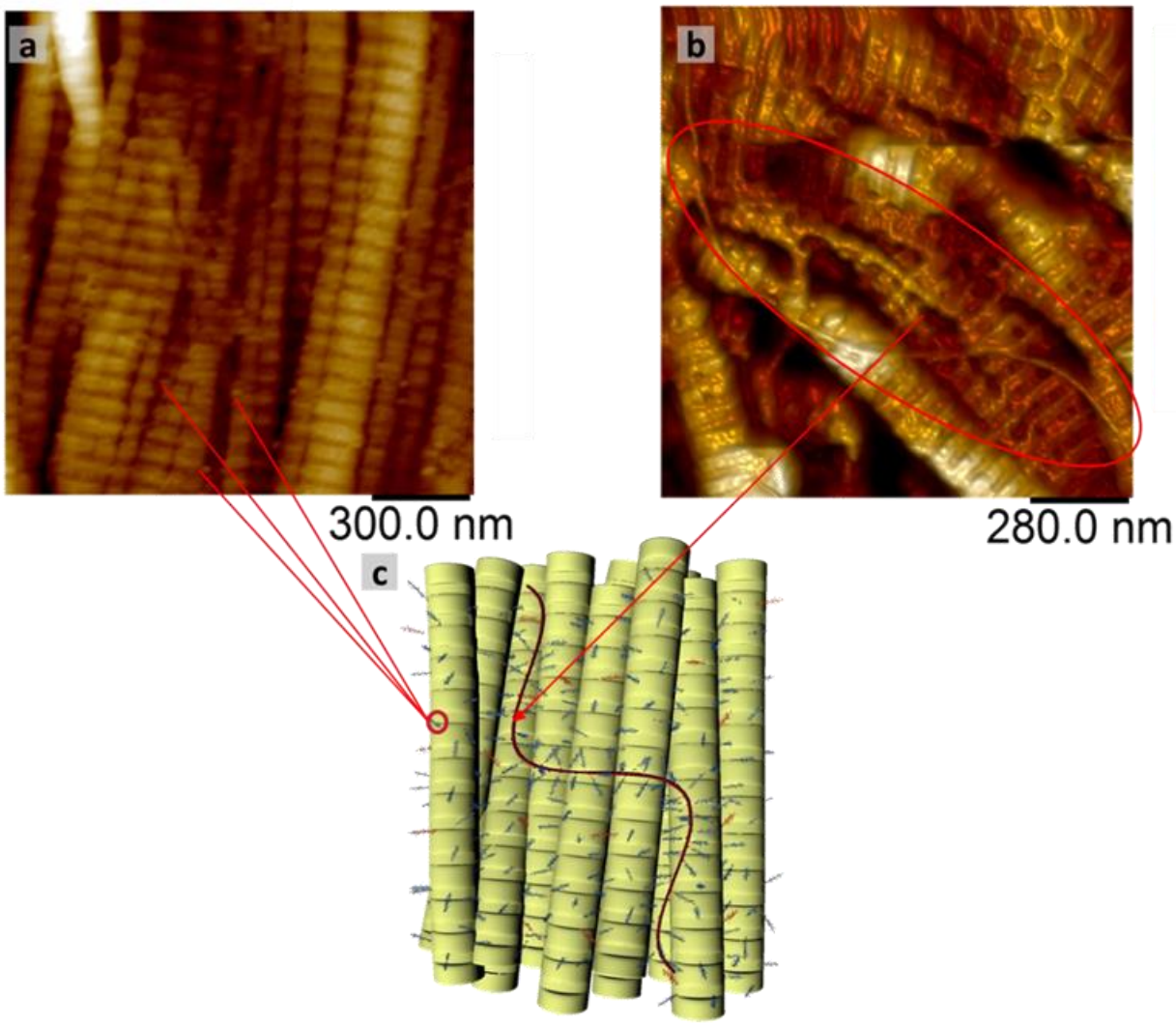

Figure 4.17 3D Schematic (c) of collagen and proteoglycan interaction based on AFM images. The small objects between the collagen fibrils in image (a) are interfibrillar proteoglycan (height channel image). The selected area image (b) shows suspected hyaluronan molecule (height channel image with 3D profiling).

Previously, studies observing transverse section TEM images of collagen fibrils have found that the collagen fibril diameters changed from being abnormally small to very large with irregular contours after proteoglycan depletion (Harper and Summers, 2015b, Robinson et al., 2017, Wang et al., 2015). These forms of changes to collagen structure have also been found in highly myopic eyes (as shown in Figure 4.18).

However, only a few studies have observed the nanostructure of the surface of collagen fibrils in scleral tissue after proteoglycan depletion.

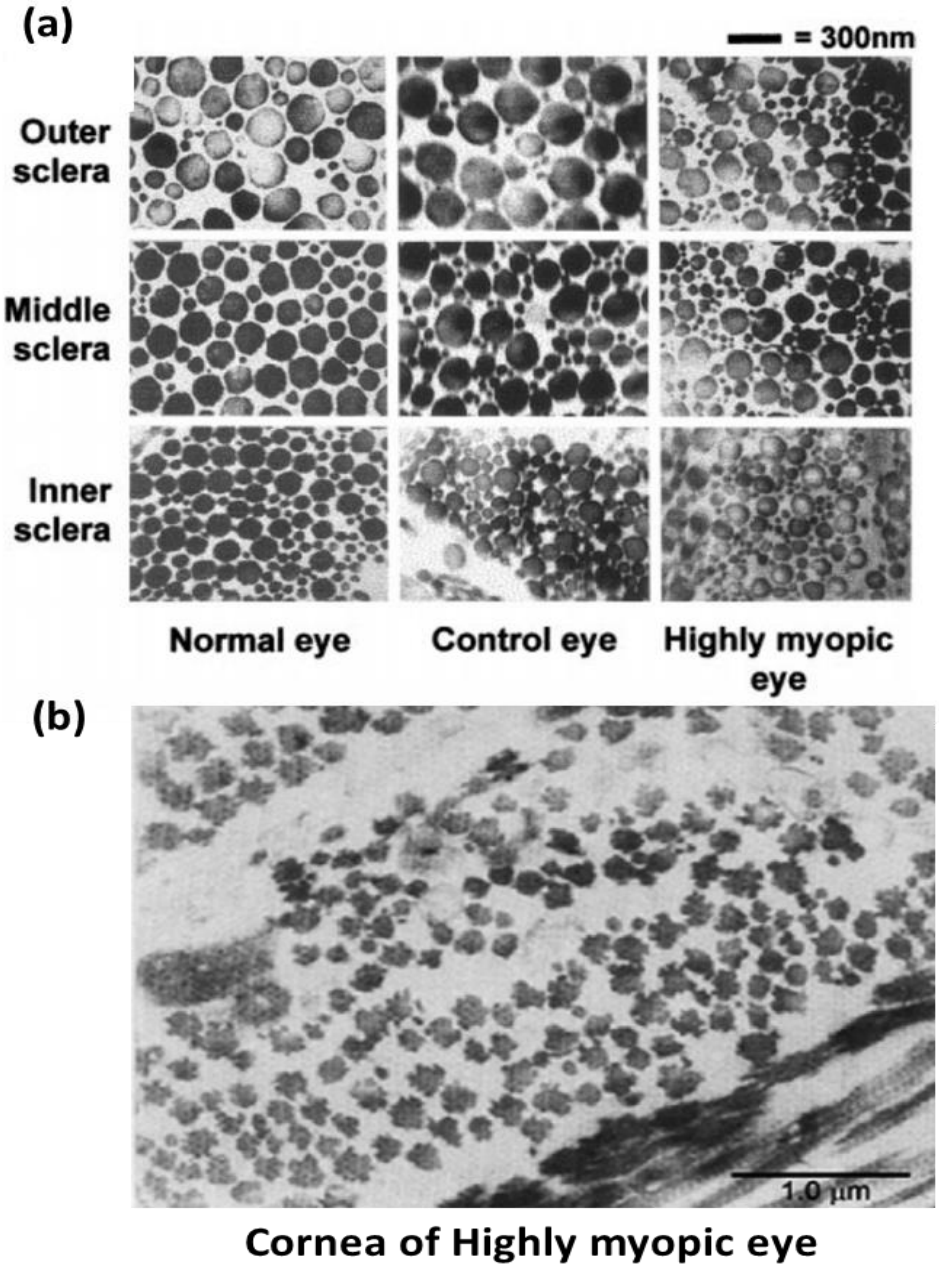

Figure 4.18 Collagen fibrils structures in highly myopic eyes captured by previous studies: (a) Comparison between a normal, control, and highly myopic eye. Collagen fibrils became irregular in size, and abnormally small collagen fibrils are increased in all scleral layers in highly a myopic eye (McBrien et al., 2001). (b)

‘‘Star’’ shape collagen fibrils found in the cornea of a highly myopic eye (Harper and Summers, 2015a).

In this study, collagen fibril ‘fusion’ and ‘splitting up’ have been found in proteoglycan-depleted tissues — both of these reactions to proteoglycan-depletion show how collagen fibrils lose regularity when they lack proteoglycan. The collagen fibril diameters significantly reduced after enzyme incubation, suggesting that an acute loss of proteoglycan will cause a reduction in collagen fibril size. These results have explained why collagen size and shape become irregular in transverse sections of collagen fibrils. They also show how PGs regulate collagen fibril assembly and interactions. Alteration in diameter and diameter range of collagen type I fibrils, abnormal collagen distribution has also been found in the proteoglycan deficient mice from previous study (Ameye and Young, 2002). Results from this study have further demonstrated that rapid absent of proteoglycans will also cause collagen defect.

Type I and III collagens are the only two types of fibrillar collagens found in sclera (Fratzl and Meek, 2008). D-periodicity for both of these two collagen is 67nm (Cameron et al., 2002). Results from this study have shown the D-period in scleral tissue to be between 60 and 70 nm. No statistically significant changes were seen in the incubated tissue, suggesting that the collagen fibrils were not degraded by the proteoglycan depletion.

Previous studies have shown that the collagen gap zone depth provides an indication of the collagen fibril hydration level (Spitzner et al., 2015). Collagen gap zone depth increased after incubation with distilled water and PBS buffer. Collagen diameter

increased after incubation with distilled water and it remained unchanged after incubation with PBS buffer, suggesting that the collagen fibrils swelled in both dimensions after being hydrated with distilled water, but only in height after incubation with PBS buffer. Gap zone depth decreased after treatment with α-amylase and chondroitinase ABC, suggesting that proteoglycan depletion reduced the function of collagen fibril hydration.

This chapter studied the nanostructure of scleral tissue from all three regions and their structural response towards treatment with distilled water, PBS, α-amylase and chondroitinase ABC. Finding relevant to proteoglycan depletion from this chapter will be used to combine with the nano- and micromechanical result from following chapters for better understanding the scleral matrix changes following the proteoglycan depletion. The main findings were:

- Hydration with distilled water results scleral collagen fibril swelling in both diameter and height.
- Unlike distilled water, treatment with PBS buffer leads to swelling only in scleral collagen fibril height.
- Proteoglycan depletion leads to the reduction in collagen fibril size. However it does not change the collagen molecular structure.
- The α-amylase changes the distribution of collagen fibrils, however no change in collagen distribution has been found in scleral tissue after incubation with chondroitinase ABC.

Chapter 5 Mechanical properties mapping following proteoglycan depletion

5.1 Introduction

The sclera's shape changes in diseases like myopia and glaucoma (Summers Rada et al., 2006, Gupta et al., 2013). Studies have suggested that this change is caused by an alteration to its mechanical properties, specifically the posterior pole (Campbell et al., 2014). Glaucoma is the second-leading cause of blindness in the world (Pascolini and Mariotti, 2012) and the damage caused it is considered to be dependent on scleral mechanical properties (Burgoyne et al., 2005). Myopia is a common anomaly of vision in which the light entering the focused area in front the retina is associated with an increased axial length of the eye, involving dramatic changes in scleral mechanical properties (McBrien et al., 2009). It is ubiquitous in certain populations including the Chinese, Japanese and Egyptian and the prevalence of myopia increases every year (Watson and Hazleman, 2012b). A meta-analysis was published in 2016 predicting that in the year 2050, the myopia rate worldwide is expected to be 50% (Lagrèze and Schaeffel, 2017).

Scleral extracellular matrix (ECM) structure changes have been reported in both glaucomatic and myopic eyes. These changes include a variation in GAG content (Knepper et al., 1996, Summers Rada et al., 2006). A decrease in the overall GAG content was found in myopic human eyes (Avetisov et al., 1983a) and a similar decrease in GAG content was measured in tree shrew eyes (McBrien et al., 2000),

monkey eyes (Rada et al., 2000b) and chicken eyes (Rada et al., 1994) with form-deprivation myopia. Changes in the viscoelastic properties of the sclera also occur in glaucomatic and myopic eyes (Jia et al., 2016, Murienne et al., 2016, Coudrillier et al., 2015b, McBrien et al., 2009). PGs play an important role in the structure and mechanical behaviour of collagenous ECM tissues. Proteoglycan closely interacts with collagen fibrils, not only through the binding of the core protein (Raspanti et al., 2008) but also through the electrostatic interaction of GAGs as shown in vitro (Rada et al., 1993). GAGs are highly polar and attract water with their negatively charged carboxyl and sulphated groups. Their fixed-charge density also creates repulsion and attraction forces among themselves and nearby collagen fibrils, resulting in GAG content regulating tissue hydration by determining the number of polar sites for the water binding (Meek, 2008) and tissue osmotic pressure (Scott and Bosworth, 1990).

The mechanical role of GAGs in collagenous tissue has been studied in various tissues by comparing their mechanical behaviour before and after GAG removal. However, the results of these studies are condition and tissue-specific and sometimes conflict (Eckert et al., 2013, Schmidt et al., 1990, Robinson et al., 2017). The mechanical functions of scleral tissues, especially in the posterior scleral region, have also been studied with various techniques (Murienne et al., 2016, Grytz and Siegwart, 2015, Grytz et al., 2014, Papi et al., 2014). However, none of the studies compare the biomechanical function of PGs though all regions of the sclera. In this study, the effects of proteoglycan removal on nano-mechanical behaviour using atomic force microscopy (AFM) in the anterior region to the posterior region of porcine sclerae were investigated in order to infer the mechanical relevance of pathological changes in scleral proteoglycan content.

In an AFM, as shown in figure 5.1, a laser beam deflection system was used. The laser reflected from the back of the AFM lever onto a position-sensitive detector. AFM tips and cantilevers are typically microfabricated from Si or Si_3N_4 with a tip radius ranging from a few to 10s of nm. (Bruker Nano Inc.). The AFM measurement relies on the forces between the tip and scanning sample. These forces impact the generation of AFM images. Forces are not measured directly, but are calculated by measuring the movement and deflection of the tip as the parameters (such as stiffness of the cantilever) are already known.

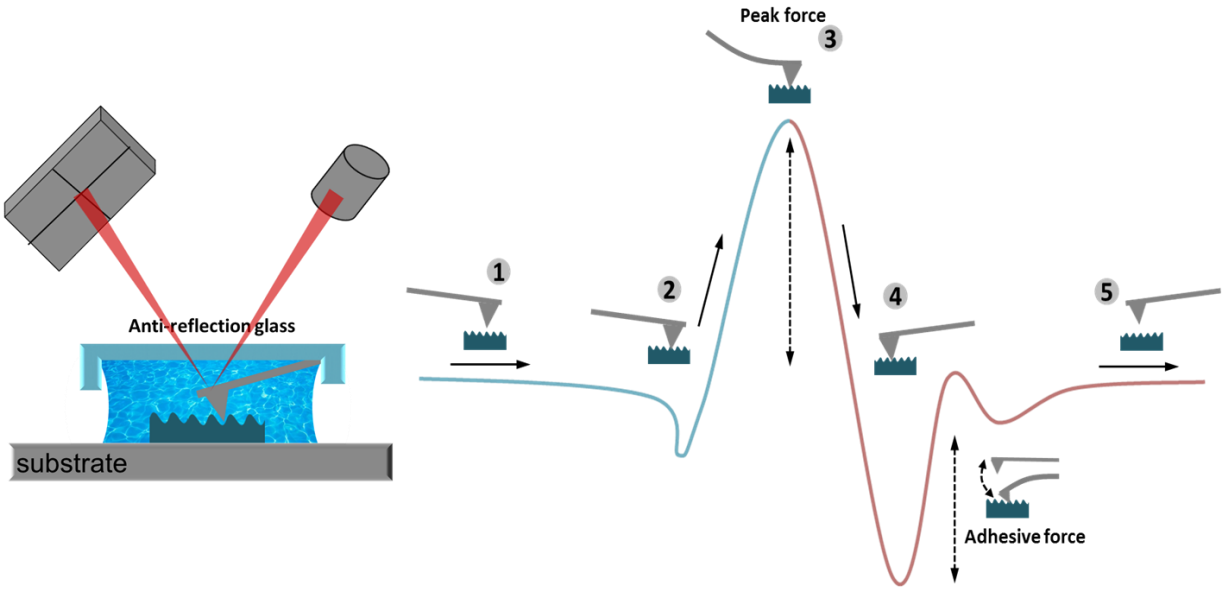

Figure 5. 1. The operating principle of a Bruker multi-mode AFM with peakforce QNM mode scanning sample surface. The force-distance curve at each tapping pixel is defined by: surface approach (1–2), point of deepest indentation (3), force release and surface restoration (4) and released cantilever (5).

Peakforce quantitative nanomechanical mapping (QNM) mode was used for this study. This is an AFM mode that is suitable for biological sampling with structural

heterogeneity (Pittenger et al., 2010b) . Compared to other AFM modes such as contact mode and tapping mode, Peakforce QNM performs a very fast force curve at every pixel in the image rather than calculating a time-average force during sample imaging (force curves and the information obtained are shown in figure 5.2). In probe scanning techniques with normal scan force, there are two main causes of tip and sample damage. Any lateral force that tips exertion on a sample will cause the sample to tear, and likewise, lateral force from a hard sample will also cause tip damage (Pittenger, Erina & Su 2010). Peakforce QNM controls the maximum force (peakforce), and this allows the detection of quantitative nanomechanical data directly from the sample, while the tip-sample contact area is minimized without sample or tip damage.

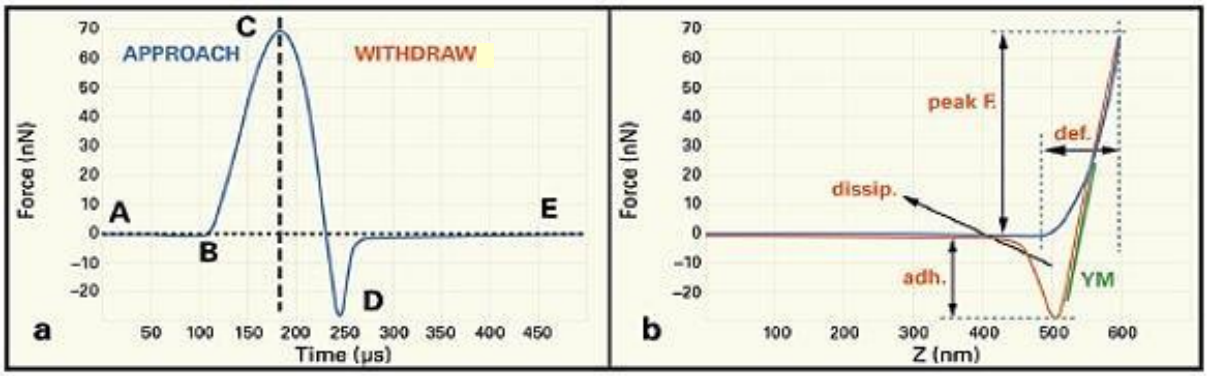

Figure 5. 2 (a) Plot of force and Z position as a function of time (b). A force curve eliminates the time variable, plotting Force vs. Z position. Edited from Veeco Instruments Inc. (2010)

Unlike traditional AFM modes, Peakforce QNM mode can operate with a wide variety of standard AFM probes. It provides images at a relatively high speed and a high resolution. In PeakForce Tapping the probe is oscillated at a suggestion

frequency of 1~2 kHz with peak-to-peak amplitudes of 150~300 nm. Figure 5.2a represents the measured force on the probe during approach of the tip and the retraction. When the tip is at a distance from the surface (point A) there is little or no force on the tip. As it is approaching to the surface the cantilever is pulled down by attractive forces such as van der Waals, electrostatics or capillary forces. At point B the tip touches the surface and stays on the surface until the Z position reaches its lowest position (point C) while the force is increasing. The PeakForce arises at point C. The probe starts to withdraw and the force decreases until its minimum at point D. The adhesion is determined by the force at that point. The tip leaves the surface and only long-range forces affect the tip. When the tip-sample separation is at its maximum (point E) there is a very small or zero force. A constant force at point C is maintained by adjusting the extension of Z piezo through the feedback loop. Dependence of the force against the Z-position can be compared with force-displacement curves that have usually been used in measuring mechanical properties of a sample. This method is faster than nanoindentation where an approach-retract cycle is performed at rate of 0.5 to 10 Hz (Sweers et al., 2011). Figure 2b illustrates the information which can be obtained. The most commonly used characteristics are elastic modulus, adhesion, energy dissipation and maximum deformation. When the force curve is complete it is then analysed to obtain the properties of the sample and the information is sent to one of the image data channel. (Malohlava et al., 2012)

In peakforce QNM, the reduced Young's modulus can be obtained in the Derjagin, Muller, Toropov (DMT) channel (see equation 4.1). This modulus is ideal for the biological tissue with non-negligible adhesion force in the contact area(Bouchonville

et al., 2016). The adhesive force between the tip and sample surface has been considered in the DMT model, the reduced Young's modulus E_r is given by:

$$E_r = \frac{3(F_{tip} - F_{adh})}{4\sqrt{Rd^3}} \quad (5.1)$$

Here, the F_{tip} is the force on the tip, F_{adh} is the adhesive force between tip and sample surface, R is the AFM tip radius, and *d* is the deformation depth.(Young et al. 2011). If the Poisson's ratio is known, the sample's Young's modulus E_s can be calculated using Equation 5.1:

$$E_r = \left[\frac{1-v_s^2}{E_s} + \frac{1-v_{tip}^2}{E_{tip}}\right]^{-1} \quad (5.2)$$

v_s and v_{tip} refer to the Poisson's ratios of the sample and the tip. The sample's Poisson's ratios must be entered by the user into the system cantilever parameter.

Previous study on compressive properties of human sclera tissue has measured that human sclera Poisson's ratio is from 0.46~ 0.50 (Battaglioli and Kamm, 1984). The reduced Young's modulus could be used for a material with unknown Poisson's ratio.

5.2 Method

5.2.1 Sample preparation

Scleral tissues were collected from the same eyes within chapter 4, cleaned of skin, fat, adherent muscle, retina and choroid then dissected into the anterior, equatorial and posterior regions. Blocks with size 4 mm^2 were taken from each region with a double blade cutting tool, from the locations as shown in figure 5.3. The dissected

tissue was then embedded in optimal cutting Temperature (OCT) resin (Tissue-Tek, CellPath, Powys, UK) and snap frozen with isopentane and liquid nitrogen for cryosectioning. Specimens were continuously sectioned vertically with a Leica CM1850 cryostat (Leica Microsystems (UK) Ltd, Milton Keynes) and numbered sequentially to make sure each testing point was approximately 5μm (specimen thickness) apart (figure 5.3). Specimen locations and thickness were decided according to previous studies on sclerae using AFM (Papi et al., 2014). All sectioned specimens were stored in -80^{O}C freezer until testing.

5.2.2 Incubation buffers

Sclera samples (three samples from each region from each eye, n=108) were tested in four solutions: 2mg/ml Amylase in water, chondroitinase ABC for proteoglycan depletion testing and 100% ultra clean distilled water. 100% PBS solution (pH7.4) was the control group for monitoring the effect of rehydration on scleral tissue.

5.2.3 AFM Peakforce QNM in liquid

Experiments were performed using a Bruker MultiMode 8 AFM and SCANASYST-FLUID (Bruker Nano Inc., Nano Surfaces Division, Santa Barbara, CA). The probes (see table 5.1) were selected based on previous experiments on scleral tissue (Papi et al., 2014) and the recommendations of Bruker AXS to investigate a range of polymer Young's moduli. (5-500MPa—values based on IIT measurements)

Table 5. 3 Information for the cantilever and tip used in this study (Bruker Nano Inc.)

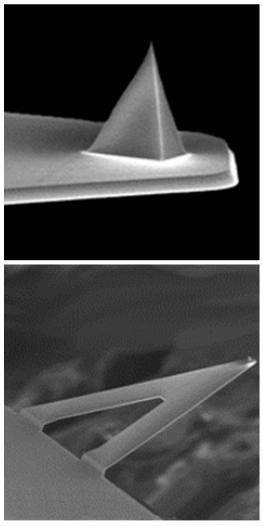

Tip Reference	TSCANASYST-FLUID
Cantilever Geometry:	Triangular
Tip Height (h):	2.5 - 8.0µm
Spring constant (N/m)	0.7
Tip Radius (Nom):	20 nm
Tip Radius (Max):	60 nm
Material:	Silicon Nitride
Cantilever Back Side Coating:	Reflective Gold

Calibration method

The relative calibration method was used in the experiment in deflection sensitivity, spring constant and tip radius. Deflection sensitivity and spring constant were calibrated by ramp on a clean glass coverslip. The spring constant was measured with a NanoScope thermal tune function. Tip radius and PeakForce Setpoint were calibrated using a calibration sample Polydimethylsiloxane (PDMS) with modulus of elasticity = 5.1±0.1MPa. To make the measured modulus equal to the known value of the reference sample, these two parameters were calibrated again after each testing to make sure the measured results were accurate. PeakoForce set point was settle to a constant value (0.05V), tip radius was not changed after each groups of testing (Typical tip radius from 18nm to 35nm).

Mechanical testing

Each sample was tested individually at room temperature (22^{o}C). Before testing, OCT was washed off with distilled water.

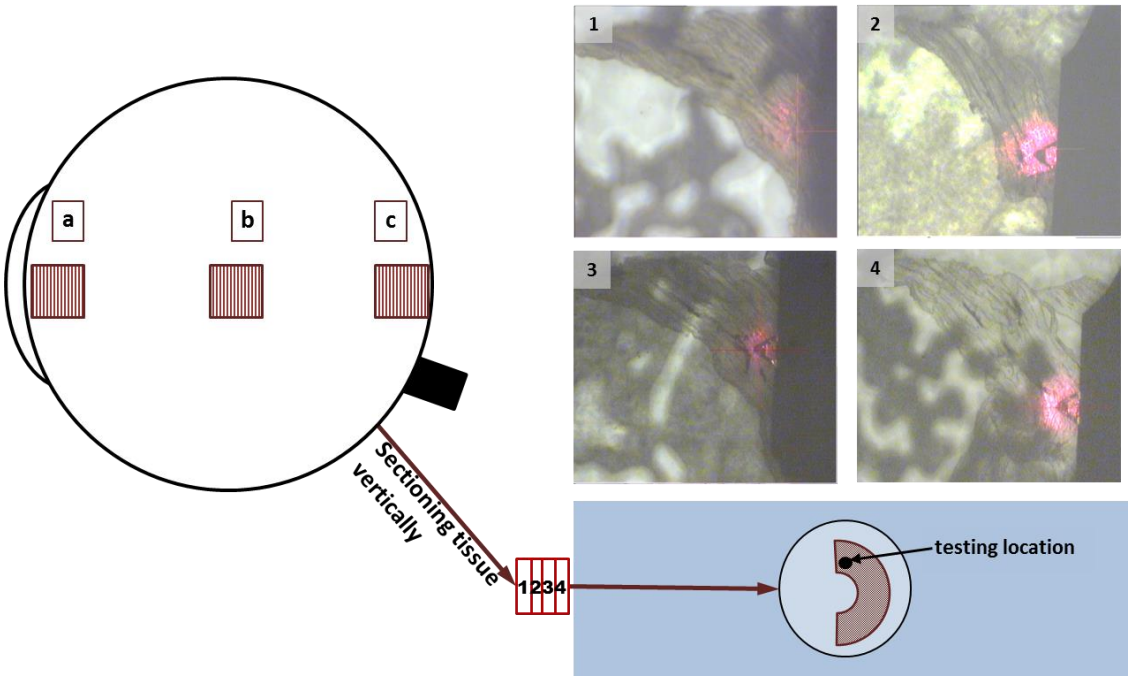

Figure 5.3 Schematic diagram of the porcine eye globe (left) showing the anterior (A), equatorial (E) and posterior (p) regions from where the tissue was dissected. Tissue was sectioned vertically and numbered sequentially; probe location images captured in this figure show that same location of the specimen (upper inner corner) was selected as the testing location for one repeat of samples for four groups.

During testing, locations with a scanning size of 7µm^2 (where the scanning coordinates are X-Offset=0, Y-Offset=0 and scan angle=0) were selected by using scleral tissue's natural curve shape. Five locations with size 1.4µm^2 found from 7µm^2 images were captured for elastic measurement, and the coordinates of these locations was recorded. After five locations were captured, the sample was kept at AFM scanning stage for buffer treatment. Allsamples were incubated with a 0.04ml buffer for 40 minutes and washed with 100% ultra clean distilled water at least three times. After incubation, the same locations with the same scan sizes were found by using recorded coordinates and measured for comparison. Once one repeat of samples

from four groups was measured, the reference sample was tested again to ensure the results were accurate.

5.2.4 Data analysis and statistics

Mechanical property results were analysed by using OriginPro9 (OriginLab, Northampton, MA) and expressed as mean ± standard mean error. Intra-group homogeneity was studied via the Kruskal-Wallis ANOVA test to determine if there were significant variations between measurements of samples mechanical properties within each treatment group. Following this, group differences were assessed via suitable 2-sample independent tests selected after appraisal of data normality and homoscedasticity. The statistical significance of mechanical properties between incubation pre and post-treatment were evaluated with one way ANOVA. (If a p-value is less than 0.05, it is flagged with one star (*). If a p-value is less than 0.01, it is flagged with two stars (**). If a p-value is less than 0.001, it is flagged with three stars (***). If a p-value is less than 0.0001, it is flagged with four stars (****))

5.3 Results

The Kruskal-Wallis ANOVA testing was performed for each group to make sure there is no measurement within in one incubation group was skewing the data. The test confirmed that there were no significant difference between samples in the same incubation group (Kruskal-Wallis ANOVA, $p>0.05$). The mechanical results were compared between specimens measured in the same location, pre and post-treatment.

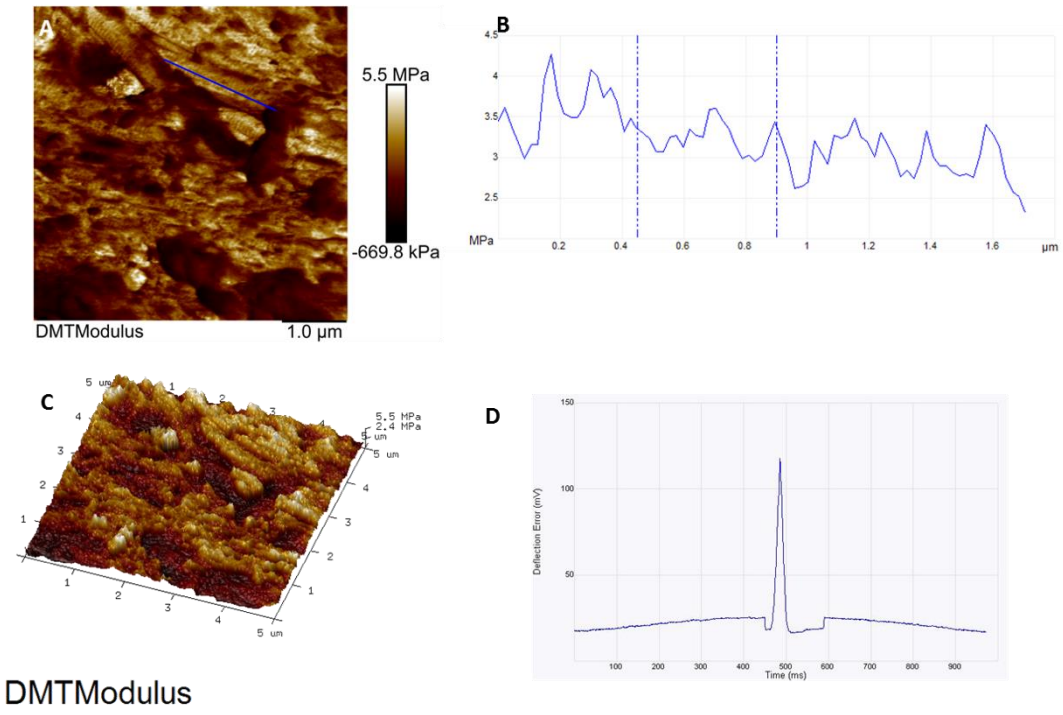

Figure 5.4 AFM PeakForce QNM image with size 7µm^2 from 2D (A) and 3D (C) DMT Modulus channel and modulus plot from a selected collagen fibril (B).(D) is a typical deformation curve for the tissue.

Surface DMT modulus from scanning image (figure 5.4) shows the mechanical properties of collagen fibrils are significantly higher than the extrafibrillar matrix between two fibrils. For a single collagen fibril, the mechanical properties of gap-zone are significantly lower than the overlap zone. This result is consistent with a previous study(Grant et al., 2008).

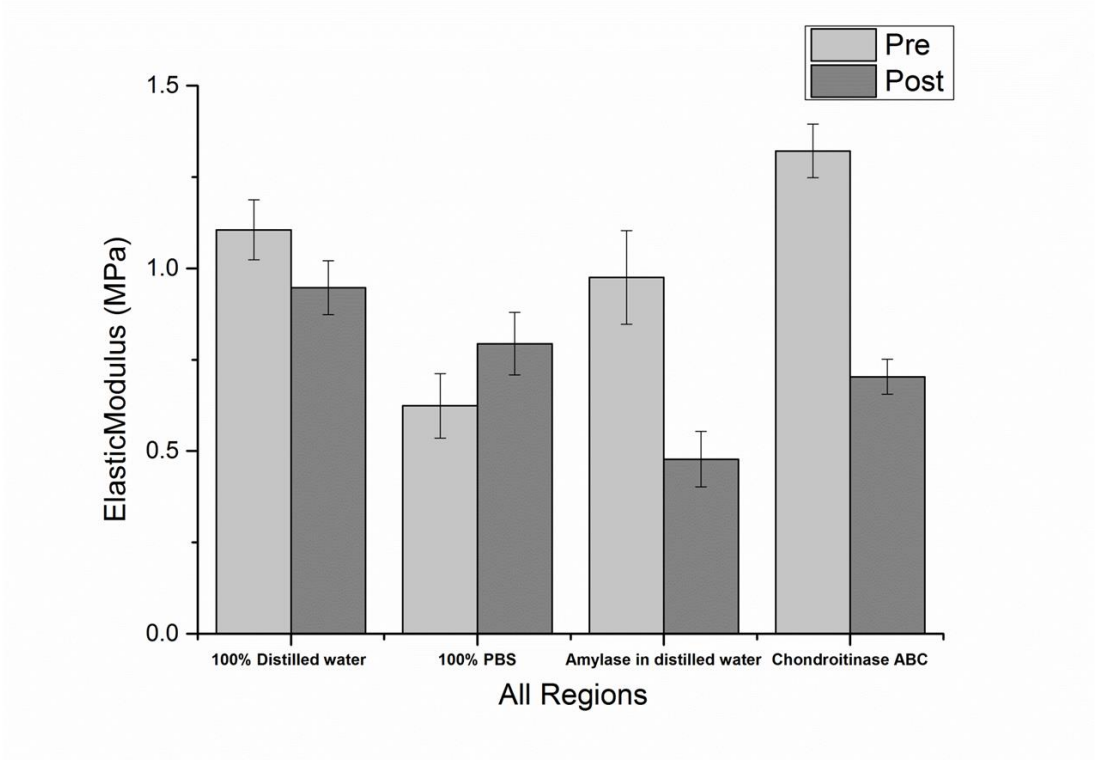

Figure 5. 5 Elastic modulus changes following buffer treatment in all scleral regions (n= 900 images/group, 450 pre and 450 post-treatment).

For the overall results (Figure 5.5), the elastic modulus reduced after incubation with α-amylase and chondroitinase ABC. There was no statistically significant change after incubation with ultra clean distilled water.

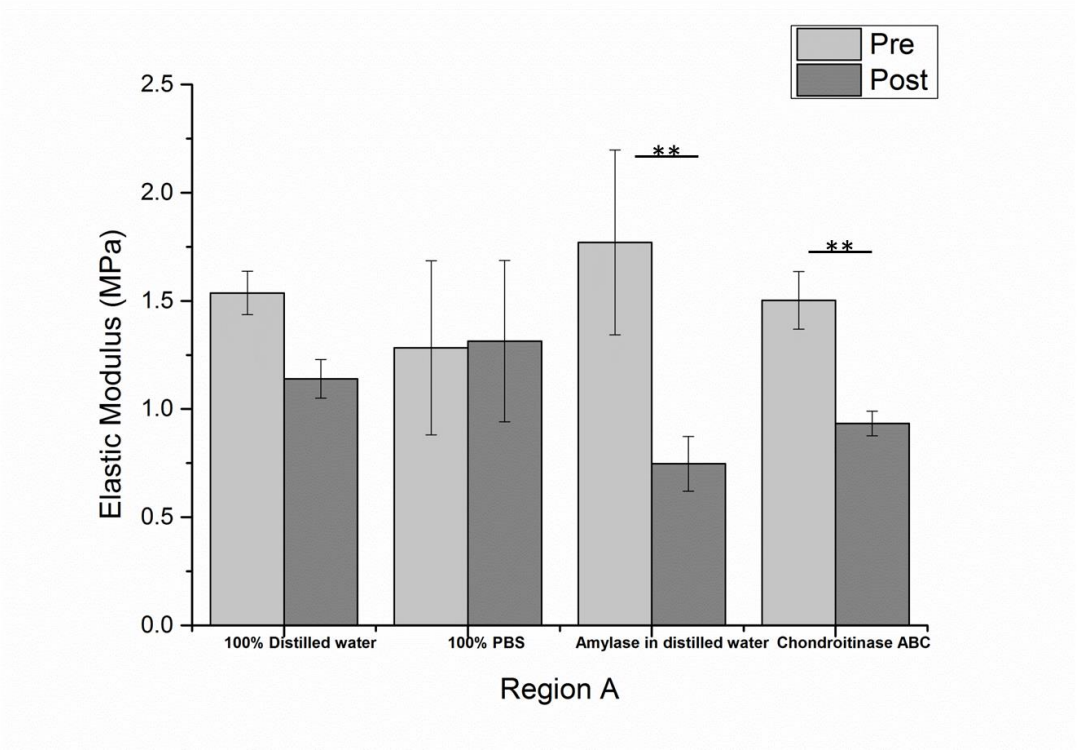

Figure 5. 6 Elastic modulus result following four treatments in anterior scleral regions (n= 300 images/group, 150 pre and 150 post-treatment).

For the results in the anterior region (Figure 5.6), the elastic modulus reduced after incubation with α-amylase and chondroitinase ABC. There was no statistically significant difference after incubation with ultra clean distilled water and PBS solution.

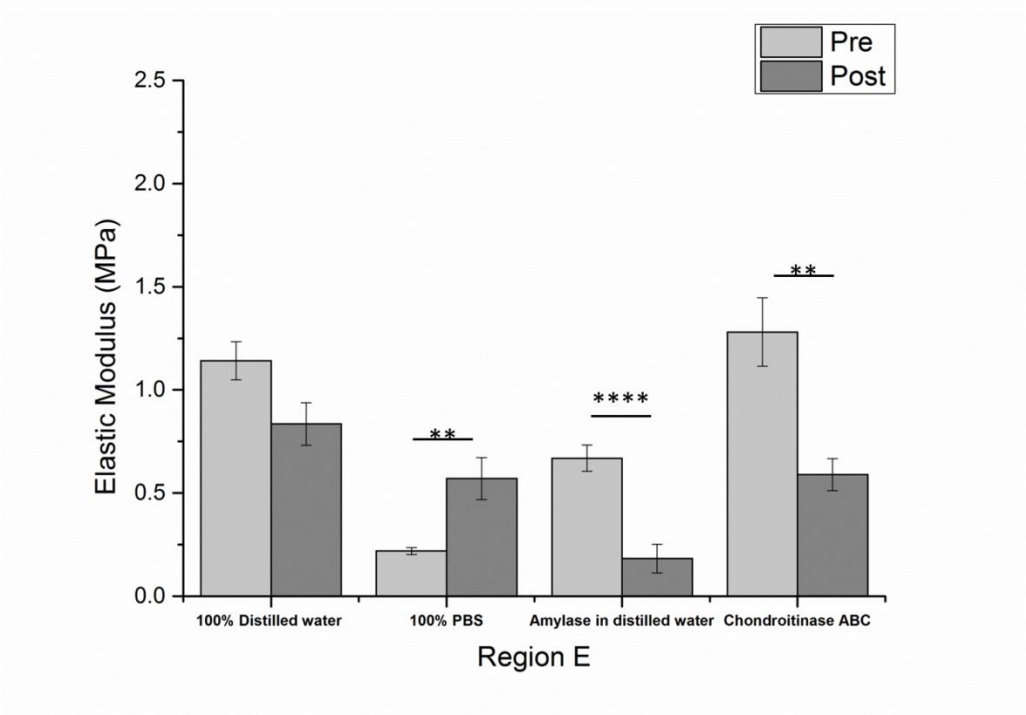

Figure 5. 7 Elastic modulus result following four treatments in scleral equatorial regions (n= 300 images/group, 150 pre and 150 post-treatment).

For the result in the equatorial region (Figure 5.7), the elastic modulus reduced after incubation with α-amylase and chondroitinase ABC There was no statistically significant difference after incubation with ultra clean distilled water, however a significant increase of elastic modulus was found in the specimen incubated with PBS solution..

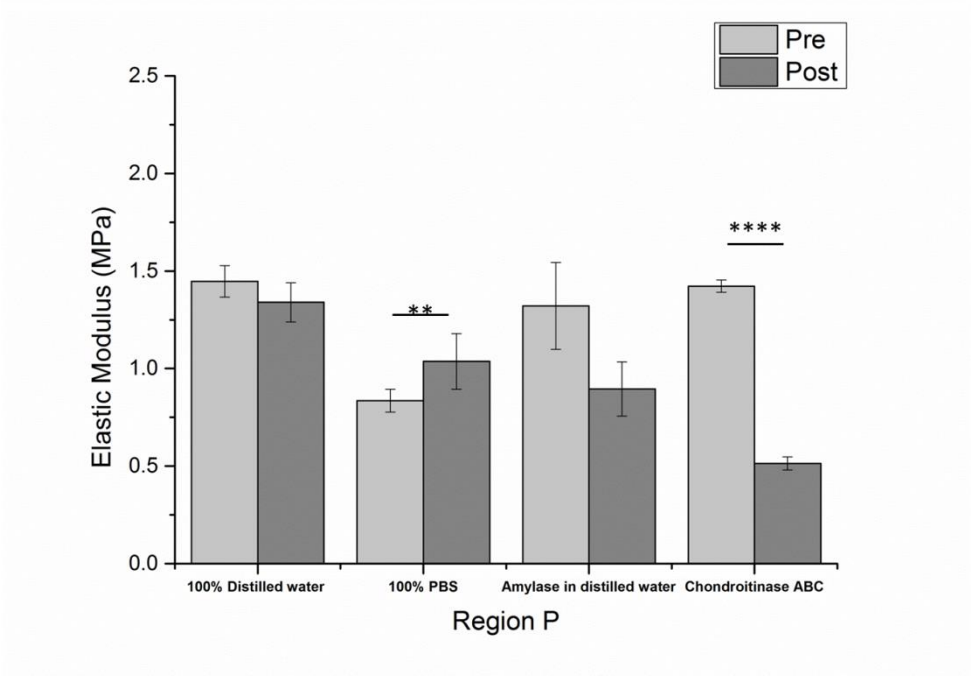

Figure 5. 8 Elastic modulus changes following buffer treatment in posterior scleral regions (n= 300 images/group, 150 pre and 150 post-treatment).

In the anterior region (Figure 5.8), the elastic modulus reduced after incubation with chondroitinase ABC however not with α-amylase. There was no statistically significant difference after incubation with ultra clean distilled water. An increase of the elastic modulus was found in specimens incubated with PBS solution.

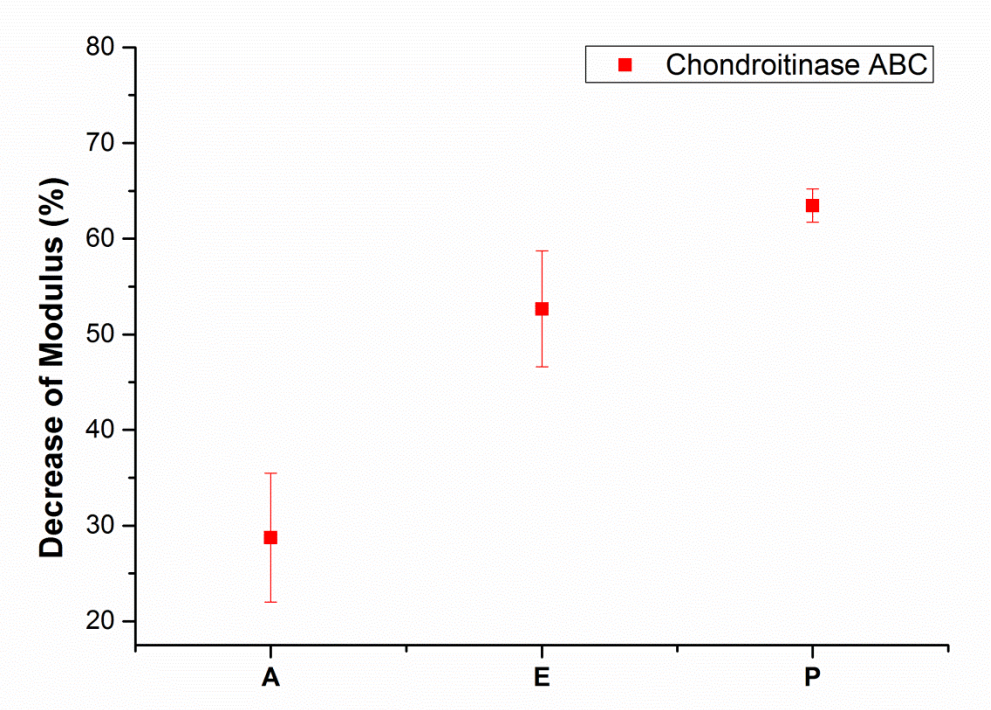

Figure 5. 9 Decrease of elastic modulus in all three regions after being incubated with chondroitinase ABC.

The elastic modulus was reduced in all three scleral regions after being incubated with chondroitinase ABC (Figure 5.9). However, these reductions were not constant through the three regions of sclera. The elastic modulus reduced by 37.87% ± 6.73 in the anterior region, 54.01% ± 6.06 in the equatorial region and 63.92% ± 1.46 in the posterior region.

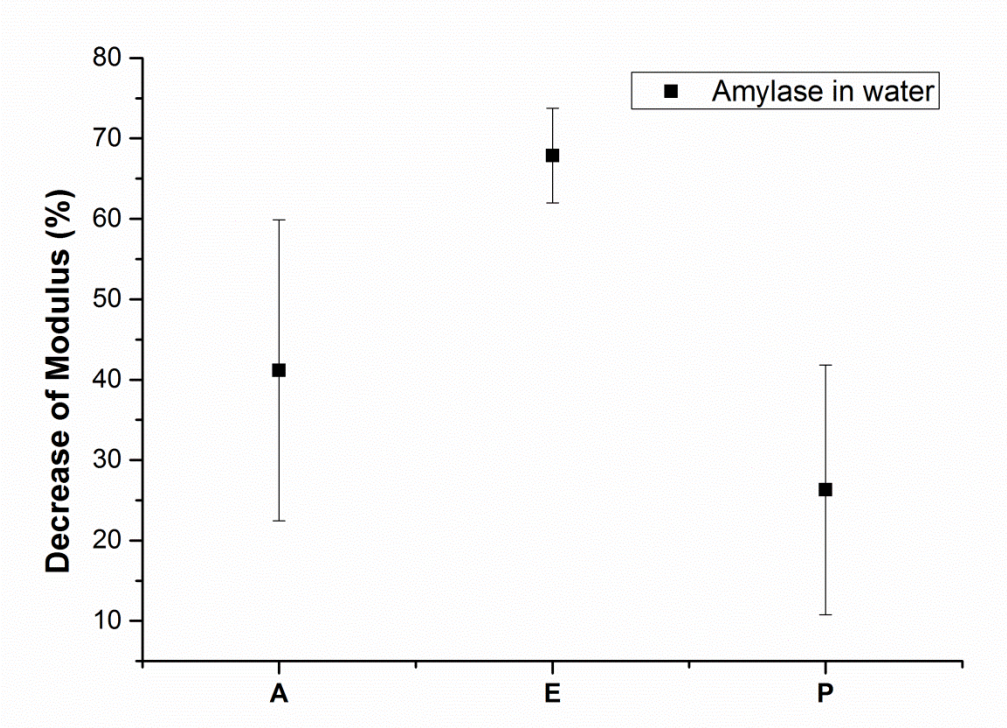

Figure 5. 10 Decrease of elastic modulus in all three regions after being incubated with α-amylase.

The elastic modulus was reduced in all three scleral regions after being incubated with α-amylase in distilled water (Figure 5.10). However, these reductions were not constant across the three regions of sclera. The elastic modulus reduced 57.80% ± 18.74 in the anterior region, 72.73% ± 5.89 in the equatorial region and 32.26% ± 8.92 in the posterior region.

Table 5. 4 Comparison of mechanical outcome, expressed as a mean value with the standard error of mean, p-value and difference in percentage between pre and post-buffer treatment.

Regions	Treatment	Pre mean ±SE (MPa)	Post mean ± SE (MPa)	P value	Difference ± SE (%)
Anterior Region	100% Distilled water	1.54±0.10	1.14±0.09	>0.05	-
	100% PBS	1.28±0.40	1.31±0.37	>0.05	-
	Amylase in distilled water	1.77±0.43	0.75±0.13	0.020	-57.80±18.74
	Chondroitinase ABC	1.50±0.13	0.93±0.06	0.005	-37.87±6.73
Equatorial Region	100% Distilled water	1.14±0.09	0.84±0.10	>0.05	-
	100% PBS	0.22±0.01	0.45±0.10	0.004	118.61±45.70
	Amylase in distilled water	0.66±0.06	0.18±0.07	0.000	-72.73±5.89
	Chondroitinase ABC	1.28±0.17	0.59±0.08	0.003	-54.00±6.06
Posterior Region	100% Distilled water	1.45±0.08	1.34±0.10	>0.05	-
	100% PBS	0.84±0.06	1.04±0.14	0.003	24.14±13.77
	Amylase in distilled water	1.32±0.22	0.90±0.14	>0.05	-32.26±8.92
	Chondroitinase ABC	1.42±0.03	0.51±0.03	0.000	-63.92±1.46
All Regions	100% Distilled water	1.11±0.08	0.95±0.07	>0.05	-
	100% PBS	0.62±0.09	0.79±0.09	>0.05	27.32±16.39
	Amylase in distilled water	0.98±0.13	0.48±0.08	0.001	-51.03±6.74
	Chondroitinase ABC	1.32±0.07	0.70±0.05	0.000	-46.75±4.86

5.4 Discussion and Conclusion

5.4.1 Scleral nanomechanical change following hydration with distilled water and PBS buffer

The elastic modulus stayed unchanged in the anterior, equatorial region after being incubated with PBS buffer (pH7.4, NaCI 137mmol/L). However, there was a increase in the posterior region and the overall scleral elastic modulus. A similar increase of mechanical properties was found in single collagen fibril treated with a high concentration water-based salt solution in a previous study (Figure 5.11) (Grant et al., 2009).

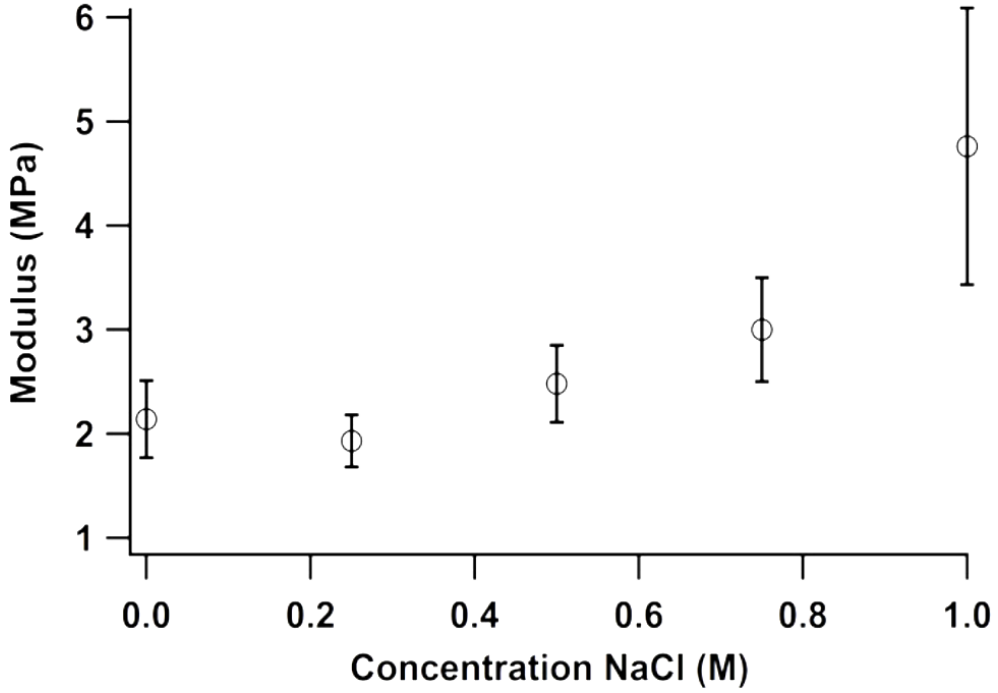

Figure 5. 11 Increase of the elastic modulus of collagen fibrils as a function of NaCl concentration. (Grant et al., 2009)

Previous studies on hydrated human corneal stroma indicate that the elasticity modulus of collagen decreases while the hydration level increases (Xia et al. 2014). Other studies have shown that a drop in the elastic modulus of two or three orders of magnitude will be led by water penetrating the collagen fibril structure (Grant et al. 2008, van der Rijt, Joost A. J. et al. 2006, Yang et al. 2008). In this study, the mean value of the elastic modulus decreased in all three regions after hydration with distilled water (25.84% in the anterior region, 26.83% in the equatorial region and 7.43 in the posterior region). However no statistical difference was found.

5.4.2 Scleral nanomechanical change following enzyme treatment

Chondroitinase ABC and α-amylase are the two main enzymes used in previous studies into collagenous tissue and mechanical properties following proteoglycan depletion (Watanabe et al., 1997, Wollensak et al., 2011, Murienne et al., 2016, Murienne et al., 2015). In these two enzymes, chondroitinase ABC is a well-studied enzyme that specifically degrades chondroitin and dermatan sulphate. Although the possible effects of α-amylase on proteoglycan have been pointed out by previous studies (Quintarelli et al., 1969), none of these studies have researched the specific effects of α-amylase on proteoglycan. It is important to study the effect of α-amylase on eye tissue because the concentration of amylase is enhanced in keratoconus patients (Spoerl et al., 2012). In addition, α-amylase is one of the enzymes that exists in tear fluid and makes continuous contact with the eye (Van Haeringen et al., 1975).

As seen in this study, elastic modulus decreases in all regions after being incubated with both enzymes. However, the reduction of two enzymes was different across the three scleral regions. The elastic modulus reduced most in the posterior region and least in anterior region after being incubated with Chondroitinase ABC, which shows a similar distribution of chondroitin and dermatan sulphate and proteoglycan measurement result in chapter 2. The α-amylase shows different effects in distribution of sclera. The elastic modulus reduced most in equatorial region (instead of anterior region) and least in the posterior region, this result is not constant with proteoglycan measurement result in chapter 2. this difference indicated that α-amylase may has effect on other components from sclera matrix that exceeded the measurement range in chapter 2 that contribute to the tissue nanomechanical properties. The standard error of mean of reductions in the mechanical modulus after

α-amylase incubation was greater than chondroitinase ABC, showing that the effect of α-amylase on scleral tissue is less stable than the effect of chondroitinase ABC. However, the change in samples treated with chondroitinase ABC was more significant than those treated with α-amylase shows chondroitinase ABC has more effect in nano-level elastic modulus.

This chapter studied the nanomechanical properties scleral tissue from different regions and their mechanical response towards treatment with distilled water, PBS, α-amylase and chondroitinase ABC. Finding relevant to proteoglycan depletion from this chapter will be used to combine with the micromechanical result from next chapter for better understanding the scleral mechanical changes following the proteoglycan depletion. The main findings were:

- Nanomechanical properties decreased in all three scleral regions after hydration with distilled water.
- Treatment with PBS has caused an increase of regional average nanomechanical in the sclera.
- Proteoglycan depletion will leads to significant reduction of scleral nanomechanical properties.
- There were significant regional differences in the reduction caused by α-Amylase and chondroitinase ABC. This indicated that different type of proteoglycan has different contribution towards scleral nano-mechanical properties.

Chapter 6: Mapping mechanical properties at a microscale following proteoglycan depletion by nanoindentation.

6.1 Introduction

Biological tissues like the sclera have a multiscale organisation (Figure 6.1). The aim of this chapter is to measure the scleral mechanical properties at a larger scale. Unlike the previous chapter, this chapter studies the mechanical properties of the tissue matrix instead of only that of collagen fibrils. Proteoglycan depletion with α-amylase and chondroitinase ABC was also carried out in this chapter to determine the change in the mechanical properties of tissue matrix following proteoglycan depletion.

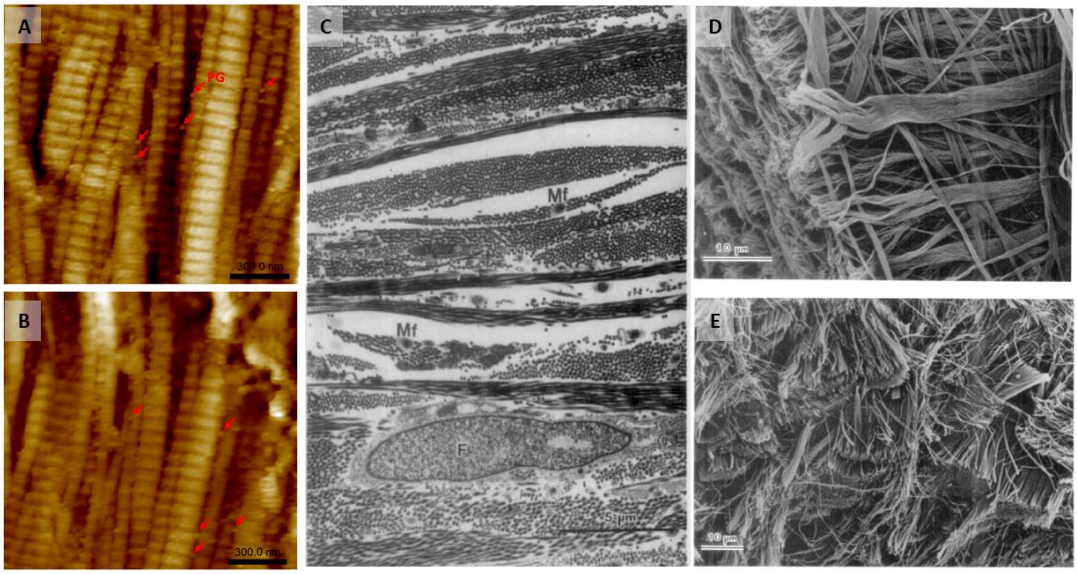

Figure 6.1. Scleral collagen fibrils and tissue matrix structure at the nanometer and micrometre scale observed by AFM and TEM. PG= Proteoglycan; F= Fibroblast; Mf=Micro fibril (Komai and Ushikif, 2015).

Biological tissues differ greatly in their structure and composition and have complex hierarchical structures with elements interacting across length-scales (Akhtar et al., 2011, Meyers et al., 2008). In the sclera, collagen fibrils are organised into irregularly arranged and interwoven lamellae (Figure 6.1). This organisation of collagen lamellae is similar to the collagen arrangement of the cornea, but scleral collagen fibrils are highly variable in their diameter and the lamellae vary in thickness. The orientation of each lamella is irregular with respect to neighbouring lamellae. Scleral fibroblasts are located between collagenous lamellae and are exclusively responsible for the synthesis of the scleral extracellular matrix. Based on studies in the cornea (Birk and Trelstad, 1984), it is likely that the outer edges of each lamella, which are adjacent to the scleral fibroblasts, contain the most immature collagen fibrils relative to those in the centres of each collagenous lamellae.

Nanoindentation is an ideal method for mapping the local mechanical properties for inhomogeneous biological materials like sclera in micrometre scale. However, methods to keep tissue hydrated during testing need to be developed (Ebenstein and Pruitt, 2004). Traditionally, this technique has been used to determine the elastic behaviour of hard materials. These materials for nanoindentation tests are often embedded in a resin to facilitate sample handling and surface polishing. However, for biological tissue like the sclera, samples are mostly required to be in a hydrated condition during testing. For a short time period of indentation, tissue samples can be submerged prior to testing and removed from the fluid just before indentation. Testing a sample fully submerged in a fluid cell is one option that has been used for

hydrated testing of tissues, but data acquisition and analysis are complicated by meniscus forces acting on the shaft of the indenter tip; specialised tips with long shafts are therefore required. Other solutions include hydrating samples from the edges using gauze, foam (Ebenstein, Pruitt 2004), a specialised mounting stage (Selby et al. 2014), or applying several drops of fluid to the surface prior to indentation.

Conventional quasi-static nanoindentation of soft tissues is challenging due to the high surface roughness, high compliance and associated issues with surface detection. The work presented in this chapter utilises an oscillatory nanoindentation method which exploits the dynamic capabilities of nanoindentation systems and allows the shear storage and shear loss modulus of the sample to be determined (Akhtar et al., 2018). This approach has been applied to test soft tissues including cartilage (Peters et al., 2017) and skin (Moronkeji et al., 2016). This chapter aims to utilise this method, with a 100 μm flat punch indentation tip to determine the micromechanical properties of the sclera tissue following enzymatic degradation.

Nayar et al have investigated the mechanical properties of porcine sclera only (2011) and sclera with choroid and retina (2012) by using nanoindentation (DMA mode, 80μm diameter, flat-punch). Both studies reported that the elastic modulus of sclera was around 30kPa. However the stiffness of inflated porcine sclera was reported to be significantly higher (0.20 ± 0.04 MPa at 15 mm Hg) in a study by Leung et al. (2014) (Universal testing machine, 5mm diameter, flat-punch). This variation might cause by difference testing instrument, testing environment, testing location and tissue hydration condition. In this chapter porcine sclera tissue from all three regions

were measured with instrument nanoindentation within the same environment, using the same enzymes as used in the previous chapters, to have a comparable microscale result and thereby better understand sclera matrix mechanical properties and the changes following enzyme degradation

6.2 Methods

6.2.1 Sample preparation and nanoindentation testing

Scleral tissues were collected from the same eyes within chapter 4, then cleaned of skin, fat, adherent muscle, retina, and choroid, and was then dissected into anterior, equatorial, and posterior regions. Three 4 mm^2 blocks (with thickness ≈ 1mm) were taken from each region using a double-blade cutting tool. Samples were divided into four groups (control, α-amylase and control, chondroitinase ABC) and incubated for 4 hours in room temperature. A flat-ended cylindrical punch (Synton-MDP Ltd, Nidau, Switzerland) with 100 μm diameter radius was mounted on and then underwent dynamic nanoindentation (G200 Nanoindenter, Keysight Technologies, Chandler, AZ, USA) equipped with an ultra-low load DCM-II actuator utilising a Continuous Stiffness Measurement (CSM) module to determine the micromechanical complex shear modulus(Peters et al., 2017).

Instrument calibration is carried out in-situ before each indentation. Microscope and indenter were calibrated to focus and tip was cleaned by indentations on double tape. During testing, Samples were mounted into a custom-made liquid cell holder, with a 21 cm radius and 1.7 mm deep well (see in appendix A), which could allow partial submersion of the samples in distilled water during testing. Samples were then examined under the built-in optical microscope to select indentation locations

randomly. Five indents with 200 μm of spacing were made on the sample surface at a fixed frequency of 110 Hz (the resonant frequency of the indenter) with 500 nm oscillation amplitude (Peters et al., 2017). This frequency has the resonant frequency of the indenter and at this frequency instrument uncertainty is minimized, as reported by Akhtar et al (2018). Contact stiffness and damping were obtained through electromagnetic oscillation sequences. The initial oscillation measured instrument stiffness and damping. These were then subtracted from the total measurement to obtain the contact response. Material properties were then obtained during the second oscillation.

After each indentation, the tip was cleaned to prevent any transfer of biological material to the subsequent indentation site that may affect measurements. This was achieved by indenting an adjacent sample holder, which was mounted with 3 M double-sided Scotch tape. This method was found to be effective at cleaning the tip without picking up any residue from the Scotch tape. Following testing of each sample, further indents were made on fused silica with the test sites.

6.2.2 Analysis of mechanical properties

The sclera is nearly incompressible, so a Poisson's ratio of 0.50 was assumed for the sclera (Rada et al., 2006) allowing the calculation of the shear storage modulus, G', shear loss modulus, G'', and the loss factor after each indentation. The theoretical basis is outlined in brief below and has been described in more detail previously (Herbert et al., 2009, Akhtar et al., 2018).

Sneddon's analysis (Sneddon, 1965) is used to calculate the shear storage modulus (G') using Poisson's ratio (v), contact stiffness (S) and tip diameter (D), based on using a flat cylindrical punch:

$$G' = S\,(1 - v) \tag{6.1}$$

The above components along with contact damping (C_w) can be used to calculate the shear loss modulus, G″:

$$G'' = C_W(1 - v) \tag{6.2}$$

The loss factor, tan δ, is defined as the loss modulus divided by the storage modulus:

$$\tan\delta = G''/G' \tag{6.3}$$

The relationship between shear modulus and the elastic modulus (E) can be defined as:

$$G' = \frac{E}{2(1+v)} \tag{6.4}$$

6.2.3 Statistical analysis

Intra-group homogeneity was studied via the Kruskal-Wallis ANOVA test using Origin OriginLab, Northampton, MA) to determine if there were significant variations between measurements of the samples' mechanical properties within each treatment group. Following this, group differences were assessed via suitable 2-sample independent tests selected after appraisal of data normality and homoscedasticity. Differences in scleral mechanical properties were tested with the Kruskal-Wallis ANOVA and the Mann-Whitney post-hoc test. For the statistical

significance of mechanical properties between pre and post-treatment groups, one-way ANOVA was applied to the data. (If a p-value is less than 0.05, it is flagged with one star (*). If a p-value is less than 0.01, it is flagged with two stars (**). If a p-value is less than 0.001, it is flagged with three stars (***). If a p-value is less than 0.0001, it is flagged with four stars (****))

6.3 Results

The Kruskal-Wallis ANOVA test was performed for each group to ensure no measurement within any one incubation group was skewing the data. The test confirmed that there were no significant differences between samples in the same incubation group (Kruskal-Wallis ANOVA, $p>0.05$). Both the overall shear storage modulus, G', and the shear loss modulus, G'', reduced after treatment with both $\propto$-amylase and chondroitinase ABC compared with control samples.

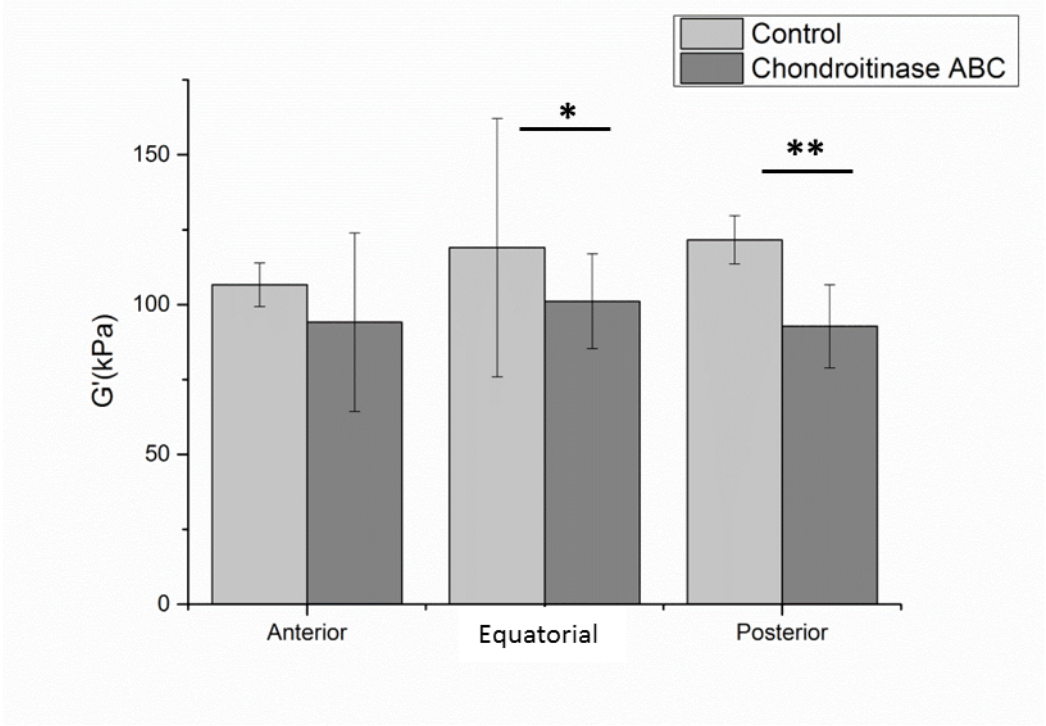

Figure 6.5. Shear storage modulus G´ for specimens from the three regions after treatment with control and chondroitinase ABC buffer. (n=140, 70 indents pre-treatment and 70 indents post treatment)

There was a significant decrease of G´ in the equatorial and posterior regions of sclera after incubation with chondroitinase ABC compared to control. G´ of samples incubated with chondroitinase ABC showed no statistical difference in the anterior region compared to control. G´ decreased more in the posterior region than in the equatorial region after incubation with chondroitinase ABC.

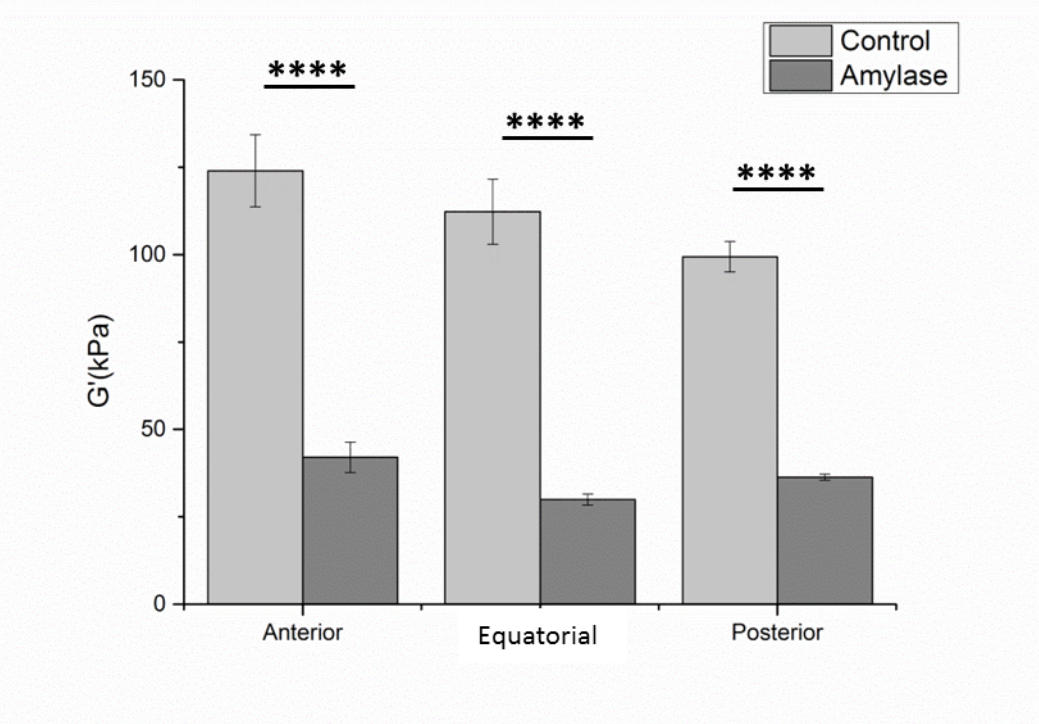

Figure 6.6 Shear storage modulus G´ for specimens from the three regions after treatment with control and ∝-amylase buffer. (n=140, 70 indents pre-treatment and 70 indents post treatment)

The shear storage modulus G´ decreased significantly in all regions after incubation with ∝-amylase compared to control. It decreased the most in the equatorial region and least in the posterior region after incubation with ∝-amylase.

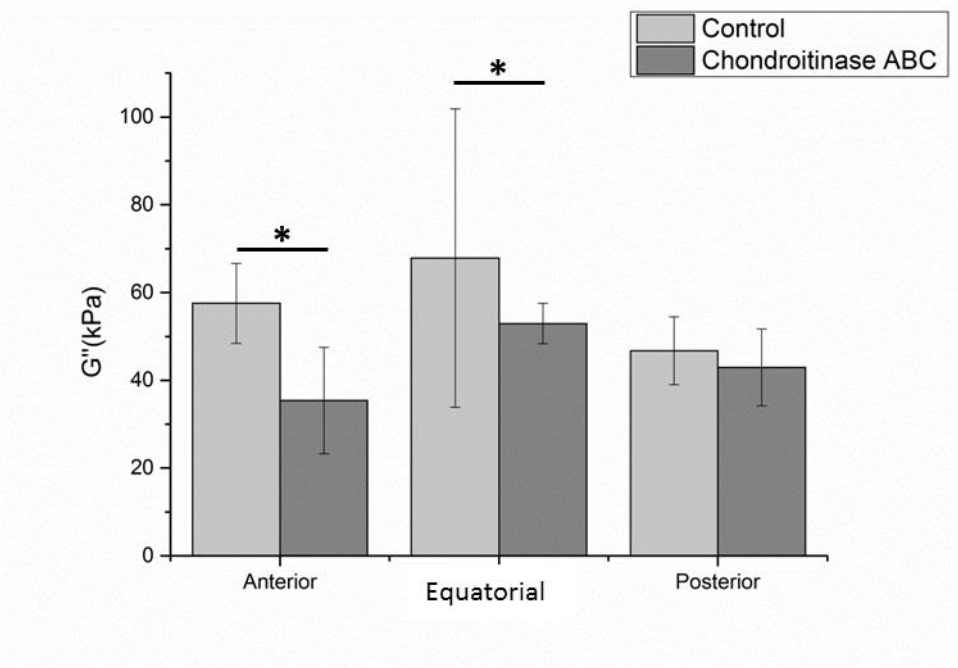

Figure 6.7 Shear loss modulus G″ for specimens from the three regions after treatment with control and chondroitinase ABC buffer. (n=140, 70 indents pre-treatment and 70 indents post treatment)

There was a significant G″ in the anterior and equatorial regions of sclera after incubation with chondroitinase ABC compared to control. G″ of the sample incubated with chondroitinase ABC showed no statistical difference in the posterior region compared to control. G″ decreased more in the anterior region than in the equatorial region after incubation with chondroitinase ABC.

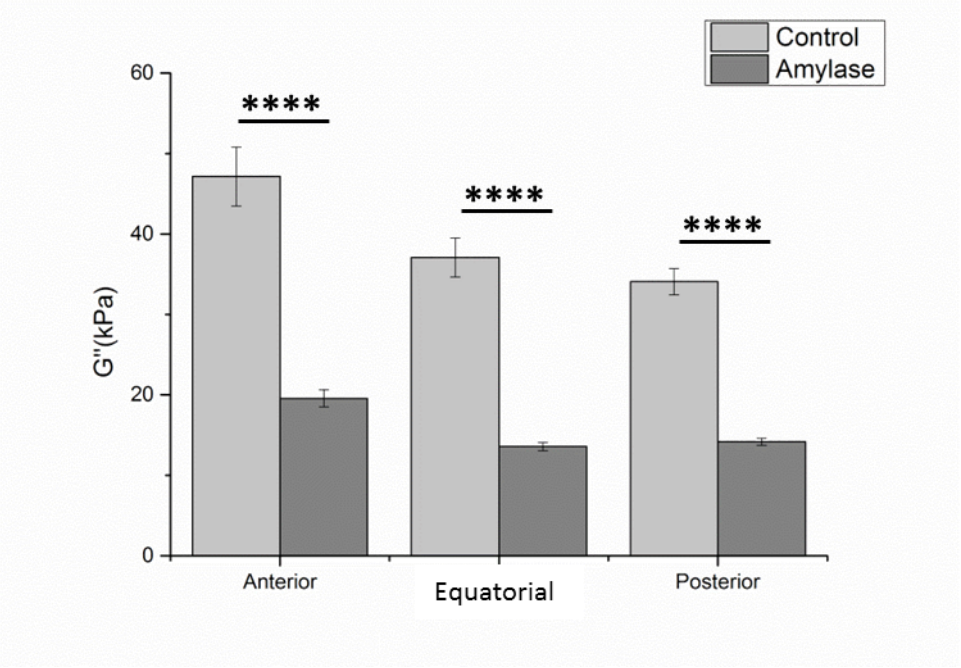

Figure 6.9 Shear loss modulus G″ for specimens from the three regions after treatment with control and ∝-amylase buffer. (n=140, 70 indents pre-treatment and 70 indents post treatment)

The shear loss modulus G″ decreased significantly in all regions of sclera after incubation with ∝-amylase compared to control. It decreased most in the equatorial region and least in the posterior region after incubation with ∝-amylase.

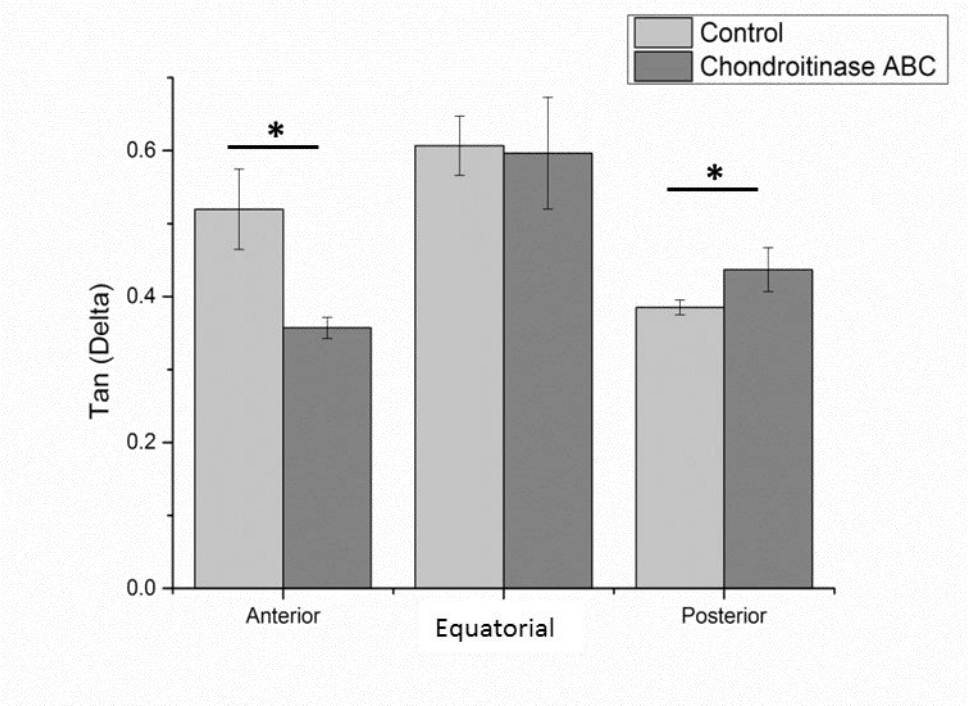

Figure 6.10 The loss factor for specimens from the three regions after treatment with control and chondroitinase ABC buffer. (n=140, 70 indents pre-treatment and 70 indents post treatment)

The loss factor of specimens incubated with chondroitinase ABC was found to be significantly decreased after incubation with chondroitinase ABC. However, an increase of loss factor was found in samples from the posterior region incubated with chondroitinase ABC. There was no significant difference in the equatorial region compared with samples incubated with control buffer.

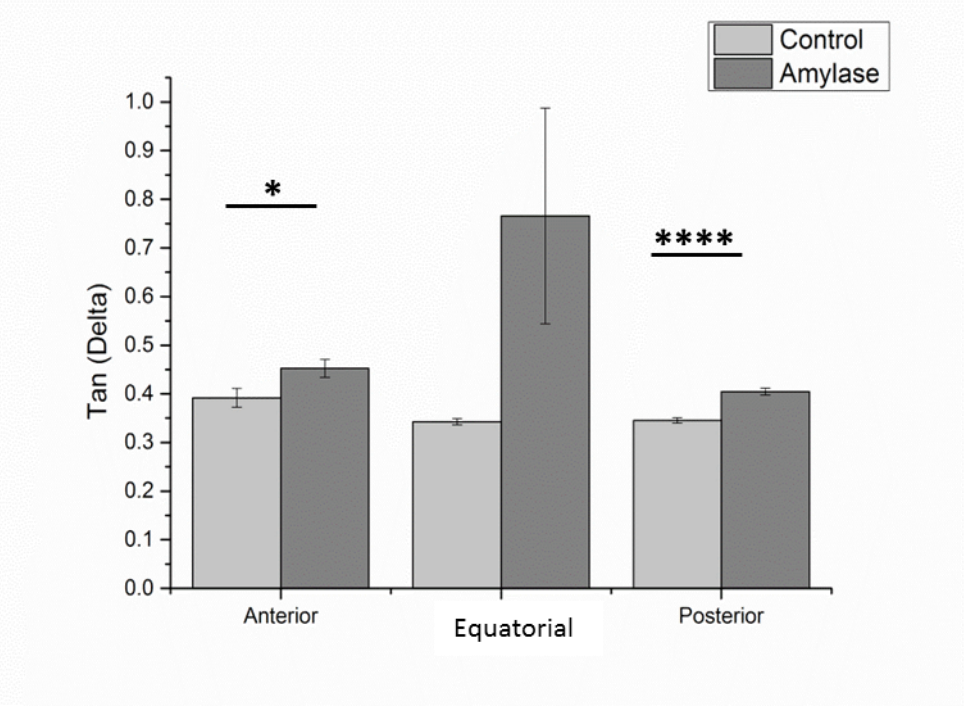

Figure 6.11 The loss factor for specimens from the three regions after treatment with control and ∝-amylase buffer. (n=140, 70 indents pre-treatment and 70 indents post-treatment)

The loss factor increased significantly in all three regions after incubation with ∝-amylase. The loss factor increased most in the equatorial region and least in the posterior region.

Table 6.1 Results of the shear storage modulus, G´, shear loss modulus, G´', and the loss factor from each group, presented as mean value, standard error of mean (SE), statistical significance (Student's t-test, p) and reduction compared to control.

Regions	Treatment		Control Mean ± SE	Treated Mean ± SE	P value	Reduced (%)
Anterior Region	α-amylase	G´(kPa)	124.00 ± 10.347	42.02 ± 1.335	0.0000	66.11
		G´'(kPa)	47.15 ± 3.675	19.57 ± 1.059	0.0000	58.49
		Tan (Delta)	0.39 ± 0.019	0.45 ± 0.018	0.0280	-
	Chondroitinase ABC	G´(kPa)	106.69 ± 7.270	94.12 ± 29.837	0.4091	-
		G´'(kPa)	57.55 ± 9.093	35.39 ± 12.146	0.0490	38.50
		Tan (Delta)	0.52 ± 0.055	0.36 ± 0.015	0.0124	-
Equatorial Region	α-amylase	G´(kPa)	112.26 ± 9.301	29.96 ± 1.561	0.0000	73.31
		G´'(kPa)	37.09 ± 2.416	13.58 ± 0.514	0.0000	63.40
		Tan (Delta)	0.34 ± 0.006	0.77 ± 0.222	0.0075	-
	Chondroitinase ABC	G´(kPa)	118.99 ± 43.109	101.13 ± 15.823	0.0406	15.00
		G´'(kPa)	67.85 ± 34.009	52.95 ± 4.601	0.0281	21.97
		Tan (Delta)	0.61 ± 0.041	0.60 ± 0.077	0.0552	-
Posterior Region	α-amylase	G´(kPa)	99.43 ± 4.347	36.35 ± 0.849	0.0000	63.44
		G´'(kPa)	34.09 ± 1.621	14.38 ± 0.449	0.0000	57.83
		Tan (Delta)	0.35 ± 0.005	0.40 ± 0.007	0.0000	-
	Chondroitinase ABC	G´(kPa)	121.63 ± 8.085	92.78 ± 13.858	0.0142	23.73
		G´'(kPa)	46.76 ± 7.745	42.96 ± 8.772	0.055	-
		Tan (Delta)	0.39 ± 0.010	0.44 ± 0.030	0.0150	-
All Regions	α-amylase	G´(kPa)	108.55 ± 4.849	36.33 ± 1.666	0.0000	66.53
		G´'(kPa)	38.14 ± 1.567	15.89 ± 0.469	0.0000	58.33
		Tan (Delta)	0.36 ± 0.006	0.53 ± 0.068	0.3364	-
	Chondroitinase ABC	G´(kPa)	133.17 ± 11.484	96.76 ± 10.674	0.0254	27.34
		G´'(kPa)	67.92 ± 10.064	45.33 ± 4.615	0.0533	32.27
		Tan (Delta)	0.49 ± 0.032	0.49 ± 0.040	0.877	-

6.4 Discussion

The shear storage modulus of the group treated with α-amylase reduced in all three regions compared to control. It was reduced the most in the equatorial region and least in the posterior region. This result shows the same trend with the results in the previous chapter using AFM: α-Amylase has the same effect on the mechanical properties of sclera in both the nano- and micro-level. Previous studies have shown similar results in corneas treated with α-amylase: a reduction in corneal stiffness. (Spoerl et al., 2012) However, the s-GAG content measurement shows that α-amylase releases the s-GAG the most in the anterior region and the least in the posterior region. This result is different from the mechanical results obtained from nanoindentation and AFM (i.e. reduced most in the equatorial region). This difference suggests that, other than sulphate PGs, α-amylase may affect other scleral matrix components that contribute to the mechanical properties of the sclera.

Previous studies show that alterations in s-GAG content may contribute to the altered creep and stiffness of the sclera (Murienne et al., 2016) This reduction in the shear storage modulus in the equatorial and posterior regions has also been found in tissue incubated with chondroitinase ABC compared to control. The shear storage modulus reduced most in the posterior region and least in the anterior region. This result shows the same trend with the result in the previous chapter using AFM. Thus, chondroitinase ABC has the same trend of regional effect on the mechanical properties of sclera in both the nano- and micro-level. However, the reductions of mechanical properties at the nano- level after incubation with chondroitinase ABC

are much more significant than at the micro-level. This difference suggests that the PGs depleted by chondroitinase ABC have a more significant contribution to scleral mechanical properties at the nano- level than at the micro- level.

G″ is reduced after incubation with both enzymes. However, the reductions are much more significant in samples incubated with α-amylase than samples incubated with chondroitinase ABC. Previous studies have suggested that shear loss modulus G´’ is particularly sensitive to a specimen’s microstructure (Adibnia and Hill, 2016). This significant difference in G″ after incubation with α-amylase may provide an explanation of the visually observed change in the collagen bundle distribution found in specimens after α-amylase incubation in Chapter 4.

As manifested by the loss factor, the scleral tissue became less elastic in all three regions incubated with α-amylase, and the posterior region when incubated with chondroitinase ABC. The changes in the loss factor were significantly different between samples in all three regions after incubation with chondroitinase ABC. This proves an instant loss of chondroitin and dermatan sulphate GAGs as a result of regional differences in the effect on scleral elasticity.

6.5 Conclusion

Results from this chapter have shown that proteoglycan depletion with both enzymes lead to reduction of the tissue shear storage modulus. However, there are significant differences in regional mechanical properties between control and enzyme-incubated group, and between α-amylase- and chondroitinase ABC-incubated groups. This suggests that different types of proteoglycan have different contributions towards the mechanical properties of sclera. Moreover, comparison of the enzymatic result

between this chapter to Chapter 5 shows chondroitinase ABC has more significant effect for scleral tissue mechanical properties at the collagen level (nanometre scale) and α-amylase has more significant effect on the scleral matrix level (micrometre scale).

Chapter 7 Conclusion

7.1 Summary of finding

Results from Chapter 3 shows significant variations in the scleral protein analyse pattern (Coomassie blue staining) incubated with α-amylase and chondroitinase ABC. Also, the sGAG content reduced significantly after incubated with both enzymes. These results indicated that both enzymes could cause proteoglycan depletion in the sclera tissue. However, the α-amylase affects the most in the anterior region and least in the posterior region. This trend is different from the result incubated with chondroitinase ABC. Also worth mentioning is chondroitinase ABC, and α-amylase were showing the effect on the protein with different molecular weight. Chondroitinase ABC was showing effects on weight 130 and 270 kDa especially in the posterior region. These share similarities in the regional distribution and apparent molecular weight with decorin and biglycan. However, no change by chondroitinase ABC was found in protein weight 66 and 52 kDa. The α-amylase results decreases of the density of all bands in 270, 130, 66 and 52kDa in the anterior region, however, the regional distribution suggest the proteoglycan depleted by α-amylase are not decorin and biglycan. Difference effect of two enzymes have also been found in the sGAG content measurement result, and the sGAG content reduced the most in the anterior region and least in the posterior region. This trend is the opposite with the result incubated with chondroitinase ABC (reduced most in the posterior region and least in the anterior region). This difference indicated that ∝-amylase does not affect

the s-GAGs depleted by chondroitinase ABC which are chondroitin sulphate and dermatan sulphate.

Chapter 4 observed and measured the nanostructure of collagen fibrils in scleral tissue after hydration and proteoglycan depletion. In this chapter, irregular change in collagen fibrils like ‘fusion’ and ‘splitting up’ have been found in proteoglycan-depleted tissues. These reactions to proteoglycan depletion indicated that collagen fibrils lose regularity when lack of proteoglycan. Also, the collagen fibril diameters significantly reduced after enzyme incubation, suggesting that an acute loss of proteoglycan will cause a reduction in collagen fibril size. Abnormal small and irregular shape collagen fibrils were found in the transverse sections SEM images in the previous study on the sclera of the highly myopic eye (Harper and Summers, 2015). Results from this study showed the similar result and possibly provided an explanation of why the irregular change has been found in the proteoglycan reduced tissue like sclera from the myopic eye. No statistically significant changes have been found in collagen D-period after all incubation suggesting that the collagen fibrils not be degraded by any treatments from this study. Previous studies have shown that the collagen gap zone depth indicates the collagen fibril hydration level (Spitzner et al., 2015). Collagen gap zone depth increased after incubation with distilled water and PBS buffer. Collagen diameter increased after incubation with distilled water, and it remained unchanged after incubation with PBS buffer, suggesting that the collagen fibrils swelled in both dimensions after being hydrated with distilled water, but only in height after incubation with PBS buffer. Gap zone depth decreased after treatment with α-amylase and chondroitinase ABC, suggesting that proteoglycan depletion reduced the function of collagen fibril hydration.

Chapter 5 investigated the scleral nanomechanical change following hydration with distilled water and PBS buffer and proteoglycan depletion with chondroitinase ABC and α-amylase. The overall elastic modulus increased after incubation with PBS buffer (pH7.4, NaCI 137mmol/L). A similar increase of mechanical properties was found in collagen fibril treated with a water-based salt solution in a previous study (Grant et al., 2009). The mean value of the elastic modulus decreased in all three regions, and this finding is also similar to previous finding on hydrated human corneal stroma (Xia et al., 2014). In this chapter, the elastic modulus decreases in all regions after being incubated with both enzymes. However, the reduction of two enzymes was different across the three scleral regions. The elastic modulus reduced most in the posterior region and least in the anterior region after being incubated with Chondroitinase ABC, which shows a similar distribution of chondroitin and dermatan sulphate. The α-amylase shows different effects on the distribution of sclera. The elastic modulus reduced most in the equatorial region and least in the posterior region. The standard error of the mechanical modulus in the sample after α-amylase incubation was greater than chondroitinase ABC, showing that the effect of α-amylase on scleral tissue is less stable than chondroitinase ABC.

In chapter 6 the shear storage modulus of the group treated with α-Amylase reduced in all three regions compared to control. It reduced the most in the equatorial region and least in the posterior region. This result shows the same trend with the result in the previous chapter using AFM, and it proved that α-Amylase has the same effect of the mechanical properties in both nano- and micro- level. However, the sGAG content measurement shows α-Amylase release the most sGAG in the anterior region and least in the posterior region, and this result is different from the mechanical

result from nanoindentation and AFM (reduced most in the equatorial region). This difference has suggested a possibility that other than sulphate proteoglycan, α-Amylase may have an effect on other scleral matrix components that have contributed to the scleral mechanical properties. The reduces in the shear storage modulus in equatorial and posterior regions have also been found in the group incubated with chondroitinase ABC compare to control. The shear storage modulus reduced most in the posterior region and least in the anterior region; this result shows the same trend with DMMB result and the result in the previous chapter using AFM. These results proved that chondroitinase ABC has the same trend of regional effect on the mechanical properties in both nano- and micro- level. However, the reductions of mechanical properties in nano-level after chondroitinase ABC are much more significant than in the micro-level. This difference suggested the PGs depleted by chondroitinase ABC have the more significant contribution to scleral mechanical properties in nano-level than in micro-level. G″ reduced after incubated with both enzymes; however, the reductions are much more significant in samples incubated with α-Amylase than samples incubated with chondroitinase ABC. The study has shown the G″ is particularly sensitive to a specimens microstructure. (Adibnia and Hill, 2016), the significant difference in G″after incubated with α-Amylase may provide an explanation of the visually observed change in the collagen bundle distribution found in specimens after α-Amylase incubation in chapter 4.

Summary of the outcomes in study are showing in the 7.1.

Modulus	Change after incubation with α-Amylase		Change after incubation with Chondroitinase ABC	Change after incubation with both enzymes
Glycan structure	A>E>P	≠	P>E>A	
sGAG content	A>E>P	≠	P>E>A	
Collagen diameter	Reduced	>	Reduced	Reduced
Collagen D-period	No change	=	No change	No change
Collagen Gap Depth	Increased	<	Increased	Increased
Collagen fibrils distribution	Change observed	≠	No Change observed	
E (Nano-scale)	Reduced, E>A>P	>	Reduced, P>E>A	Reduced
G' (Micro-scale)	Reduced , E>A>P	>	Reduced, P>E>A	Reduced
G'' (Micro-scale)	Reduced , E>A>P	>	Reduced, A>E>P	Reduced

Figure 7.1 The outcome summery of this study. Modulus Changes found in the sclera tissue after enzyme incubations by different technique approaches.

7.2 Key contribution

There are 4 key findings in this work that may contribute to the field of experimental mechanics and scleral biomechanics:

- Both α-Amylase and chondroitinase ABC result in proteoglycan depletion in all three regions of the sclera.

- Proteoglycan depletion could cause a reduction in collagen fibrils' size; and reduction in the collagen fibril hydration functions. However, proteoglycan depletion does not effect on the molecular structure of collagen fibrils.

- The significant change in collagen fibrils distribution were observed in tissue incubated with α-Amylase, however this change was not observed in the tissue incubated with chondroitinase ABC.

- Proteoglycan depletion leads to significant reduction in both nanoscale and microscale mechanical properties of the sclera.

- The α-Amylase and chondroitinase ABC are depleting the different type of proteoglycan, result a significant regional difference in both structure and mechanical proteoglycan depletion results.

Chapter 8 Limitations and future work

8.1 Limitations

The limitations and discussions specific to each part of this thesis were detailed in the corresponding chapter. However, several important limitations should be acknowledged here:

- All experimental works in this study were conducted at room temperature. Although the activities of the enzymes under room temperature were confirmed by pilot studies and standard activity curve provided by predictor (see in appendix), 37^{o}C is still the best option for proteoglycan depletion experiments as this temperature provided a reaction environment similar in human body.

- Although the gloves and lab coat were wearing when handling the enzymes, there are still possibilities for contamination in this research. Contamination of the enzyme could cause large standard deviation in the overall result, For avoiding the contamination in the future work, enzyme inhibitors and filter could be used before each treatment.

- This study aims to study the scleral nanostructure and mechanical properties through all three regions, and the changes in sclera following proteoglycan depletion. Although the molecular weight ranges of effected proteoglycan have been pointed out in chapter 2, the type of depleted PGs were still not

specific. Further conclusion on the structure and mechanical contribution by specific proteoglycan could not be made in this study.

- In chapter 5 and 6, nano- and micro-scale α-amylase treated mechanical result shows the same regional trend proved the accuracy of the experiments. However, the regional mechanical results were not consisting with the regional sGAG content result after α-amylase from chapter 2. The difference indicated α-amylase has the effect on other sclera matrix components which are not sulphated and contribute to the mechanical properties, possibly have the highest concentration in the equatorial region.

- AFM and nanoindentation used in this study were surface probing technology, structure and mechanical results from this study were all from the outer layer of sclera only. Although there is no study indicated the concentration of proteoglycan through inner, middle and outer layer of sclera, there are studies showed collagen fibrils size are different between the three layers: collagen fibrils are thinnest in the inner layer and thickest in the outer layer of sclera (McBrien et al., 2001, McBrien et al., 2003).

8.2 future directions

The main future directions suggested by the study are 1). Investigating the specific PGs in the sclera and their contribution towards tissue structure and mechanical properties. 2). Investigating the α-amylase and its effect on the scleral and corneal components.

Most of the structure and mechanical studies of sclera were focused on the posterior part of the sclera (Murienne et al., 2016, Kaya and Yildirim, 2016, Grytz et al., 2014, Coudrillier et al., 2012), this is because the two primary diseases (myopia and glaucoma) involves shape altering in sclera have occurred in the posterior part of the eye. However the results from this study have provided a new angle to study pathologies like myopia and glaucoma, this study has proved the proteoglycan is one of the critical factors that influence the structure and mechanical properties in sclera and the PGs are not evenly distributed in the sclera, different type of the PGs have different contribution towards tissue structure, mechanical properties or hydration function. Furthermore, alteration of scleral shape complicated with reduction of proteoglycan has been reported in the aged eyes (Wang et al., 2018, Rada et al., 2015). Investigating the specific PGs and their structure and mechanical contribution to the scleral tissue can provide a better understanding of the role proteoglycan plays in the sclera pathology and ageing. In the long term, the possibility of using proteoglycan triggering specific microstructural or mechanical changes that are beneficial against glaucoma or myopia could be invested, thus avoiding the need for surgical intervention.

Unlike chondroitinase ABC, α-amylase is an enzyme that found in the human tear fluid (Van Haeringen et al., 1975). This present of α-amylase means the α-amylase is existed in the eye environment and interacts with eye tissue all the time. Furthermore increase of α-amylase has been found in the keratoconus patients (Spoerl et al., 2012). Finally, results from this study have shown that the α-amylase has the significant effect on both scleral microstructure and mechanical properties. All of these findings indicated the importance of investigating the α-amylase and its

effect on both scleral and corneal components. However, since Quintarelli et al. (1969) pointed out α-amylase has the effect on collagen-proteoglycan interaction in connective tissue. To the author's knowledge, no study since has investigated the α-amylase in connective tissue, and none of the studies ever has investigated the α-amylase in the ocular tissue. For effect of α-amylase on ocular tissue, this study has pointed out a blank area both in biochemistry and biomechanics field.

Reference

ADIBNIA, V. & HILL, R. J. 2016. Universal aspects of hydrogel gelation kinetics, percolation and viscoelasticity from PA-hydrogel rheology. *Journal of Rheology,* 60**,** 541-548.

AKHTAR, R., DRAPER, E. R., ADAMS, D. J. & HAY, J. 2018. Oscillatory nanoindentation of highly compliant hydrogels: A critical comparative analysis with rheometry. *Journal of Materials Research,* 33**,** 873-883.

AKHTAR, R., SHERRATT, M. J., CRUICKSHANK, J. K., DERBY, B., AKHTAR, R., SHERRATT, M. J., CRUICKSHANK, J. K. & DERBY, B. 2011. Characterizing the elastic properties of tissues. *Materials Today,* 14**,** 96.

AMEYE, L. & YOUNG, M. F. 2002. Mice deficient in small leucine-rich proteoglycans: novel in vivo models for osteoporosis, osteoarthritis, Ehlers-Danlos syndrome, muscular dystrophy, and corneal diseases. *Glycobiology,* 12**,** 107R-116R.

AUSTIN, B. A., COULON, C., LIU, C.-Y., KAO, W. W.-Y. & RADA, J. A. 2002. Altered collagen fibril formation in the sclera of lumican-deficient mice. *Investigative ophthalmology & visual science,* 43**,** 1695-1701.

AVETISOV, E., SAVITSKAYA, N., VINETSKAYA, M. & IOMDINA, E. 1983a. A study of biochemical and biomechanical qualities of normal and myopic eye sclera in humans of different age groups. *Metabolic, pediatric, and systemic ophthalmology,* 7**,** 183-188.

AVETISOV, E. S., SAVITSKAYA, N. F. & VINETSKAYA, M. I. 1983b. A study of biochemical and biomechanical qualities of normal and myopic eye sclera in humans of different age groups. *Metabolic, Pediatric, and Systemic Ophthalmology,* 7**,** 183-188.

AYAD, S., BOOT-HANDFORD, R., HUMPHRIES, M., KADLER, K. & SHUTTLEWORTH, A. 1998. *The extracellular matrix factsbook,* Elsevier.

BARRETT, S. D. 2008. Image sxm. *Liverpool L69 E,* 72**,** 2008.

BATTAGLIOLI, J. & KAMM, R. 1984. measurements of the compressive properties of scleral tissue. *Investigative ophthalmology & visual science,* 25(1)**,** 59-65.

BENGTSSON, B. 1981. The prevalence of glaucoma. *British Journal of Ophthalmology,* 65**,** 46-49.

BOOTE, C., HAYES, S., YOUNG, R. D., KAMMA-LORGER, C. S., HOCKING, P. M., ELSHEIKH, A., INGLEHEARN, C. F., ALI, M., MEEK, K. M., BOOTE, C., HAYES, S., YOUNG, R. D., KAMMA-LORGER, C. S., HOCKING, P. M., ELSHEIKH, A., INGLEHEARN, C. F., ALI, M. & MEEK, K. M. 2009. Ultrastructural changes in the retinopathy, globe enlarged (rge) chick cornea. *Journal of structural biology,* 166**,** 195.

BORCHERDING, M. S., BLACIK, L., SITTIG, R., BIZZELL, J. W., BREEN, M. & WEINSTEIN, H. 1975. Proteoglycans and collagen fibre organization in human corneoscleral tissue. *Experimental eye research,* 21**,** 59-70.

BOUCHONVILLE, N., MEYER, M., GAUDE, C., GAY, E., RATEL, D. & NICOLAS, A. 2016. AFM mapping of the elastic properties of brain tissue reveals kPa μm− 1 gradients of rigidity. *Soft Matter,* 12**,** 6232-6239.

BREEN, M., JOHNSON, R. L., SITTIG, R., WEINSTEIN, H. & VEIS, A. 1972. The acidic glycosaminoglycans in human fetal development and adult life: Cornea, sclera and skin. *Connective Tissue Research,* 1**,** 291-303.

BRUKER NANO INC. *AFM Probes* [Online]. [Accessed].

BURGOYNE, C. F., DOWNS, J. C., BELLEZZA, A. J., SUH, J.-K. F. & HART, R. T. 2005. The optic nerve head as a biomechanical structure: a new paradigm for understanding the role of IOP-related stress and strain in the pathophysiology of glaucomatous optic nerve head damage. *Progress in retinal and eye research,* 24**,** 39-73.

CAMERON, G., ALBERTS, I., LAING, J. & WESS, T. 2002. Structure of type I and type III heterotypic collagen fibrils: an X-ray diffraction study. *Journal of structural biology,* 137**,** 15-22.

CAMPBELL, I. C., COUDRILLIER, B. & ROSS ETHIER, C. 2014. Biomechanics of the posterior eye: a critical role in health and disease. *J Biomech Eng,* 136**,** 021005.

CELORIO, J. & PRUETT, R. C. 1991. Prevalence of lattice degeneration and its relation to axial length in severe myopia. *American journal of ophthalmology,* 111**,** 20-23.

CHEN, K., ROWLEY, A. P., WEILAND, J. D. & HUMAYUN, M. S. 2014. Elastic properties of human posterior eye. *Journal of Biomedical Materials Research Part A,* 102**,** 2001-2007.

CHOI, S., CHEONG, Y., LEE, H.-J., LEE, S. J., JIN, K.-H. & PARK, H.-K. 2011. AFM study for morphological and mechanical properties of human scleral surface. *Journal of nanoscience and nanotechnology,* 11**,** 6382-6388.

CLARK, S. J., KEENAN, T. D., FIELDER, H. L., COLLINSON, L. J., HOLLEY, R. J., MERRY, C. L., VAN KUPPEVELT, T. H., DAY, A. J. & BISHOP, P. N. 2011. Mapping the differential distribution of glycosaminoglycans in the adult human retina, choroid, and sclera. *Invest Ophthalmol Vis Sci,* 52**,** 6511-21.

COUDRILLIER, B., PIJANKA, J., JEFFERYS, J., SORENSEN, T., QUIGLEY, H. A., BOOTE, C. & NGUYEN, T. D. 2015a. Collagen structure and mechanical properties of the human sclera: analysis for the effects of age. *Journal of biomechanical engineering,* 137**,** 041006.

COUDRILLIER, B., PIJANKA, J. K., JEFFERYS, J. L., GOEL, A., QUIGLEY, H. A., BOOTE, C. & NGUYEN, T. D. 2015b. Glaucoma-related Changes in the Mechanical Properties and Collagen Micro-architecture of the Human Sclera. *PLoS One,* 10**,** e0131396.

CURTIN, B. J. 1969. Physiopathologic aspects of scleral stress-strain. *Transactions of the American Ophthalmological Society,* 67**,** 417.

CURTIN, B. J., IWAMOTO, T. & RENALDO, D. P. 1979. Normal and staphylomatous sclera of high myopia: an electron microscopic study. *Archives of ophthalmology,* 97**,** 912-915.

DOWNS, J. C., SUH, J. F., THOMAS, K. A., BELLEZZA, A. J., HART, R. T. & BURGOYNE, C. F. 2005. Viscoelastic material properties of the

peripapillary sclera in normal and early-glaucoma monkey eyes. *Investigative ophthalmology & visual science,* 46**,** 540-546.

DUNLEVY, J. R. & RADA, J. A. S. 2004. Interaction of lumican with aggrecan in the aging human sclera. *Investigative ophthalmology & visual science,* 45**,** 3849-3856.

ECKERT, C. E., FAN, R., MIKULIS, B., BARRON, M., CARRUTHERS, C. A., FRIEBE, V. M., VYAVAHARE, N. R. & SACKS, M. S. 2013. On the biomechanical role of glycosaminoglycans in the aortic heart valve leaflet. *Acta biomaterialia,* 9**,** 4653-4660.

EILAGHI, A., FLANAGAN, J. G., SIMMONS, C. A. & ETHIER, C. R. 2010. Effects of scleral stiffness properties on optic nerve head biomechanics. *Annals of biomedical engineering,* 38**,** 1586-1592.

ELSHEIKH, A., ALHASSO, D. & RAMA, P. 2008. Biomechanical properties of human and porcine corneas. *Experimental eye research,* 86**,** 783-790.

ELSHEIKH, A. & ANDERSON, K. 2005. Comparative study of corneal strip extensometry and inflation tests. *Interface,* 2.

FAZIO, M. A., GRYTZ, R., BRUNO, L., GIRARD, M. J., GARDINER, S., GIRKIN, C. A. & DOWNS, J. C. 2012. Regional variations in mechanical strain in the posterior human sclera. *Investigative ophthalmology & visual science,* 53**,** 5326-5333.

FECHTNER, R. D. & WEINREB, R. N. 1994. Mechanisms of optic nerve damage in primary open angle glaucoma. *Survey of ophthalmology,* 39**,** 23-42.

FOSTER, C. & DE LA SAINZ MAZA, M. The Sclera. 1994. Springer, Berlin, Heidelberg, New York.

FRATZL, P. & MEEK, K. M. 2008. Collagen: structure and mechanics, an introduction. *Collagen.* Springer.

FULLWOOD, N. J., HAMMICHE, A., POLLOCK, H. M., HOURSTON, D. J. & SONG, M. 1995. Atomic force microscopy of the cornea and sclera. *Current eye research,* 14**,** 529-535.

GERAGHTY, B., JONES, S. W., RAMA, P., AKHTAR, R. & ELSHEIKH, A. 2012. Age-related variations in the biomechanical properties of human sclera. *Journal of the mechanical behavior of biomedical materials,* 16**,** 181-191.

GERAGHTY, B., WHITFORD, C., BOOTE, C., AKHTAR, R. & ELSHEIKH, A. 2015. Age-related variation in the biomechanical and structural properties of the corneo-scleral tunic. *Mechanical Properties of Aging Soft Tissues.* Springer.

GERLIE, C., KODA, R. T. & LIEN, E. J. 2000. Glucosamine and chondroitin sulfates in the treatment of osteoarthritis: a survey. *Progress in drug research.* Springer.

GIRARD, M. J., DOWNS, J. C., BURGOYNE, C. F. & SUH, J.-K. F. 2008. Experimental surface strain mapping of porcine peripapillary sclera due to elevations of intraocular pressure. *Journal of biomechanical engineering,* 130**,** 041017.

GRANT, C. A., BROCKWELL, D. J., RADFORD, S. E. & THOMSON, N. H. 2008. Effects of hydration on the mechanical response of individual collagen fibrils. *Applied Physics Letters,* 92**,** 233902.

GRANT, C. A., BROCKWELL, D. J., RADFORD, S. E., THOMSON, N. H., GRANT, C. A., BROCKWELL, D. J., RADFORD, S. E. & THOMSON, N.

H. 2009. Tuning the Elastic Modulus of Hydrated Collagen Fibrils. *Biophysical Journal (Science Direct),* 97**,** 2985.

GRANT, C. A., THOMSON, N. H., SAVAGE, M. D., WOON, H. W. & GREIG, D. 2011a. Surface characterisation and biomechanical analysis of the sclera by atomic force microscopy. *J Mech Behav Biomed Mater,* 4**,** 535-40.

GRANT, C. A., THOMSON, N. H., SAVAGE, M. D., WOON, H. W., GREIG, D., GRANT, C. A., THOMSON, N. H., SAVAGE, M. D., WOON, H. W. & GREIG, D. 2011b. Surface characterisation and biomechanical analysis of the sclera by atomic force microscopy. *Journal of the Mechanical Behavior of Biomedical Materials,* 4**,** 535.

GREENE, P. R. & MCMAHON, T. A. 1979. Scleral creep vs. temperature and pressure in vitro. *Experimental eye research,* 29**,** 527-537.

GRYTZ, R., FAZIO, M. A., GIRARD, M. J. A., LIBERTIAUX, V., BRUNO, L., GARDINER, S., GIRKIN, C. A., CRAWFORD DOWNS, J., GRYTZ, R., FAZIO, M. A., GIRARD, M. J. A., LIBERTIAUX, V., BRUNO, L., GARDINER, S., GIRKIN, C. A. & CRAWFORD DOWNS, J. 2014. Material properties of the posterior human sclera. *Journal of the Mechanical Behavior of Biomedical Materials,* 29**,** 602.

GRYTZ, R. & SIEGWART, J. T., JR. 2015. Changing material properties of the tree shrew sclera during minus lens compensation and recovery. *Invest Ophthalmol Vis Sci,* 56**,** 2065-78.

GUPTA, D., MOORE, D., BOJIKIAN, K. & SLABAUGH, M. 2013. Relationship between eye shape and the risk for glaucoma. *Investigative Ophthalmology & Visual Science,* 54**,** 3524-3524.

HAN, B., NIA, H. T., WANG, C., CHANDRASEKARAN, P., LI, Q., CHERY, D. R., LI, H., GRODZINSKY, A. J. & HAN, L. 2017. AFM-Nanomechanical Test: An interdisciplinary tool that links the understanding of cartilage and meniscus biomechanics, osteoarthritis degeneration, and tissue engineering. *ACS Biomaterials Science & Engineering,* 3**,** 2033-2049.

HARPER, A. R. & SUMMERS, J. A. 2015a. The dynamic sclera: extracellular matrix remodeling in normal ocular growth and myopia development. *Experimental eye research,* 133**,** 100-111.

HARPER, A. R. & SUMMERS, J. A. 2015b. The dynamic sclera: Extracellular matrix remodeling in normal ocular growth and myopia development. *Experimental eye research,* 133**,** 100.

HATAMI-MARBINI, H. & RAHIMI, A. 2014. The relation between hydration and mechanical behavior of bovine cornea in tension. *journal of the mechanical behavior of biomedical materials,* 36**,** 90-97.

HAUT, T. L. & HAUT, R. C. 1997. The state of tissue hydration determines the strain-rate-sensitive stiffness of human patellar tendon. *Journal of biomechanics,* 30**,** 79-81.

HEDBOM, E. & HEINEGÅRD, D. 1993. Binding of fibromodulin and decorin to separate sites on fibrillar collagens. *Journal of Biological Chemistry,* 268**,** 27307-27312.

HERBERT, E. G., OLIVER, W. C., LUMSDAINE, A. & PHARR, G. M. 2009. Measuring the constitutive behavior of viscoelastic solids in the time and frequency domain using flat punch nanoindentation. *Journal of Materials Research,* 24**,** 626.

HITCHCOCK, A. M., YATES, K. E., SHORTKROFF, S., COSTELLO, C. E. & ZAIA, J. 2006. Optimized extraction of glycosaminoglycans from normal and osteoarthritic cartilage for glycomics profiling. *Glycobiology,* 17**,** 25-35.

HO, L. T., HARRIS, A. M., TANIOKA, H., YAGI, N., KINOSHITA, S., CATERSON, B., QUANTOCK, A. J., YOUNG, R. D. & MEEK, K. M. 2014. A comparison of glycosaminoglycan distributions, keratan sulphate sulphation patterns and collagen fibril architecture from central to peripheral regions of the bovine cornea. *Matrix Biol,* 38**,** 59-68.

HODGE, A. J. 1963. Recent studies with the electron microscope on ordered aggregates of the tropocollagen macromolecule. *Aspects of protein structure***,** 289-300.

HOWELL, G. R., LIBBY, R. T., JAKOBS, T. C., SMITH, R. S., PHALAN, F. C., BARTER, J. W., BARBAY, J. M., MARCHANT, J. K., MAHESH, N. & PORCIATTI, V. 2007. Axons of retinal ganglion cells are insulted in the optic nerve early in DBA/2J glaucoma. *J Cell Biol,* 179**,** 1523-1537.

JAN, N. J., LATHROP, K. & SIGAL, I. A. 2017. Collagen Architecture of the Posterior Pole: High-Resolution Wide Field of View Visualization and Analysis Using Polarized Light Microscopy. *Invest Ophthalmol Vis Sci,* 58**,** 735-744.

JENSEN, B. 1982. *Iridology: Science and Practice in the Healing Arts*, B. Jensen.

JEROME, P., A, J. L. T. & H, M. K. 1957. Comparison of bovine corneal and scleral mucopolysaccharides. *Biochimica et Biophysica Acta,* 26**,** 361-364.

JIA, X., YU, J., LIAO, S. H. & DUAN, X. C. 2016. Biomechanics of the sclera and effects on intraocular pressure. *Int J Ophthalmol,* 9**,** 1824-1831.

JOHNSON, J. M., YOUNG, T. L. & RADA, J. 2006. Small leucine rich repeat proteoglycans (SLRPs) in the human sclera: identification of abundant levels of PRELP. *Mol Vis,* 12**,** 1057-1066.

KANAI, A. & KAUFMAN, H. E. 1972. Electron microscopic studies of the elastic fiber in human sclera. *Elastic,* 11.

KARSDAL, M. A., DIANA, L. & KIM, H. 2016. *Biochemistry of Collagens, Laminins and Elastin: Structure, Function and Biomarkers*, Academic Press.

KAYA, A. & YILDIRIM, Y. 2016. Posterior scleral thinning accompanies increased vitreous chamber depth in myopia. *Journal of ophthalmic & vision research,* 11**,** 242.

KEELEY, F. W., MORIN, J. D. & VESELY, S. 1984. Characterization of collagen from normal human sclera. *Experimental eye research,* 39**,** 533.

KEENAN, T. D., CLARK, S. J., UNWIN, R. D., RIDGE, L. A., DAY, A. J. & BISHOP, P. N. 2012a. Mapping the differential distribution of proteoglycan core proteins in the adult human retina, choroid, and sclera. *Investigative ophthalmology & visual science,* 53**,** 7528-7538.

KEENAN, T. D., CLARK, S. J., UNWIN, R. D., RIDGE, L. A., DAY, A. J. & BISHOP, P. N. 2012b. Mapping the differential distribution of proteoglycan core proteins in the adult human retina, choroid, and sclera. *Invest Ophthalmol Vis Sci,* 53**,** 7528-38.

KHURSHEED, A. 2007. Scanning electron microscope. Google Patents.

KNEPPER, P. A., GOOSSENS, W., HVIZD, M. & PALMBERG, P. F. 1996. Glycosaminoglycans of the human trabecular meshwork in primary open-

angle glaucoma. *Investigative ophthalmology & visual science,* 37**,** 1360-1367.
KNUDSON, C. B. & KNUDSON, W. Cartilage proteoglycans. Seminars in cell & developmental biology, 2001. Elsevier, 69-78.
KOKOTT, W. 1934. Das spaltlinienbild der sklera.(Ein beitrag zum funktionellen bau der sklera). *Klin. Monatsbl. Augenheilkd,* 92**,** 177-185.
KOMAI, Y. & USHIK, U. 1991. The three-dimensional organization of collagen fibrils in the human cornea and sclera. *Investigative ophthalmology,* 32**,** 2244.
KOMAI, Y. & USHIKIF, T. 2015. The Three-Dimensional Organization of Collagen Fibrils. *Investigative Ophthalmology & Visual Science,* 32**,** 8.
KURYLO, M. P., GRANDFIELD, K., MARSHALL, G. W., ALTOE, V., ALONI, S. & HO, S. P. 2016. Effect of proteoglycans at interfaces as related to location, architecture, and mechanical cues. *Arch Oral Biol,* 63**,** 82-92.
LAGRÈZE, W. A. & SCHAEFFEL, F. 2017. Preventing myopia. *Deutsches Ärzteblatt International,* 114**,** 575.
LARI, D. R., SCHULTZ, D. S., WANG, A. S., LEE, O.-T. & STEWART, J. M. 2012. Scleral mechanics: comparing whole globe inflation and uniaxial testing. *Experimental eye research,* 94**,** 128-135.
LEE, H.-J., CHOI, S., CHEONG, Y., JUNG, G. B., JIN, K.-H., PARK, H.-K. & LEE, S. J. 2011. Effects of Mitomycin C on Scleral Collagen Fibrils According to Atomic Force Microscopy. *Journal of the Korean Ophthalmological Society,* 52**,** 671-678.
MAEDA, N. 2015. Proteoglycans and neuronal migration in the cerebral cortex during development and disease. *Frontiers in neuroscience,* 9**,** 98.
MALOHLAVA, J., ZAPLETALOVA, H., TOMANKOVA, K. & KOLAROVA, H. 2012. Atomic force microscopy: Studying mechanical properties of a cell. *Current microscopy contributions to advances in science and technology. FORMATEX Microscopy Series, Spain***,** 528-532.
MARCUS, M. W., DE VRIES, M. M., MONTOLIO, F. G. J. & JANSONIUS, N. M. 2011. Myopia as a risk factor for open-angle glaucoma: a systematic review and meta-analysis. *Ophthalmology,* 118**,** 1989-1994. e2.
MASSOUDI, D., MALECAZE, F. & GALIACY, S. D. 2015. Collagens and proteoglycans of the cornea: importance in transparency and visual disorders. *Cell Tissue Res*.
MCBRIEN, N. A., CORNELL, L. M. & GENTLE, A. 2001. Structural and Ultrastructural Changes to the Sclera in a Mammalian Model of High Myopia. *Investigative Ophthalmology & Visual Science,* 42.
MCBRIEN, N. A., JOBLING, A. I. & GENTLE, A. 2009. Biomechanics of the sclera in myopia: extracellular and cellular factors. *Optometry and Vision Science,* 86**,** E23-E30.
MCBRIEN, N. A., LAWLOR, P. & GENTLE, A. 2000. Scleral remodeling during the development of and recovery from axial myopia in the tree shrew. *Investigative ophthalmology & visual science,* 41**,** 3713-3719.
MCBRIEN, N. A. N. A., GENTLE, A. A. & MCBRIEN, N. 2003. Role of the sclera in the development and pathological complications of myopia. *Progress in retinal and eye research,* 22**,** 307.
MEEK, K. M. 2008. Cornea and Sclera. *In:* FRATZL, P. (ed.) *Collagen: Structure and Mechanics.* Springer Science & Business Media.

MELLER, D., PETERS, K., MELLER, K., MELLER, D., MELLER, K. & PETERS, K. 1997. Human cornea and sclera studied by atomic force microscopy. *Cell and tissue research,* 288**,** 111.

MEYERS, M. A., CHEN, P.-Y., LIN, A. Y.-M., SEKI, Y., MEYERS, M. A., CHEN, P.-Y., LIN, A. Y.-M. & SEKI, Y. 2008. Biological materials: Structure and mechanical properties. *Progress in Materials Science,* 53**,** 1.

MICHELACCI, Y. M., BIOQUÍMICA, D. D., MEDICINA, E. P. D., PAULO, U. F. D. S. & PAULO, S. 2003. Collagens and proteoglycans of the cornal extracellular matrix. *Brazilian Journal of Medical and Biological Research,* 36.

MURIENNE, B. J., CHEN, M. L., QUIGLEY, H. A. & NGUYEN, T. D. 2016. The contribution of glycosaminoglycans to the mechanical behaviour of the posterior human sclera. *J R Soc Interface,* 13.

MURIENNE, B. J., JEFFERYS, J. L., QUIGLEY, H. A. & NGUYEN, T. D. 2015. The effects of glycosaminoglycan degradation on the mechanical behavior of the posterior porcine sclera. *Acta Biomater,* 12**,** 195-206.

NAYAR, V., WEILAND, J. & HODGE, A. 2011. Characterization of porcine sclera using instrumented nanoindentation. *Materials Science and Engineering: C,* 31**,** 796-800.

NAYAR, V. T., WEILAND, J. D. & HODGE, A. M. 2012. Macrocompression and nanoindentation of soft viscoelastic biological materials. *Tissue Engineering Part C: Methods,* 18**,** 968-975.

NEWTON, R. H. & MEEK, K. M. 1998. Circumcorneal annulus of collagen fibrils in the human limbus. *Investigative ophthalmology & visual science,* 39**,** 1125-1134.

NICOLI, S., FERRARI, G., QUARTA, M., MACALUSO, C., GOVONI, P., DALLATANA, D. & SANTI, P. 2009. Porcine sclera as a model of human sclera for in vitro transport experiments: histology, SEM, and comparative permeability. *Molecular Vision,* 15.

NORTON, T. T. & RADA, J. A. 1995. Reduced extracellular matrix in mammalian sclera with induced myopia. *Vision research,* 35**,** 1271-1281.

ÖBRINK, B. 1973. A study of the interactions between monomeric tropocollagen and glycosaminoglycans. *European journal of biochemistry,* 33**,** 387-400.

OGLESBY, E. N., TEZEL, G., CONE-KIMBALL, E., STEINHART, M. R., JEFFERYS, J., PEASE, M. E. & QUIGLEY, H. A. 2016. <Scleral fibroblast response to experimental glaucoma in mice.pdf>. *Molecular Vision,* 22.

PALKO, J. R., PAN, X. & LIU, J. 2011. Dynamic testing of regional viscoelastic behavior of canine sclera. *Experimental eye research,* 93**,** 825-832.

PAPI, M., PAOLETTI, P., GERAGHTY, B. & AKHTAR, R. 2014. Nanoscale characterization of the biomechanical properties of collagen fibreils in the sclera. 104.

PASCOLINI, D. & MARIOTTI, S. P. 2012. Global estimates of visual impairment: 2010. *British Journal of Ophthalmology,* 96**,** 614-618.

PENG, S. & BHUSHAN, B. 2012. Smart polymer brushes and their emerging applications. *RSC Advances,* 2**,** 8557-8578.

PEREZ, B. C., TANG, J., MORRIS, H. J., PALKO, J. R., PAN, X., HART, R. T. & LIU, J. 2014. Biaxial mechanical testing of posterior sclera using high-

resolution ultrasound speckle tracking for strain measurements. *Journal of biomechanics,* 47**,** 1151-1156.

PETERS, A. E., COMERFORD, E. J., MACAULAY, S., BATES, K. T. & AKHTAR, R. 2017. Micromechanical properties of canine femoral articular cartilage following multiple freeze-thaw cycles. *Journal of the mechanical behavior of biomedical materials,* 71**,** 114-121.

PITTENGER, B., ERINA, N. & SU, C. 2010a. Quantitative mechanical property mapping at the nanoscale with PeakForce QNM. *Application Note Veeco Instruments Inc***,** 1-2.

PITTENGER, B., ERINA, N. & SU, C. 2010b. Quantitative Mechanical Property Mapping at the Nanoscale with PeakForce QNM. *Veeco application note AN128, Rev. A0*.

POGANY, G., HERNANDEZ, D. J. & VOGEL, K. G. 1994. The in vitro interaction of proteoglycans with type 1 collagen is modulated by phosphate. *Archives of biochemistry and biophysics,* 313**,** 102-111.

QUIGLEY, H. A. 1993. Open-angle glaucoma. *New England Journal of Medicine,* 328**,** 1097-1106.

QUIGLEY, H. A., ADDICKS, E. M., GREEN, W. R. & MAUMENEE, A. 1981. Optic nerve damage in human glaucoma: II. The site of injury and susceptibility to damage. *Archives of ophthalmology,* 99**,** 635-649.

QUIGLEY, H. A. & BROMAN, A. T. 2006. The number of people with glaucoma worldwide in 2010 and 2020. *British journal of ophthalmology,* 90**,** 262-267.

QUIGLEY, H. A., HOHMAN, R. M., ADDICKS, E. M., MASSOF, R. W. & GREEN, W. R. 1983. Morphologic changes in the lamina cribrosa correlated with neural loss in open-angle glaucoma. *American journal of ophthalmology,* 95**,** 673-691.

QUINTARELLI, G., DELLOVO, M., BALDUINI, C. & CASTELLANI, A. 1969. The effects of alpha amylase on collagen-proteoglycans and collagen-glycoprotein complexes in connective tissue matrices. *Histochemie,* 18**,** 373-375.

RADA, J. A., ACHEN, V. R., PENUGONDA, S., SCHMIDT, R. W. & MOUNT, B. A. 2000a. Proteoglycan composition in the human sclera during growth and aging. *Investigative ophthalmology & visual science,* 41**,** 1639-1648.

RADA, J. A., ACHEN, V. R., PENUGONDA, S., SCHMIDT, R. W. & MOUNT, B. A. 2015. Proteoglycan Composition in the Human Sclera During Growth and Aging.

RADA, J. A., ACHEN, V. R., PERRY, C. A. & FOX, P. W. 1997. Proteoglycans in the Human Sclera Evidence for the Presence of Aggrecan. *Investigative Ophthalmology & Visual Science,* 38.

RADA, J. A., CORNUET, P. K. & HASSELL, J. R. 1993. Regulation of corneal collagen fibrillogenesis in vitro by corneal proteoglycan (lumican and decorin) core proteins. *Experimental eye research,* 56**,** 635-648.

RADA, J. A., MATTHEWS, A. L., BRENZA, H., RADA, J. A., MATTHEWS, A. L. & BRENZA, H. 1994. Regional Proteoglycan Synthesis in the Sclera of Experimentally Myopic Chicks. *Experimental eye research,* 59**,** 747.

RADA, J. A., NICKLA, D. L. & TROILO, D. 2000b. Decreased proteoglycan synthesis associated with form deprivation myopia in mature primate eyes. *Investigative ophthalmology & visual science,* 41**,** 2050-2058.

RADA, J. A. S., SHELTON, S. & NORTON, T. T. 2006. The sclera and myopia. *Experimental eye research,* 82**,** 185-200.

RASPANTI, M., VIOLA, M., FORLINO, A., TENNI, R., GRUPPI, C. & TIRA, M. E. 2008. Glycosaminoglycans show a specific periodic interaction with type I collagen fibrils. *Journal of structural biology,* 164**,** 134-139.

ROBINSON, K. A., SUN, M., BARNUM, C. E., WEISS, S. N., HUEGEL, J., SHETYE, S. S., LIN, L., SAEZ, D., ADAMS, S. M., IOZZO, R. V., SOSLOWSKY, L. J. & BIRK, D. E. 2017. Decorin and biglycan are necessary for maintaining collagen fibril structure, fiber realignment, and mechanical properties of mature tendons. *Matrix Biol,* 64**,** 81-93.

ROUGHLEY, P. J. & MORT, J. S. 2014. The role of aggrecan in normal and osteoarthritic cartilage. *Journal of experimental orthopaedics,* 1**,** 8.

RUSSELL, P., BATCHELOR, D. & THORNTON, J. 2001. SEM and AFM: complementary techniques for high resolution surface investigations. *Veeco Instruments Inc., AN46, Rev A,* 1**,** 2004.

RUSSELL, R., SWEDA, J. R., PORCHERON, A. & MAUGER, E. 2014. Sclera color changes with age and is a cue for perceiving age, health, and beauty. *Psychology and aging,* 29**,** 626.

SCHMIDT, M. B., MOW, V. C., CHUN, L. E. & EYRE, D. R. 1990. Effects of proteoglycan extraction on the tensile behavior of articular cartilage. *Journal of Orthopaedic Research,* 8**,** 353-363.

SCOTT, J. E. 1988. Proteoglycan-fibrillar collagen interactions. *The Biochemical journal,* 252**,** 313-323.

SCOTT, J. E. & BOSWORTH, T. R. 1990. A comparative biochemical and ultrastructural study of proteoglycan-collagen interactions in corneal stroma. Functional and metabolic implications. *Biochemical Journal,* 270**,** 491.

SHOULDERS, M. D. & RAINES, R. T. 2009. Collagen structure and stability. *Annu Rev Biochem,* 78**,** 929-58.

SIEGWART JR, J. T. & NORTON, T. T. 1999. Regulation of the mechanical properties of tree shrew sclera by the visual environment. *Vision research,* 39**,** 387-407.

SIGMA-ALDRICH 2000. *Glycobiology Analysis Manual, 2nd Edition*, Sigma Life Science.

SNEDDON, I. N. 1965. The relation between load and penetration in the axisymmetric Boussinesq problem for a punch of arbitrary profile. *International journal of engineering science,* 3**,** 47-57.

SPITZNAS, M. & HOGAN, M. J. 1970. Outer segments of photoreceptors and the retinal pigment epithelium: interrelationship in the human eye. *Archives of Ophthalmology,* 84**,** 810-819.

SPITZNAS, M., LUCIANO, L. & REALE, E. 1970. Fine structure of rabbit scleral collagen. *American journal of ophthalmology,* 69**,** 414-418.

SPITZNER, E.-C., PER, S. R., ZERSON, M., BERNSTEIN, A. & MAGERLE, R. 2015. Nanoscale Swelling Heterogeneities in Type I Collagen Fibrils. *ACS Nano,* 9.

SPOERL, E., TERAI, N., RAISKUP, F. & PILLUNAT, L. E. 2012. Amylase Reduces The Biomechanical Stiffness Of The Cornea. *Investigative Ophthalmology & Visual Science,* 53**,** 1531-1531.

SUMMERS RADA, J. A., SHELTON, S., NORTON, T. T., SUMMERS RADA, J. A., SHELTON, S. & NORTON, T. T. 2006. The sclera and myopia. *Experimental eye research,* 82**,** 185.

SWEERS, K., VAN DER WERF, K., BENNINK, M. & SUBRAMANIAM, V. 2011. Nanomechanical properties of α-synuclein amyloid fibrils: a comparative study by nanoindentation, harmonic force microscopy, and Peakforce QNM. *Nanoscale research letters,* 6**,** 270.

TIELSCH, J. M., SOMMER, A., KATZ, J., ROYALL, R. M., QUIGLEY, H. A. & JAVITT, J. 1991. Racial variations in the prevalence of primary open-angle glaucoma: the Baltimore Eye Survey. *Jama,* 266**,** 369-374.

TIMOTHY, W. O., SCOTT, S., XIAO, F. & WILLIAM, C. H. 2002. Porcine Sclera: Thickness and Surface Area. *Investigative ophthalmology & visual science,* 43**,** 2529-2532.

TRIER, K., OLSEN, E. B. & AMMITZBØLL, T. 1990. Regional glycosaminoglycans composition of the human sclera. *Acta ophthalmologica,* 68**,** 304-306.

VAN HAERINGEN, N., ENSINK, F. & GLASIUS, E. 1975. Amylase in human tear fluid: origin and characteristics, compared with salivary and urinary amylases. *Experimental eye research,* 21**,** 395-403.

VARKI, A., CUMMINGS, R. D., ESKO, J. D., FREEZE, H. H., STANLEY, P., MARTH, J. D., BERTOZZI, C. R., HART, G. W. & ETZLER, M. E. 2009. Symbol nomenclature for glycan representation. *Proteomics,* 9**,** 5398-5399.

VOGEL, K. G., PAULSSON, M. & HEINEGÅRD, D. 1984. Specific inhibition of type I and type II collagen fibrillogenesis by the small proteoglycan of tendon. *Biochemical Journal,* 223**,** 587-597.

WANG, X., HUANG, Y., JASTANEIAH, S., MAJUMDAR, S., KANG, J. U., YIU, S. C., STARK, W. & ELISSEEFF, J. H. 2015. Protective Effects of Soluble Collagen during Ultraviolet-A Crosslinking on Enzyme-Mediated Corneal Ectatic Models. *PLoS One,* 10**,** e0136999.

WATANABE, Y., KOMATSU, K., WATANABE, Y. & KOMATSU, K. 1997. Biomechanical and Morphological Studies on the Periodontal Ligament of the Rat Molar after Treatment with α-amylase in vitro. *Connective tissue research,* 36**,** 35.

WATSON, P. & HAZLEMAN, B. 2012a. *the sclera and systemic disorders*, JP Medic

al Ltd.

WATSON, P. G. & HAZLEMAN, B. L. 2012b. *The sclera and systemic disorders*, JP Medical Ltd.

WATSON, P. G. & YOUNG, R. D. 2004. Scleral structure, organisation and disease. A review. *Experimental Eye Research,* 78**,** 609-623.

WEIYI, C., WANG, X., WANG, C., TAO, L., LI, X. & ZHANG, Q. 2008. An experimental study on collagen content and biomechanical properties of sclera after posterior sclera reinforcement. *Clinical Biomechanics,* 23**,** S17-S20.

WILLIAMS, D. B. & CARTER, C. B. 1996. The transmission electron microscope. *Transmission electron microscopy.* Springer.

WOLFF, E. 1997. The conjunctiva, The ocular appendages: eyelids, conjunctiva and lacrimal apparatus. *Wolff's Anatomy of the Eye and Orbit Eighth edition***,** 51-70.

WOLLENSAK, G., SPORL, E., MAZZOTTA, C., KALINSKI, T. & SEL, S. 2011. Interlamellar cohesion after corneal crosslinking using riboflavin and ultraviolet A light. *Br J Ophthalmol,* 95**,** 876-80.

WOLLENSAK, G., WILSCH, M., SPOERL, E. & SEILER, T. 2004. Collagen Fiber Diameter in the Rabbit Cornea After Collagen Crosslinking by Riboflavin/UVA. *Cornea,* 23.

YAMAMOTO, S., HASHIZUME, H., HITOMI, J., SHIGENO, M., SAWAGUCHI, S., ABE, H. & USHIKI, T. 2000. The subfibrillar arrangement of corneal and scleral collagen fibrils as revealed by scanning electron and atomic force microscopy. *Archives of histology and cytology,* 63**,** 127-135.

YAMAMOTO, S., HITOMI, J., SAWAGUCHI, S., ABE, H., SHIGENO, M. & USHIKI, T. 2002. Observation of human corneal and scleral collagen fibrils by atomic force microscopy. *Japanese journal of ophthalmology,* 46**,** 496-501.

YANG, W., SHERMAN, V. R., GLUDOVATZ, B., SCHAIBLE, E., STEWART, P., RITCHIE, R. O. & MEYERS, M. A. 2015. On the tear resistance of skin. *Nat Commun,* 6**,** 6649.

YOUNG, R. D. 1985a. The ultrastructural organization of proteoglycans and collagen in human and rabbit scleral matrix. *Journal of cell science,* 74**,** 95-104.

YOUNG, R. D. 1985b. The ultrastructural organization of proteoglycans and collagen in human and rabbit scleral matrix. *Journal of cell science,* 74**,** 95-104.

YOUNG, T. J., MONCLUS, M. A., BURNETT, T. L., BROUGHTON, W. R., OGIN, S. L. & SMITH, P. A. 2011. The use of the PeakForce^{TM} quantitative nanomechanical mapping AFM-based method for high-resolution Young's modulus measurement of polymers. *Measurement Science & Technology,* 22**,** 125703.

YOUNG, T. L., GUO, X. D., KING, R. A., JOHNSON, J. M. & RADA, J. A. 2003. Identification of genes expressed in a human scleral cDNA library. *Mol Vis,* 9**,** 508-514.

ZHANG, Y., LI, Z., LIU, L., HAN, X., ZHAO, X. & MU, G. 2014. Comparison of riboflavin/ultraviolet-A cross-linking in porcine, rabbit, and human sclera. *BioMed research international,* 2014.

Appendix A

Experimental setup and protocols

SDS-PAGE Loading and running buffer

2x Loading sample buffer (10ml)

1 M Tris-HCl pH 6.8	1 ml
10% SDS	4 ml
Glycerol	2 ml
β-mercaptoethanol	2.5 ml
1% Bromophenol blue	500 µl
dH_2O	to10 ml

4x Loading sample buffer (10ml)

1 M Tris-HCl pH6. 8	2 ml
SDS	0.8 g
Glycero	l 4 ml
β-mercaptoethanol	4 ml
10% Bromophenol blue	10 µl

10 × Running buffer

Tris base	30.3 g
Glycine	144.4 g

SDS 10 g

Dissolve in 1 L of MilliQ-filtered H_2O.

Papain Digestion

Papain Enzyme stock (Papain: Sigma P4762):

Make 10× stock enzyme solution at 100 units/ml. This will make the final working concentration for the digest at 10 unit/ml. Make enzyme stock up in 10× papain buffer.

10× papain buffer

1M Sodium Acetate (1.36g)
24mM EDTA (0.48ml OF 0.5M stock)
50Mm L-cysteine (87.8mg)
PH 5.8

Working Enzyme Solution (1×)

To make 1ml of working enzyme solution = 100µl stock enzyme (10×) + 900µ water

Add 500µl of diluted 1 × papain (or enough to cover sample completely) and incubate overnight at 60^{o}C (or until the tissue is completely digested). Store digests at -20^{o}C

GAG ASSAY

Preparation of the standard curve:

Use 5mg/ml Chondroitin Sulphate C (shark cartilage, Sigma C-4384) as a stock solution (made up in water) from which to make the standards. Then further dilute 50 x to give 100 ug/ml.

Standard Conc (ug/ml)	Vol. 100ug/ml stock to add (ul)	Vol. H_2O to add (ul)
0	0	1000
10	100	900
20	200	800
30	300	700
40	400	600
50	500	500
60	600	400
70	700	300

Use a transparent flat bottomed 96 well plate and add 40 ul standard to appropriate wells (perform in triplicate)

Dilute papain digested sclera samples 1 in 5 with water to make a total volume of 40 ul. Apply diluted sample to appropriate wells and again perform in triplicate.

Add 250ul DMMB dye to each well.

Read immediately on a plate reader at an absorbance of 570mm (the dye-GAG complex will precipitate out of solution if left too long).

DMMB (light sensitive)

16mg 1-9 dimethyl methylene blue
2g sodium formate
2ml formic acid
In 1 litre water
pH = 3.5

Pilot study for experimental setup

AFM sample thickness result from testing sclera tissue in air with PeakForce QNM

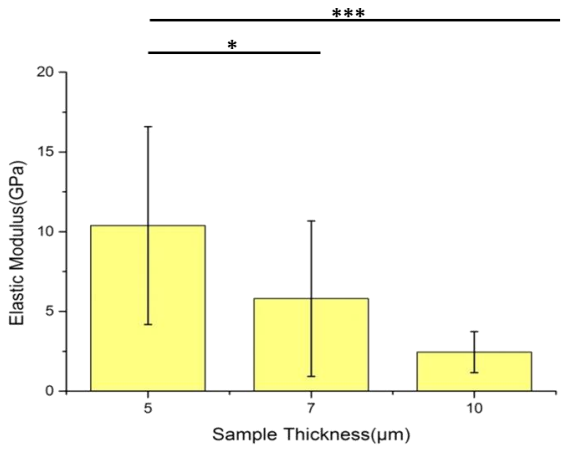

Elastic modulus of samples with different thickness.

- The elastic modulus decreased in sample with thickness of 7 μm (≈4.35 GPa) and 10 μm (≈ 7.50 GPa)

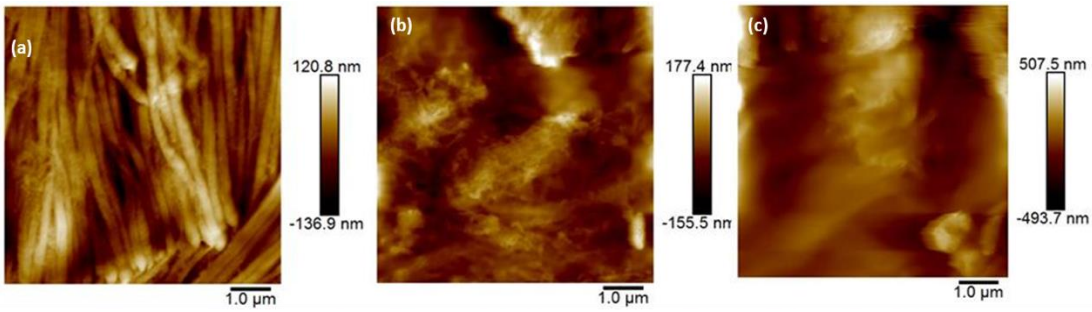

Image qualities became low while sample thickness increased.5µm (a), 7µm (b) and 10µm (c)

Chondroitinase ABC activities

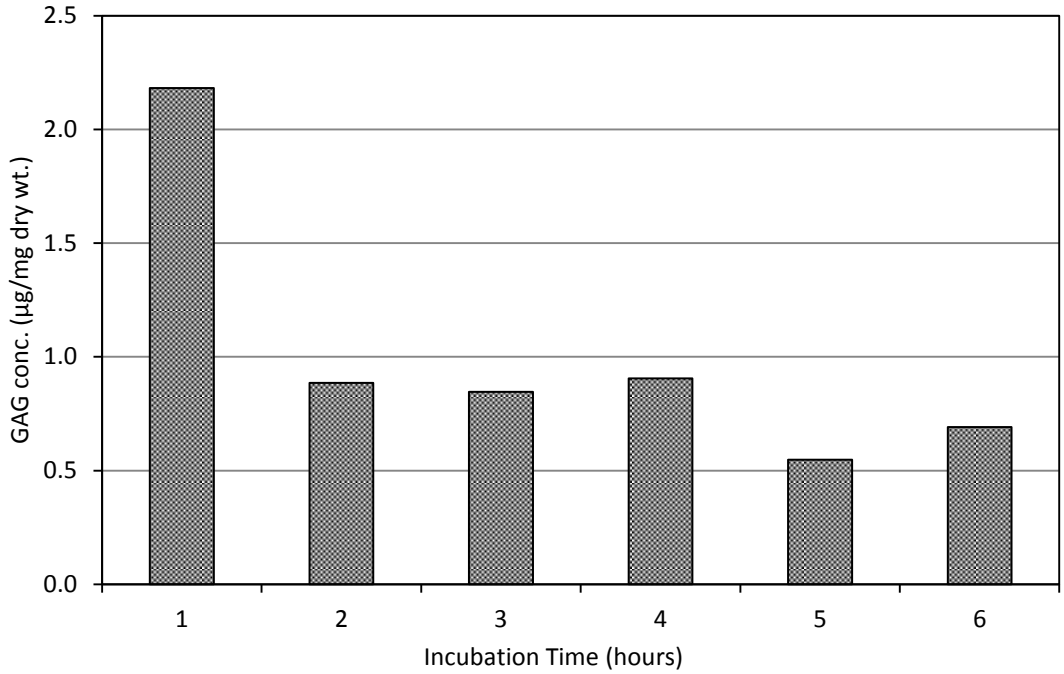

From previous study by Miss Charlotte Li (BBSRC Funded Summer Project, supervised by Prof. Eithne Comerford and Dr Brendan Geraghty, University of Liverpool), using 0.25 unit/m for scleral proteoglycan depletion in 37°C environment. the incubated results show a decrease in GAG concentration within the first 2 hours (roughly 60%), followed by little change in concentration.

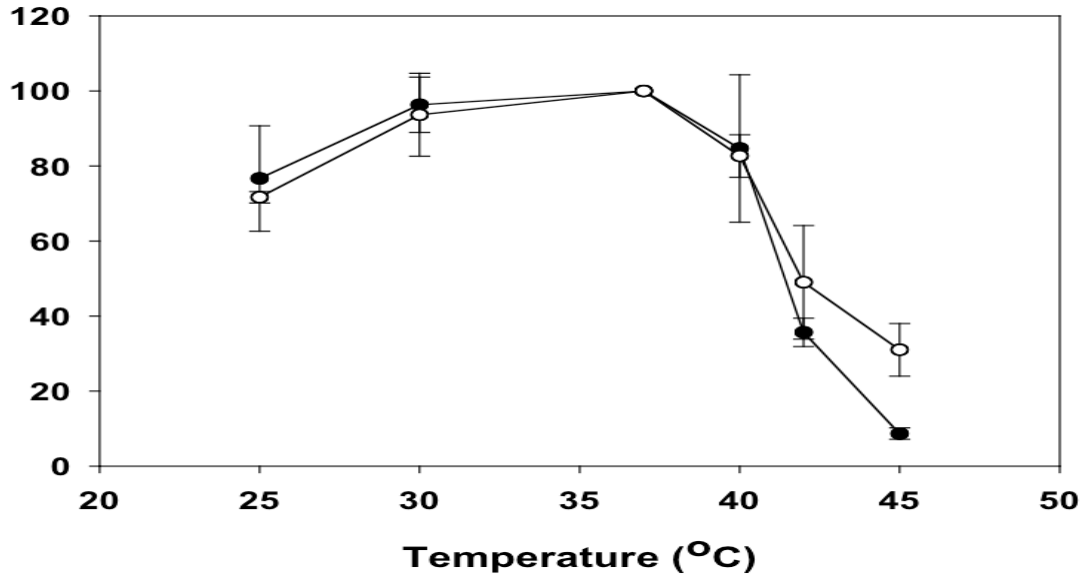

Chondroitinase ABC II Biochemical Reaction Conditions. Effect of reaction temperature effect using sodium acetate titration. For all panels:, C6S; , DS. (activity curve from Sigma for enzyme chondroitinase ABC : C2905, Sigma-Aldrich, St. Louis MO)

Drawings for nanoindentation sample holder

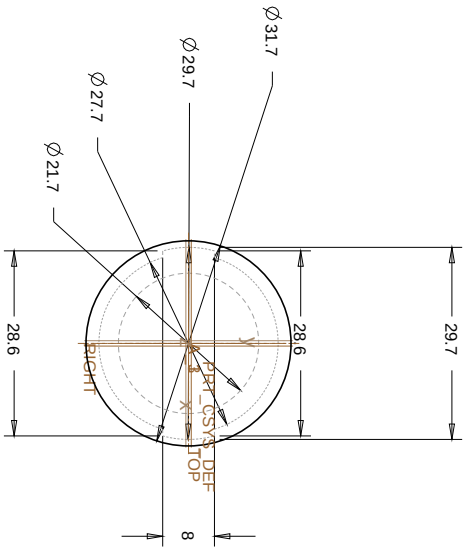

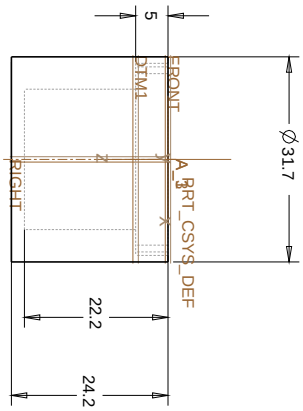

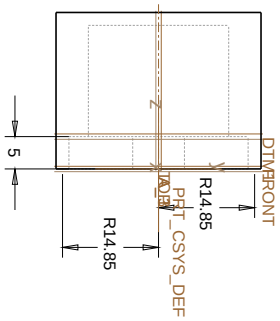

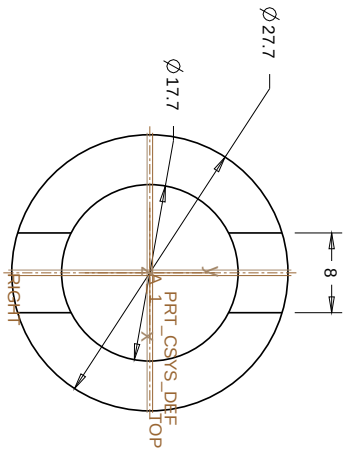
Ø 27.7
Ø 17.7
8
PRT_CSYS_DEF
TOP
RIGHT

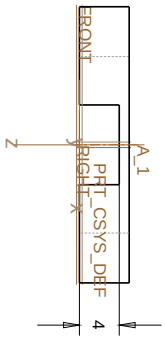
FRONT
A_1
PRT_CSYS_DEF
RIGHT
4

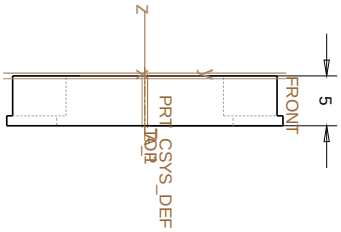
5
FRONT
PRT_CSYS_DEF
TOP

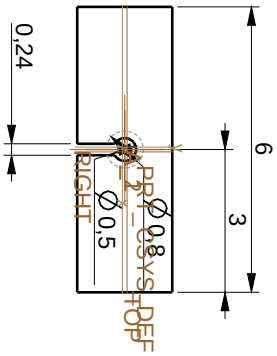
0,24
6
3
Ø0,5
Ø0,8
RIGHT
PRT_CSYS_DEF
FRONT

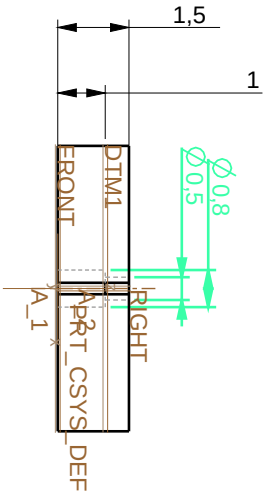
1,5
1
Ø0,8
Ø0,5
DTM1
FRONT
RIGHT
A_1
A_2
PRT_CSYS_DEF

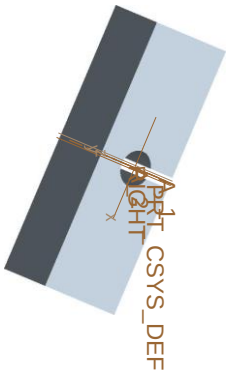
A_1
A_2
RIGHT
PRT_CSYS_DEF

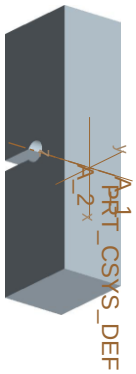
A_1
A_2
PRT_CSYS_DEF

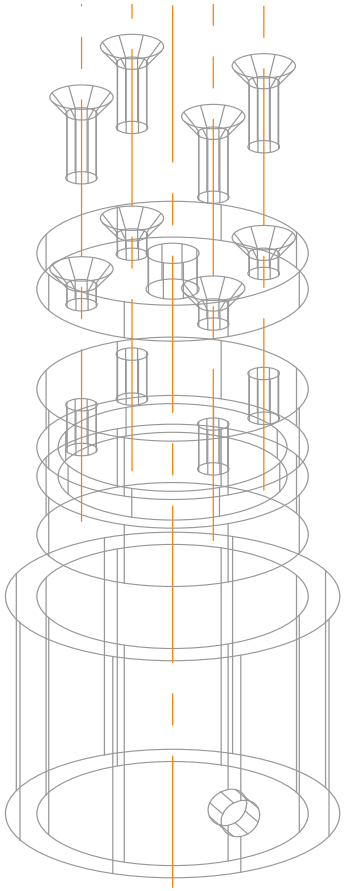

Assembly drawing:
Scale 2:1

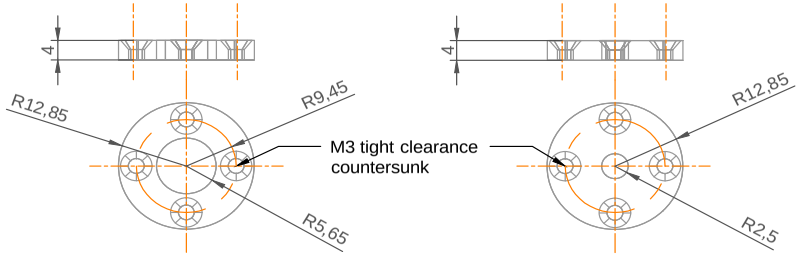

Cover no. 1

Cover no. 2

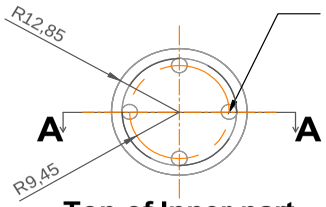

Top of Inner part

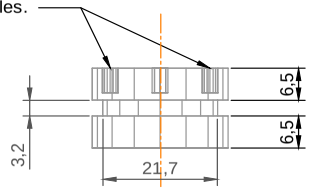

Inner part
cross section (A-A)

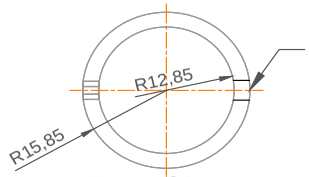

Top of base

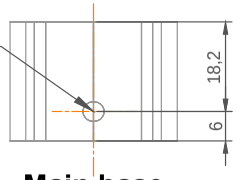

Main base

Component drawing: Scale
Material - Stainless steel

Appendix B

Codings for Image processing

Matlab code

Testing point localization

```
% Demo to use normxcorr2 to find a template (a white
onion)
% in a larger image (of a pile of vegetables)
clc;    % Clear the command window.
close all;  % Close all figures (except those of
imtool.)
imtool close all;  % Close all imtool figures.
clear;  % Erase all existing variables.
workspace;  % Make sure the workspace panel is
showing.
format long g;
format compact;
fontSize = 11;

% Check that user has the Image Processing Toolbox
installed.
hasIPT = license('test', 'image_toolbox');
if ~hasIPT
    % User does not have the toolbox installed.
    message = sprintf('Sorry, but you do not seem to
have the Image Processing Toolbox.\nDo you want to
try to continue anyway?');
    reply = questdlg(message, 'Toolbox missing',
'Yes', 'No', 'Yes');
    if strcmpi(reply, 'No')
        % User said No, so exit.
        return;
    end
end

% Read in a standard MATLAB color demo image.
```

```
folder = fullfile(matlabroot,
'\toolbox\images\imdemos');
baseFileName = 'peppers.png´;
% Get the full filename, with path prepended.
fullFileName = fullfile(folder, baseFileName);
if ~exist(fullFileName, 'file')
    % Didn't find it there.  Check the search path
for it.
    fullFileName = baseFileName; % No path this time.
    if ~exist(fullFileName, 'file')
        % Still didn't find it.  Alert user.
        errorMessage = sprintf('Error: %s does not
exist.', fullFileName);
        uiwait(warndlg(errorMessage));
        return;
    end
end
rgbImage = imread(fullFileName);
% Get the dimensions of the image.
numberOfColorBands should be = 3.
[rows, columns, numberOfColorBands] = size(rgbImage);
% Display the original color image.
subplot(2, 2, 1);
imshow(rgbImage, []);
axis on;
caption = sprintf('Original Color Image, %d rows
by %d columns.', rows, columns);
title(caption, 'FontSize', fontSize);
% Enlarge figure to full screen.
set(gcf, 'units','normalized','outerposition',[0, 0,
1, 1]);

% Let's get our template by extracting a small
portion of the original image.
templateWidth = 71
templateHeight = 49
smallSubImage = imcrop(rgbImage, [192, 82,
templateWidth, templateHeight]);
% Get the dimensions of the image.
numberOfColorBands should be = 3.
[rows, columns, numberOfColorBands] =
size(smallSubImage);
subplot(2, 2, 2);
imshow(smallSubImage, []);
axis on;
```

```
caption = sprintf('Template Image to Search For, %d
rows by %d columns.', rows, columns);
title(caption, 'FontSize', fontSize);

% Ask user which channel (red, green, or blue) to
search for a match.
% channelToCorrelate = menu('Correlate which color
channel?', 'Red', 'Green', 'Blue');
% It actually finds the same location no matter what
channel you pick,
% for this image anyway, so let's just go with red
(channel #1).
% Note: If you want, you can get the template from
every color channel and search for it in every color
channel,
% then take the average of the found locations to
get the overall best location.
channelToCorrelate = 1;  % Use the red channel.
correlationOutput = normxcorr2(smallSubImage(:,:,1),
rgbImage(:,:, channelToCorrelate));
subplot(2, 2, 3);
imshow(correlationOutput, []);
axis on;
% Get the dimensions of the image.
numberOfColorBands should be = 1.
[rows, columns, numberOfColorBands] =
size(correlationOutput);
caption = sprintf('Normalized Cross Correlation
Output, %d rows by %d columns.', rows, columns);
title(caption, 'FontSize', fontSize);

% Find out where the normalized cross correlation
image is brightest.
[maxCorrValue, maxIndex] =
max(abs(correlationOutput(:)));
[yPeak, xPeak] =
ind2sub(size(correlationOutput),maxIndex(1))
% Because cross correlation increases the size of
the image,
% we need to shift back to find out where it would
be in the original image.
corr_offset = [(xPeak-size(smallSubImage,2)) (yPeak-
size(smallSubImage,1))]

% Plot it over the original image.
```

```
subplot(2, 2, 4); % Re-display image in lower right.
imshow(rgbImage);
axis on; % Show tick marks giving pixels
hold on; % Don't allow rectangle to blow away image.
% Calculate the rectangle for the template box.
Rect = [xLeft, yTop, widthInColumns, heightInRows]
boxRect = [corr_offset(1) corr_offset(2)
templateWidth, templateHeight]
% Plot the box over the image.
rectangle('position', boxRect, 'edgecolor', 'G´,
'linewidth',2);
% Give a caption above the image.
title('Template Image Found in Original Image',
'FontSize', fontSize);
uiwait(helpdlg('Done with demo!'));
```

Gap zone and approximate D-periodicity measurement

```
%data = xlread('testing.xlsx');
%
%
%Enroll database.
%Each database content values of one hydration/
depletion experiment
%The odd column is x vules and the even columnis the
y valus of curve.
data= Book1;
GAPnm = [];
PERInm = [];
n = size (data,2)/2;
for i = 1:n
fibril = [data{:,2*i-1}];
hi = [data{:,2*i}];
org= plot(fibril,hi);
[pks,locs] = findpeaks(hi,'MinPeakdistance',20);
%findpeaks(hi)
plot(fibril,hi,'color',rand(1,3)); hold on;
% offset values of peak heights for plotting
plot(fibril(locs),pks+0.05,'r*','markerfacecolor',[0
1 1]);
locpeak = fibril(locs);
aveperium = mean(diff(locpeak))*1000;
rhi = -hi;
```

```
[rpks,rlocs] = findpeaks(rhi,'MinPeakdistance',20);
% offset values of peak heights for plotting
rpks= rpks*-1;
plot(fibril(rlocs),rpks+0.05,'k*','markerfacecolor',
[1 0 1]);
%
%
%start to caululate collagen fibril gaps between
peak and minum value
Gap= [];
if size(pks,2) <= size(rpks,2)
    m = size (pks,2)-1;
else
    m = size (rpks,2)-1;
end

for j=1:m
    gap= pks(1,j)-rpks(1,j);
    Gap = [Gap gap];
end
avgapnm= mean(Gap);
PERInm = [PERInm;aveperium];
GAPnm = [GAPnm;avgapnm];

end
```

Collagen fibrils orientation measurement

```
 clear all
close
% Hough test
peakpionts=50
I=imread('Untitled 2.jpg');
I=rgb2gray(I);% gray
I=edge(I,'prewitt');
figure(1)
imshow (I);title('The Original image')

I=im2bw(I);
[H, theta, rho] = hough(I, 'ThetaResolution', 0.2);
figure(2)
imshow(H, [], 'XData', theta, 'YData', rho,
'InitialMagnification', 'fit')
axis on, axis normal
hold on
```

```
xlabel('\theta'), ylabel('\rho')
peaks = houghpeaks(H,peakpionts);
plot(theta(peaks(:, 2)), rho(peaks(:, 1)), ...
    'linestyle', 'none', 'marker', 's', 'color', 'r')
title('The peak point location')
lines = houghlines(I, theta, rho, peaks);
figure(3)
imshow(I), hold on
for k = 1:length(lines)
    xy=[lines(k).point1 ; lines(k).point2];
    plot(xy(:,1), xy(:,2), 'LineWidth', 4, 'Color',
[1 0 0]);
    slope(k)=(xy(1,2)-xy(2,2))./(xy(1,1)-xy(2,1));
    angle(k)=atan(slope(k)).*180/pi;
end
title('Hough-transformation result')

%ans=theta(peaks(:, 2))

I=imread('Untitled 2.jpg);
B=fft(I);
figure()
imshow(B)
```

ImageSXM macro

macro 'Measurement of periodicity and diameter 27'

{ edited SDB 11 Mar 2017 }

{01} var

{02}   xxx,yyy,x,mode,mean,min, max, ThisPic: real;

{03} result,name: string;

{04} n: integer;

{05} begin

```
{06}    UnsharpMask('11x11');
{07}   Measure;
{08}    GetResults(n, mean, mode, min ,max);
{09}    SetThreshold(mode);
{10}    MakeBinary;
{11}    SetBinaryCount(2);
{12}    Dilate;
{13}    Erode;
{14}    Dilate;
{15}    Erode;
{16}    Dilate;
{17}    Erode;
{18}    Dilate;
{19}    Erode;
{20}    Dilate;
{21}    Erode;
{22}    Skeletonize;
{23}    SetPicName('ske');
{24}    SelectAll;
{25}    Copy;
{26}    MoveRoi(1,0);
{27}    Paste;
{28}
{29}    MakeNewWindow('new',256,256); {make a new window}
{30}    Paste;
{31}    SetPicName('new');
```

```
{32}     SelectPic(2);

{33}     xxx:=PicNumber;

{34}    SelectPic(3);

{35}    yyy:=PicNumber;

{36}    result := 'ads';

{37}    ImageMath('or',xxx,yyy,1,0,result);

{38}    Invert;

{39}    SetForegroundColor(255);    { make border black so that it touches ... }

{40}    SetLineWidth(1);                    { all objects truncated by the border }

{41}    DrawBoundary;

{42}    KillRoi;

{43}    SetForegroundColor(0);

{44}     AutoOutline(1, 128);     { copy all objects other than those touching
edge }

{45}    Copy;

{46}    SelectAll;

{47}    Clear;              { clear the whole image... }

{48}    Paste;              { and then put objects back }

{49}    KillRoi;

{50}    SetParticleSize(1,200);

{51}    AnalyzeParticles('label','reset','ignore');
{52}   ShowResults;

{53} end;
```

Appendix C

AFM Images

Images of proteoglycan

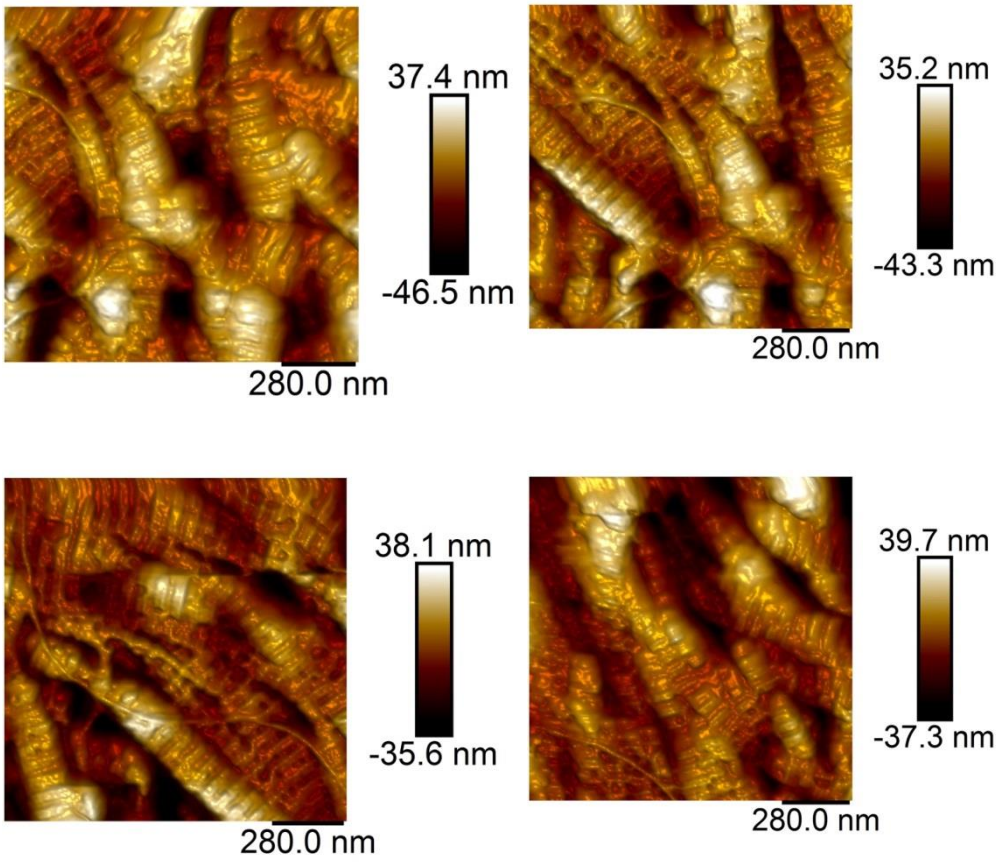

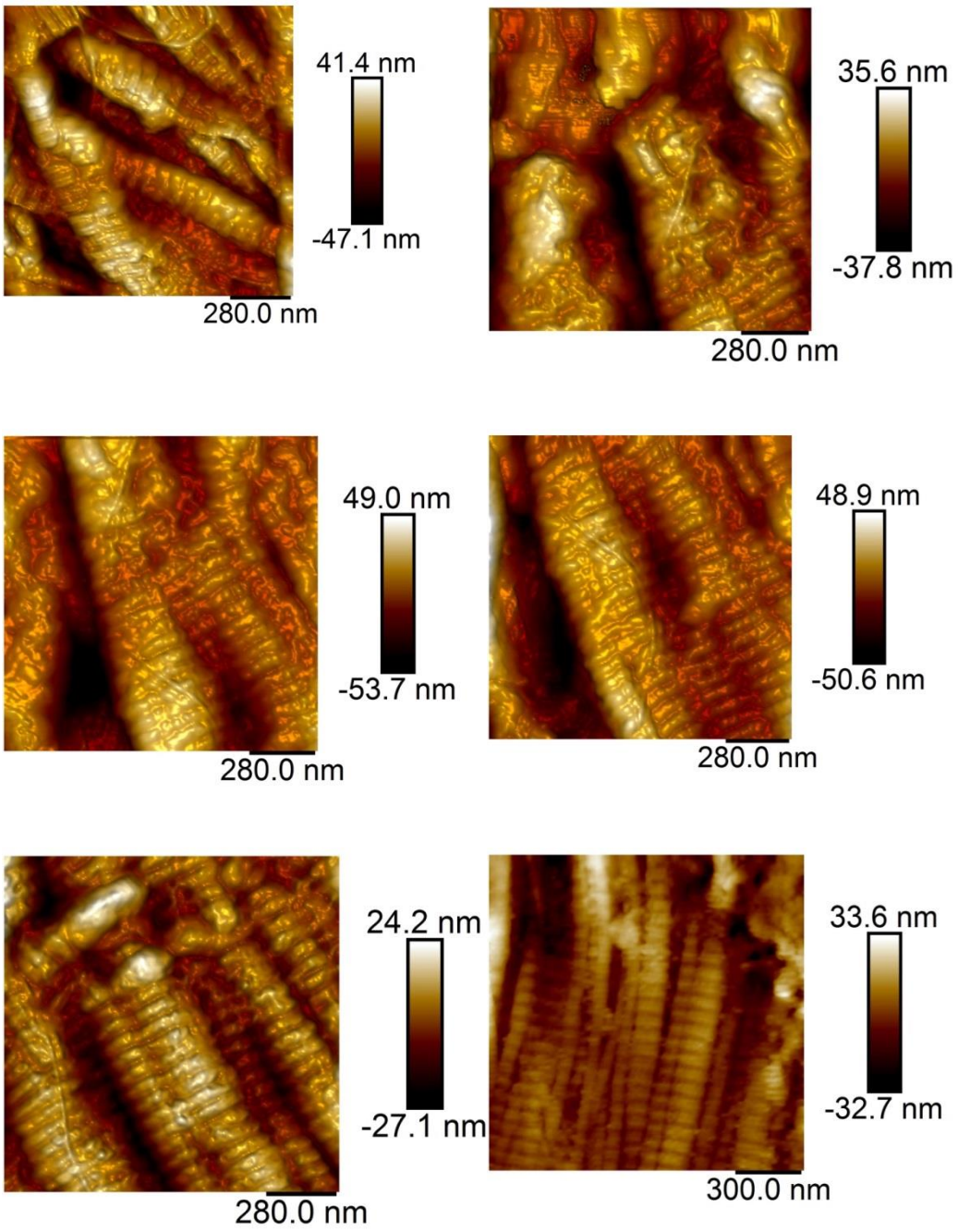
41.4 nm
-47.1 nm
280.0 nm
35.6 nm
-37.8 nm
280.0 nm
49.0 nm
-53.7 nm
280.0 nm
48.9 nm
-50.6 nm
280.0 nm
24.2 nm
-27.1 nm
280.0 nm
33.6 nm
-32.7 nm
300.0 nm

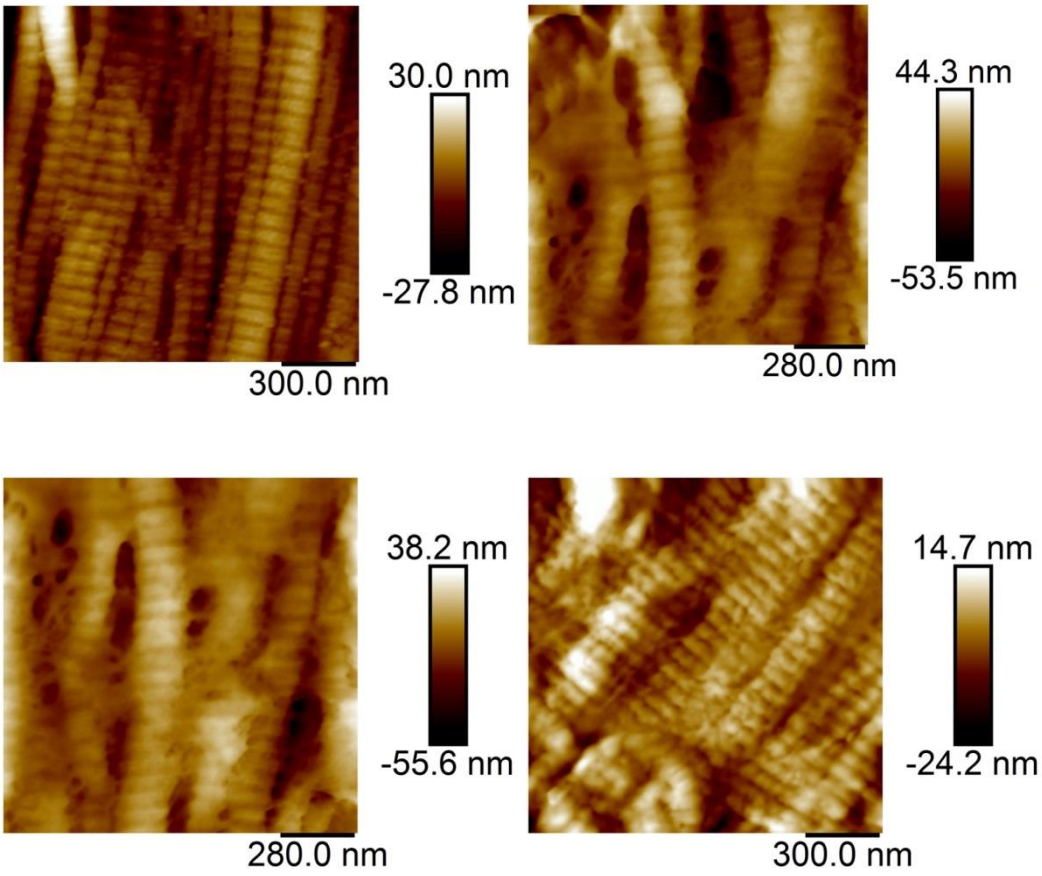

Images of collagen fibrils "fusion" after Amylase treatment.

Pre Amylase treatment	Post Amylase treatment
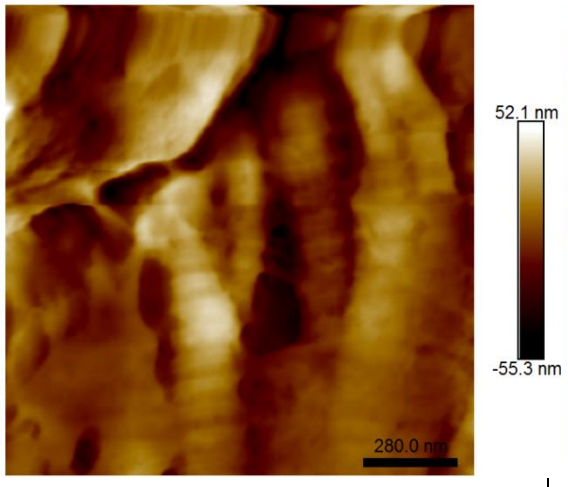	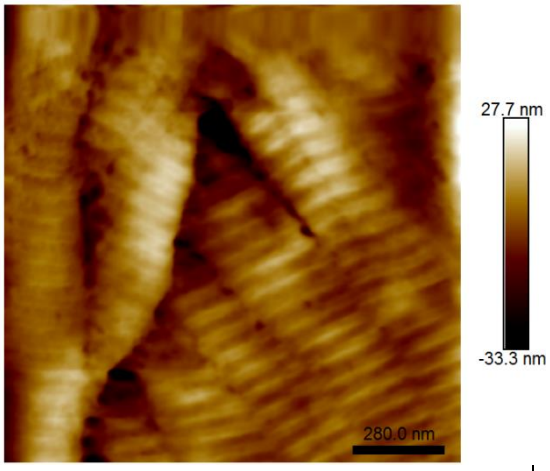

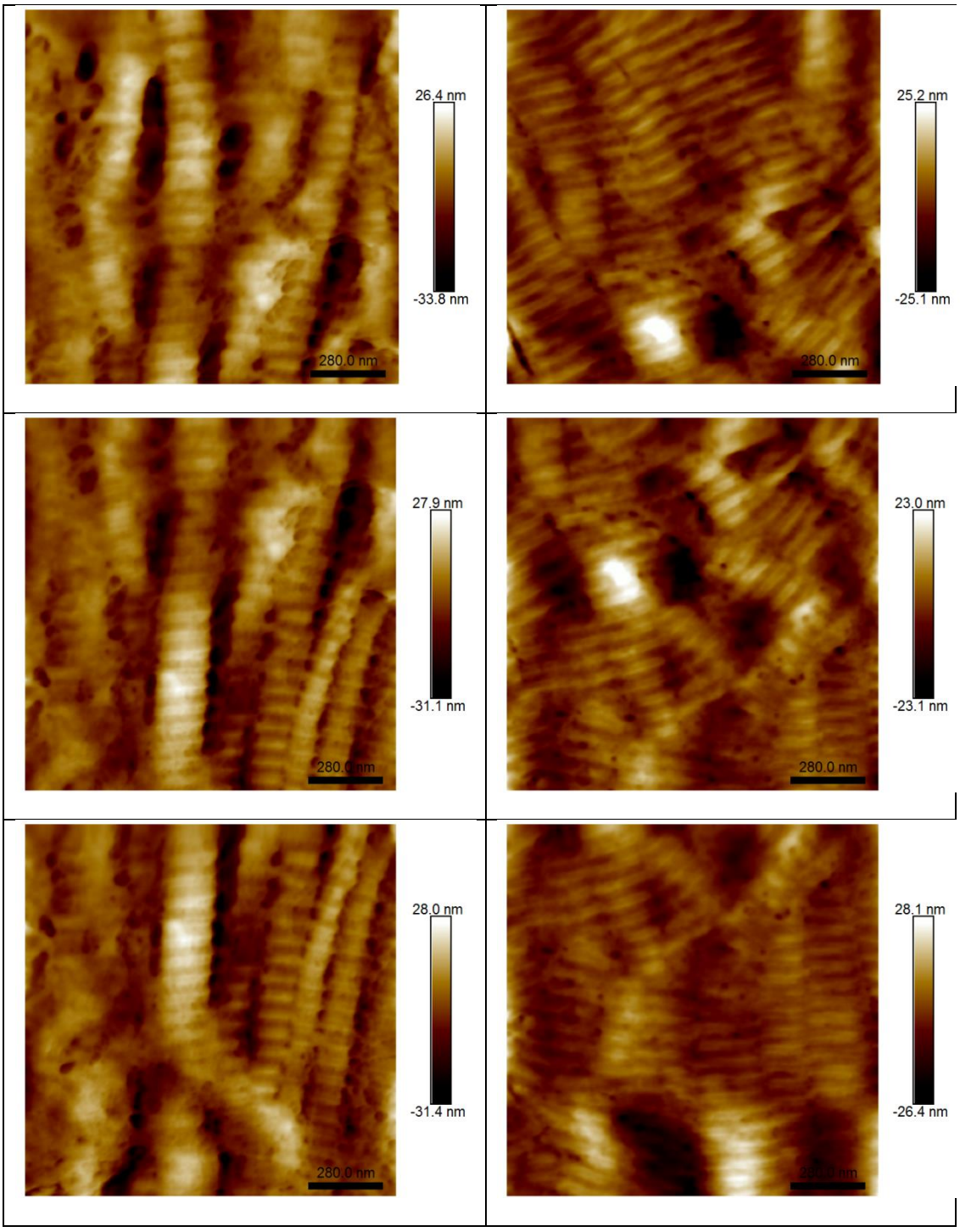
26.4 nm
-33.8 nm
280.0 nm
25.2 nm
-25.1 nm
280.0 nm
27.9 nm
-31.1 nm
280.0 nm
23.0 nm
-23.1 nm
280.0 nm
28.0 nm
-31.4 nm
280.0 nm
28.1 nm
-26.4 nm

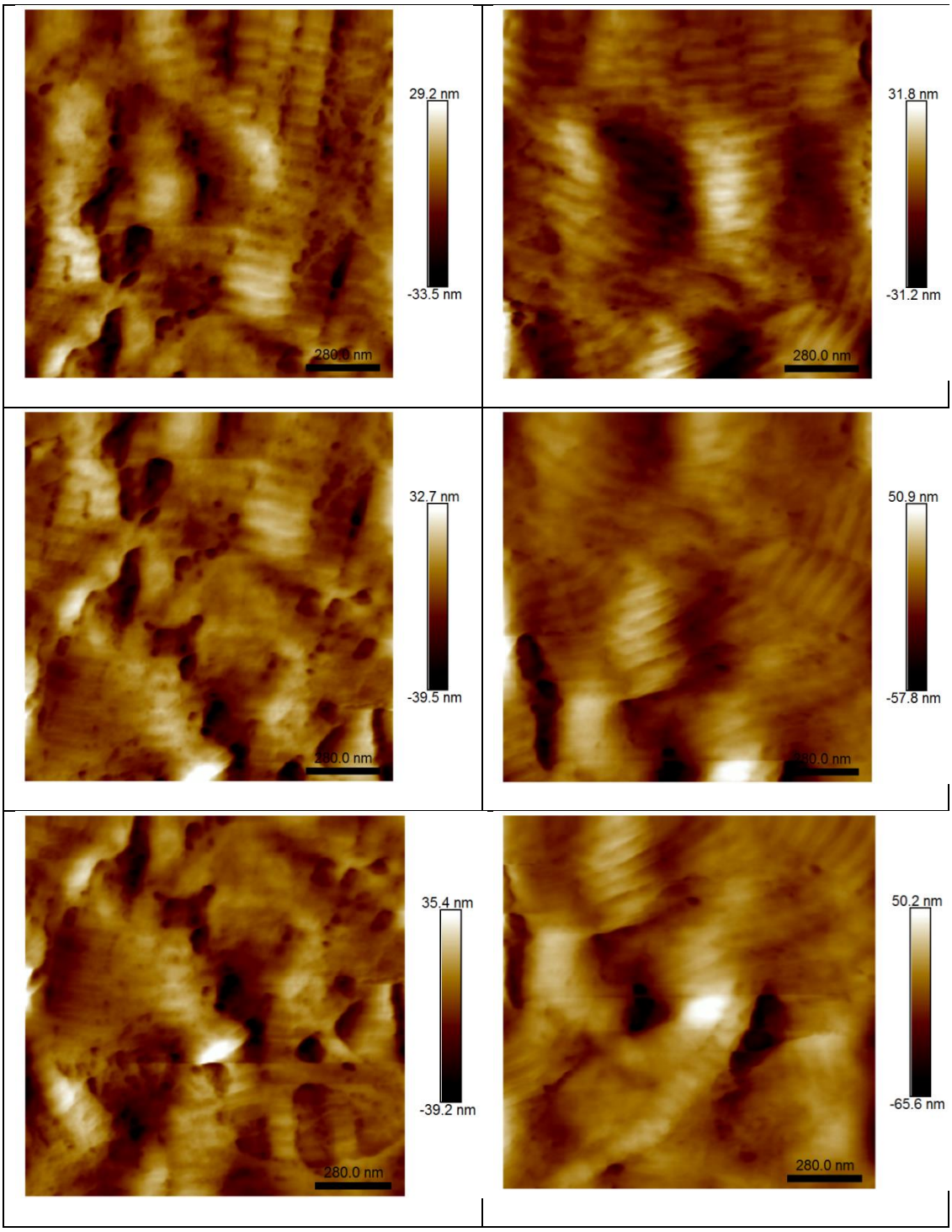
29.2 nm
-33.5 nm
280.0 nm
31.8 nm
-31.2 nm
280.0 nm
32.7 nm
-39.5 nm
280.0 nm
50.9 nm
-57.8 nm
35.4 nm
-39.2 nm
280.0 nm
50.2 nm
-65.6 nm
280.0 nm

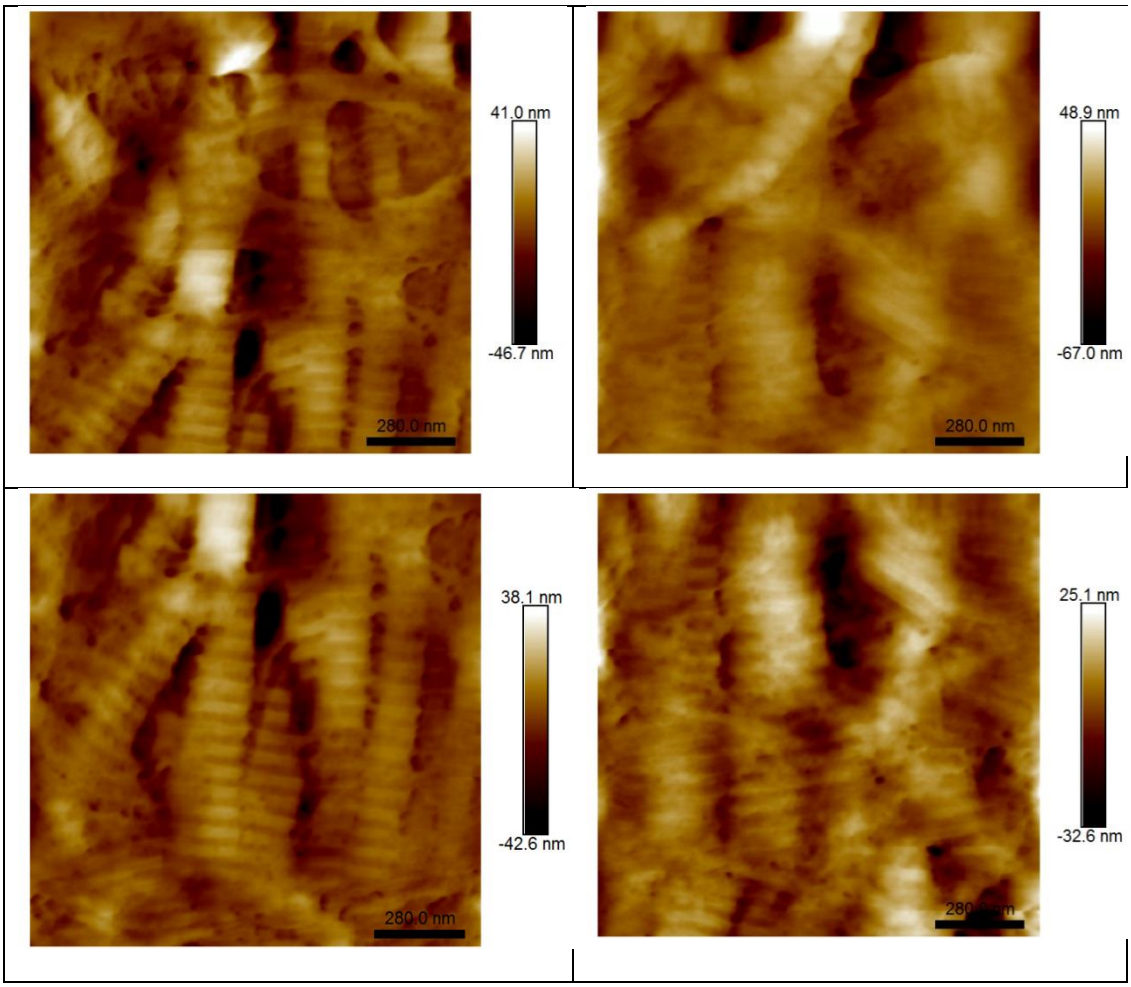
41.0 nm
-46.7 nm
280.0 nm
48.9 nm
-67.0 nm
280.0 nm
38.1 nm
-42.6 nm
280.0 nm
25.1 nm
-32.6 nm

Images of collagen fibrils distribution pre and post treatments

Pre - Distilled water	Post – Distilled water
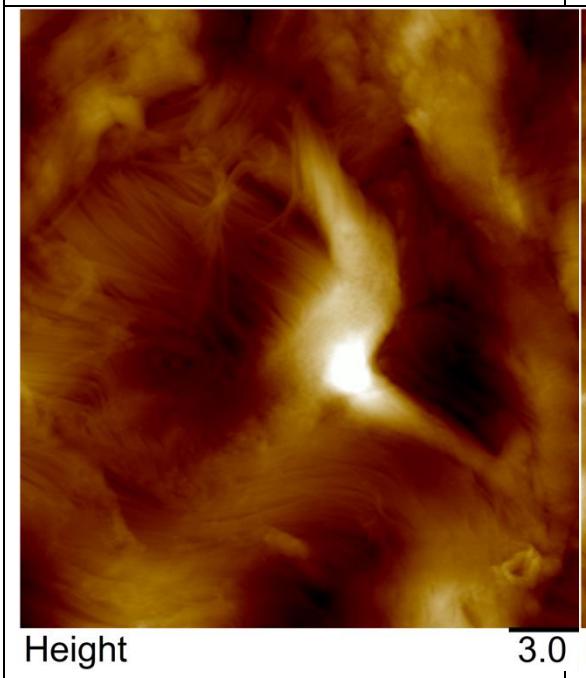	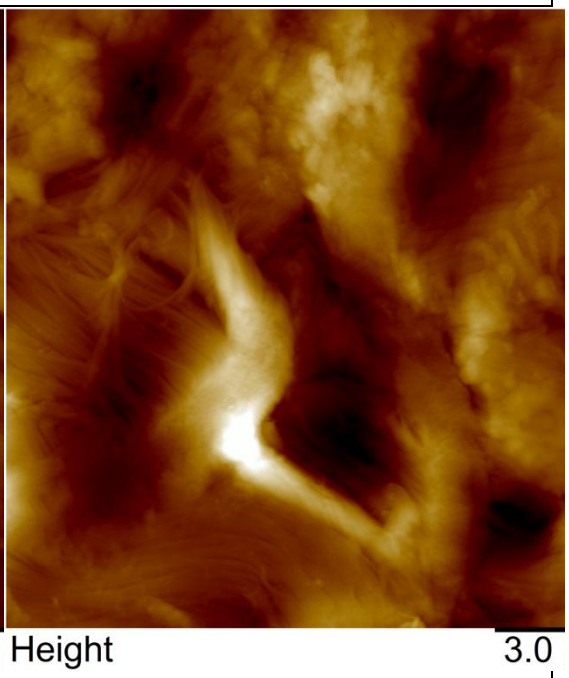
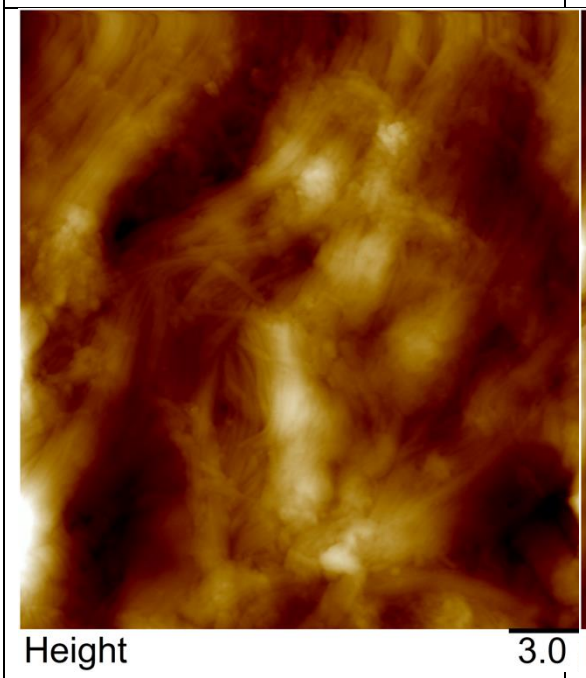	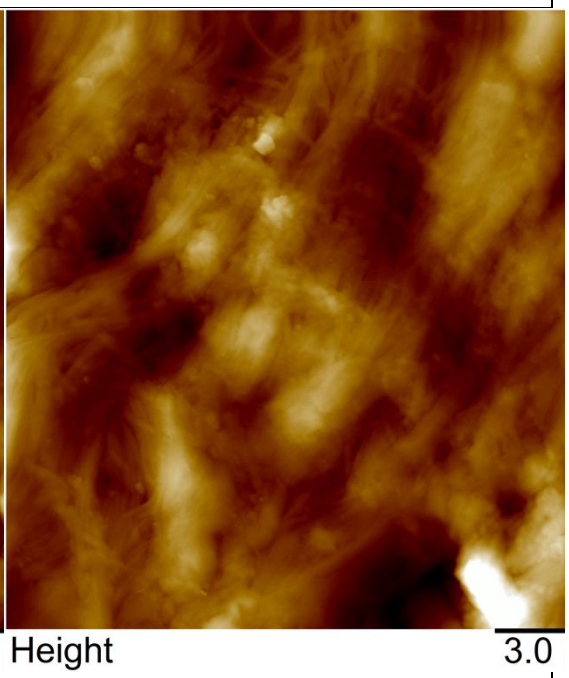

Pre - PBS	Post – PBS
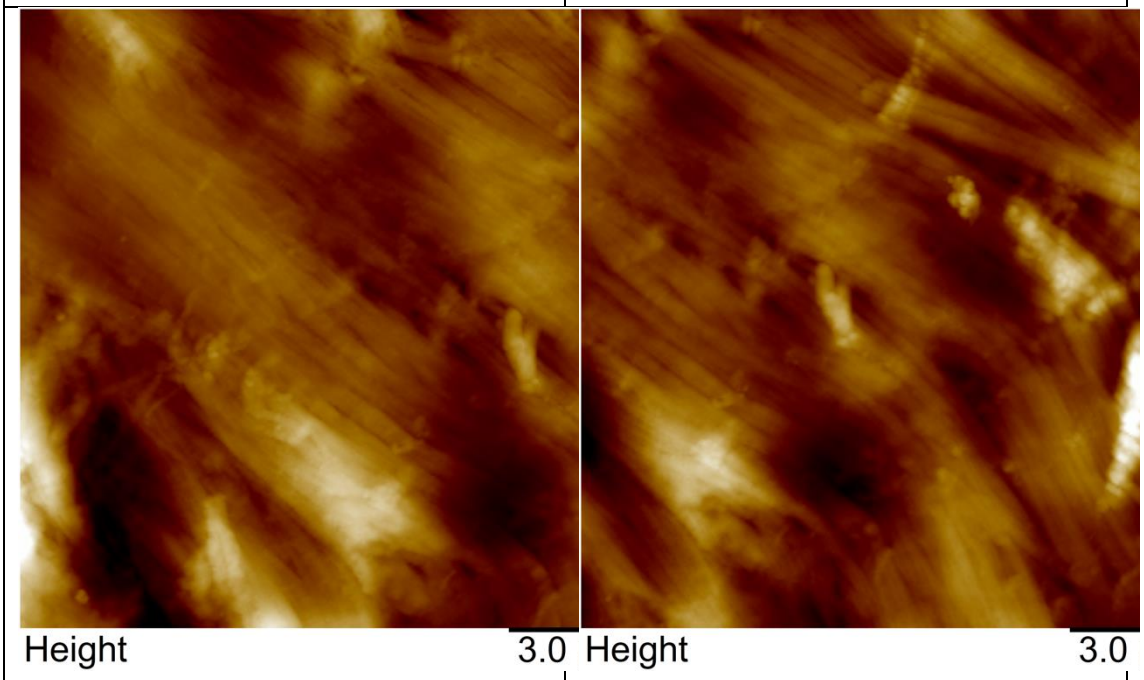	
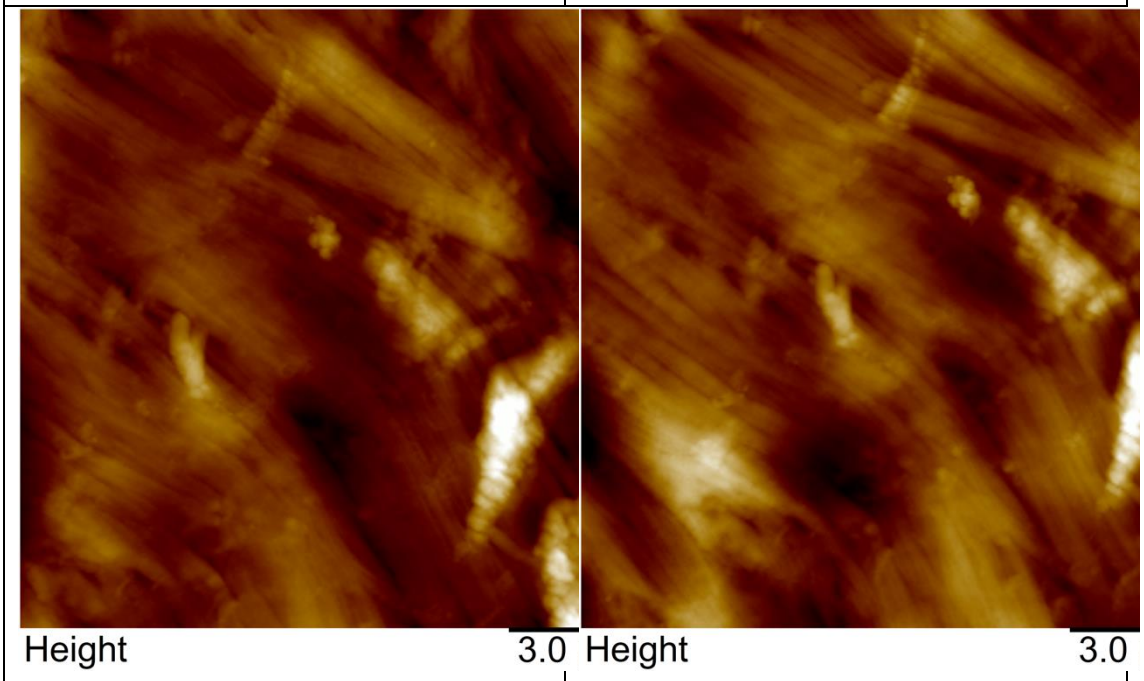	

Pre -Amylase	Post - Amylase
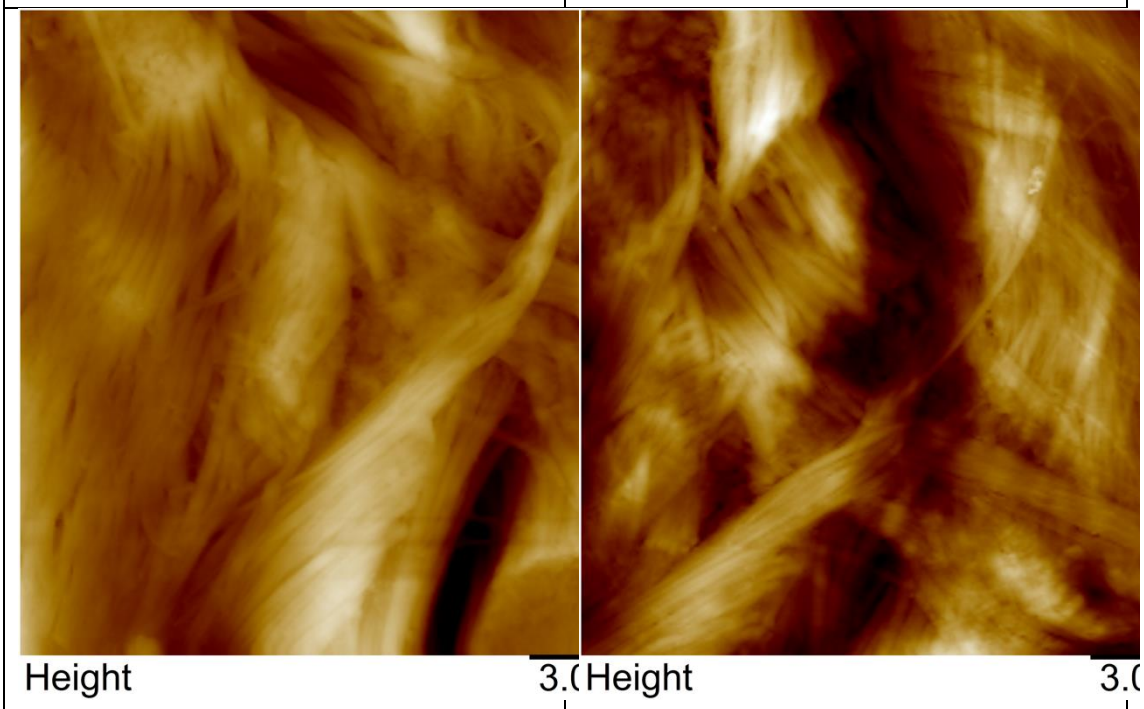	
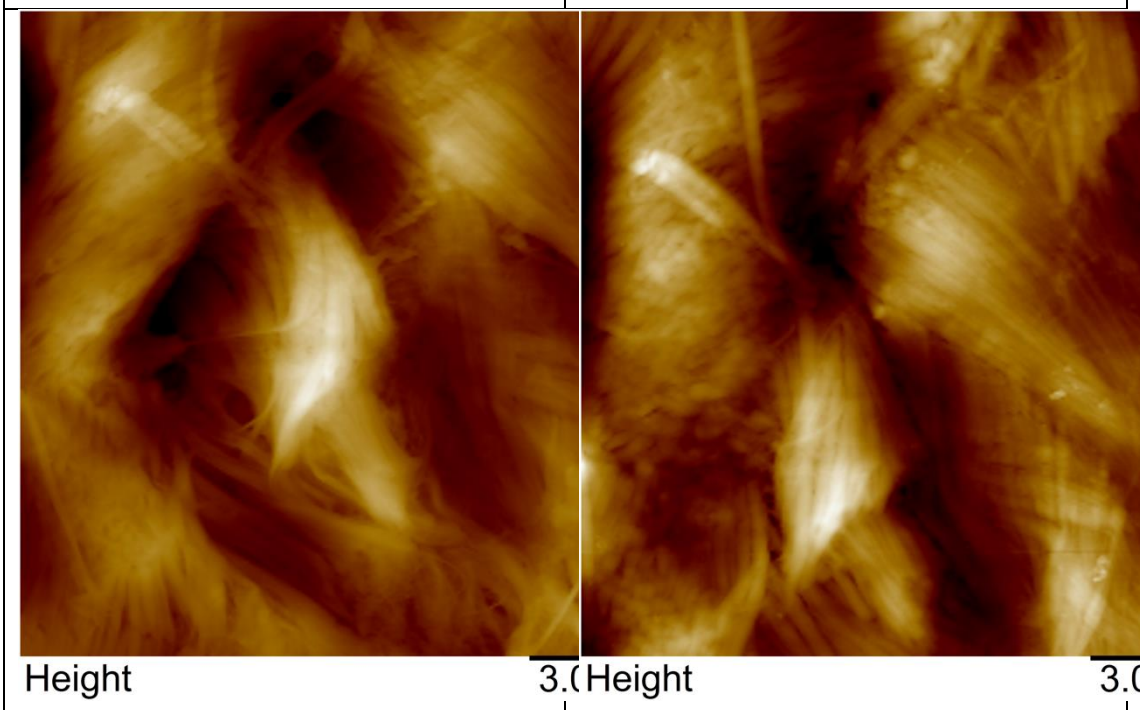	

Pre -Chondroitinase ABC	Post – Chondroitinase